Reverse Water-Gas Shift Chemical Looping for Syngas Production from CO_2

Dissertation
zur Erlangung des akademischen Grades

Doktoringenieur
(Dr.-Ing.)

von M.Sc. Marcus Wenzel
geb. am 05.04.1988 in Köthen (Anhalt)

genehmigt durch die Fakultät für Verfahrens- und Systemtechnik der Otto-von-Guericke-Universität Magdeburg

Promotionskommission: Prof. Dr.-Ing. Frank Beyrau (Vorsitz)
Prof. Dr.-Ing. Kai Sundmacher (Gutachter)
Prof. Dr. Guy Marin (Gutachter)
Prof. Dr. techn. Viktor Hacker (Gutachter)

eingereicht am: 03.04.2018
Promotionskolloquium am: 22.10.2018

This thesis is dedicated to my newborn daughter.

Acknowledgements

A work like this is never done by a single person. The numerous people who were directly or indirectly involved in this undertaking shall be gratefully acknowledged in the following.

First of all I would like to thank Prof. Sundmacher for giving me the opportunity to work on an interesting as well as challenging scientific topic. I am very grateful for the granted trust and the motivating discussions which forced me to repeatedly reconsider and improve my work. The working environment at the MPI helped me to develop the necessary skills to work independently and goal-oriented. The possibility to go to many different high quality conferences and international reseach partners was vital for my personal and professional growth. I am also grateful for the extensive teaching experience I was able to get during my time at the Max Planck Institute. Furthermore, I would like to thank Dr. techn. Liisa Rihko-Struckmann for supervising me during my PhD time. The help in getting my first publication ready was immensely important for my future work progress and for the belief in my own work. The countless discussions and suggestions made my work more scientifically sound and my writing more concise. I also kindly acknowledge Prof. Guy Marin, Dr. Vladimir Galvita and Dr. Aditya Dharanipragada for taking care of me during my stay at Ghent University. It was a pleasure working with you.

My time in the laboratory studying iron oxide mixtures would not have been possible without the help of Bianka Stein and Markus Ikert. My gratitude goes to them for undertaking the challenge of kindly and patiently teaching another know-it-all student how not to do things in the lab. Thank you for your continued professional support and for your open ear!

Working on my PhD thesis entailed sitting countless hours in a big office. This time would not have been as pleasurable without the lengthy and enjoyable discus-

sions with my colleagues and friends. Especially I would like to thank (in alphabetical order) Erdal Aydin, Jens Bremer, Ali el-Sibai, Andreas Himmel, Nicolas Kaiser, Florian Karst, Georg Liesche, Mostafa Mangal, Dominik Schack and Alexander Zinser. I enjoyed every minute in and out of the Max Planck Institute with all of you. I am not exaggerating when saying that I probably would not have been able to finish this work without your personal support and scientific input.

I also want to acknowledge the countless students who - by relentlessly questioning my expertise - pushed me to delve much deeper into topics I once thought I understood. They clearly showed me the difference between knowing something and being able to explain it to others.

My personal gratitude goes to my ever-supportive parents, Margit and Bernd. Without them I would not have even cared to take up studying. My personal and professional growth is inextricably linked to their personal and financial support over all those years. Thank you for believing in me!

I thank all of my friends and acquaintances for again and again reminding me not to forget to take pleasure and joy in the world outside of work.

Last but not least, my greatest love goes to my dear Katharina who always backed me up and gave me strength during the hard times. You are the joy of my life and I am deeply indebted to you for delivering us the pleasures of parenthood. How pale my life would be without you!

Abstract

This thesis comprises a systematic approach for the evaluation of the reverse water-gas shift chemical looping (RWGSCL) process for CO_2 utilization. The RWGSCL process is first investigated theoretically by thermodynamic principles. By assessing the maximum possible oxygen storage capacity and by calculating the reaction equilibrium of many possible oxygen storage materials (OSMs), it is shown that even though many potential OSM candidates are available only very few warrant further investigation. Iron oxide is shown to be one of the most promising materials for the RWGSCL process. A thorough analysis of the entire syngas production chain from CO_2, H_2 and solar energy is performed for the RWGSCL process based on flowsheet simulation and optimization and compared to the traditional RWGS reaction. It is shown that an overall solar-to-syngas efficiency of 13.7% can be realized which is comparable to theoretical estimates for solar-thermochemical looping as the main competing process of RWGSCL. Energy consumption in the reactor/seperator sequence of the process flowsheets is reduced by 54% for RWGSCL compared to a traditional RWGS reactor. These results serve as a proof of concept indicating that the RWGSCL is a promising process for CO_2 utilization.

To validate iron oxide as a possible OSM for RWGSCL different experimental techniques were used. Pure iron oxide was modified with $Ce_{0.5}Zr_{0.5}O_2$ to enhance the sintering resistance and to improve the reaction kinetics. The modified iron oxide was characterized by in-situ XRD and TEM. Transformation from Fe_3O_4 to Fe upon reduction with H_2 and subsequent reoxidation from Fe to Fe_3O_4 with CO_2 was verified yielding a potentially high oxygen storage capacity. The reduction and oxidation reaction kinetics were measured by TGA at ambient pressure and varying temperatures (973–1173 K) and inlet conditions (8–75 mol% of CO_2 or H_2, respectively). Different kinetic models were compared and kinetic parameters were estimated for the most suitable model based on the experimental data. Furthermore, long time experiments

were conducted and a stable CO production during oxidation was realized after 100 redox cycles.

Based on the kinetic expressions derived in this thesis, process simulation and optimization is performed to identify the most promising reactor concept for scale-up of the RWGSCL process. Dynamic 1D models are derived for fixed bed and fluidized bed reactor designs. Special emphasis is on the derivation of thermodynamically consistent reaction rate expressions for the equilibrium limited gas-solid reactions that occur in the RWGSCL process. Process optimization is performed for both reactor designs. Two conflicting objectives were used to evaluate the process performance: 1) the OSM utilization and 2) the average CO concentration. It is shown that the fixed bed reactor design is superior with regard to both objectives.

Zusammenfassung

In dieser Arbeit wird ein systematisches Vorgehen für die Analyse und die Bewertung des Reverse Water-Gas Shift Chemical Looping (RWGSCL) Prozesses im Kontext der CO_2-Nutzung vorgestellt. Zu Beginn wird der RWGSCL Prozess basierend auf thermodynamischen Prinzipien theoretisch untersucht. Durch die Ermittlung der maximal möglichen Sauerstoffspeicherkapazität und durch chemische Gleichgewichtsberechnungen wird gezeigt, dass nur sehr wenige der vielen potenziell verfügbaren Sauerstoffspeichermaterialien für weitere Untersuchungen in Frage kommen. Es stellt sich heraus, dass Eisenoxid eines der vielversprechendsten Materialien für den RWGSCL Prozess ist. Weiterhin wird der RWGSCL Prozess mit anderen Chemical-Looping Prozessen verglichen und es wird gezeigt, dass solarthermisches Looping der einzige direkt vergleichbare Konkurrenzprozess ist. Eine umfassende Analyse eines möglichen Gesamtprozesses zur Synthesegasherstellung aus CO_2, H_2 und Sonnenenergie wird für den RWGSCL Prozess mit Hilfe von stationärer Prozesssimulation und -optimierung durchgeführt. Die Resultate werden einem Vergleichsprozess, basierend auf der traditionellen RWGS Reaktion, gegenübergestellt. Ein energetischer Gesamtwirkungsgrad (ausgehend von Sonnenenergie bis hin zum Synthesegas) von $13,7\%$ kann für die Synthesegasherstellung mittels RWGSCL erreicht werden. Dieser Wert ist vergleichbar mit theoretischen Werten für solarthermisches Looping. Der Energiebedarf im Reaktor-Separator-Netzwerk des Gesamtprozesses lässt sich durch den RWGSCL Prozess im Verleich zur traditionellen RWGS Reaktion um 54% verringern. Die Resultate belegen die theoretische Machbarkeit des RWGSCL Konzepts.

Zur Validierung von Eisenoxid als potenzielles Sauerstoffspeichermaterial für den RWGSCL Prozess wurden diverse Experimente durchgeführt. Basierend auf dem Vorwissen von früheren Arbeiten wurde das reine Eisenoxid mit $Ce_{0.5}Zr_{0.5}O_2$ dotiert, um die Sinterungsbeständigkeit zu erhöhen und die reaktionskinetischen Eigenschaften zu verbessern. Das modifizierte Eisenoxid wurde mittels Röntgenbeugung und Transmissionselektronenmikroskopie charakterisiert. Die Reduktion von Fe_3O_4 zu

Fe mittels H_2 sowie die anschließende Oxidation von Fe zu Fe_3O_4 mittels CO_2 wurden experimentell belegt. Die Kinetiken der Reduktion und Oxidation wurden durch thermogravimetrische Messungen bei atmosphärischem Druck, Temperaturen von 973–1173 K und unterschiedlichen Gaszusammensetzungen am Reaktoreingang ermittelt. Unterschiedliche kinetische Modelle wurden zur Beschreibung der Kinetiken verglichen und die kinetischen Parameter wurden für das passendste Modell ermittelt. Weiterhin wurden Langzeitexperimente durchgeführt, um die Stabilität des Materials nach wiederholten Reduktions-Oxidations-Zyklen zu analysieren. Ein stabiler Betriebszustand konnte nach etwa 200 Zyklen erreicht werden.

Mithilfe der ermittelten kinetischen Gleichungen können weitere Simulations- und Optimierungsstudien durchgeführt werden, um vielversprechende Reaktorkonzepte für eine großskalige Synthesegasherstellung basierend auf dem RWGSCL Prozess zu identifizieren. Dynamische, örtlich verteilte Modelle werden für den Festbettreaktor und den Wirbelschichtreaktor hergeleitet. Ein spezieller Fokus liegt auf der Herleitung von thermodynamisch konsistenten Reaktionsratengleichungen für die gleichgewichtslimitierten Gas-Feststoff-Reaktionen, die im RWGSCL Prozess ablaufen. Eine Prozessoptimierung wurde für beide Reaktortypen durchgeführt. Dazu werden zwei gegensätzliche Optimierungsziele definiert: 1) der Nutzungsgrad der Sauerstoffspeicherkapazität und 2) die mittlere CO Konzentration am Reaktorausgang. Es wird gezeigt, dass der Festbettreaktor für beide Optimierungsziele bessere Werte erzielt als der Wirbelschichtreaktor.

Table of contents

Nomenclature **xv**

1 Introduction **1**
1.1 Motivation . . . 1
1.2 Aim of this work . . . 3

2 Theoretical background **7**
2.1 CO_2 utilization reactions . . . 7
2.2 RWGS for CO_2 activation . . . 9
2.2.1 Thermodynamic considerations . . . 10
2.2.2 Advantages of RWGS for CO_2 activation . . . 11
2.2.3 Intensification of RWGS . . . 12

3 Chemical looping for process intensification **15**
3.1 Rationale for chemical looping . . . 16
3.2 RWGS chemical looping (RWGSCL) . . . 18
3.3 Comparison of chemical looping applications . . . 20
3.4 Oxygen storage materials . . . 24
3.4.1 Classification of OSMs . . . 25
3.4.2 Selection of OSMs for RWGSCL . . . 26
3.5 Conclusions . . . 31

4 Efficiency analysis **33**
4.1 Process systems . . . 34
4.1.1 Reverse water-gas shift (RWGS) . . . 34
4.1.2 Reverse water-gas shift chemical looping (RWGSCL) . . . 35
4.2 Thermodynamic model . . . 36
4.2.1 Solar energy collection . . . 37
4.2.2 Electrolysis . . . 38
4.2.3 Reactor . . . 38

4.2.4 H_2O flash . . . 40
4.2.5 Separator . . . 40
4.2.6 Heating and cooling . . . 41
4.2.7 Mixer . . . 42
4.3 Results and discussion . . . 43
4.3.1 Optimization results . . . 44
4.3.2 Comparison with syngas production by STL . . . 47
4.4 Conclusions . . . 49

5 Kinetic analysis 51
5.1 Experimental . . . 53
5.1.1 Material synthesis . . . 53
5.1.2 Material pretreatment and stabilization . . . 53
5.1.3 TEM . . . 54
5.1.4 Conventional and in-situ XRD . . . 54
5.1.5 Thermogravimetric analysis . . . 54
5.2 Results and discussion . . . 55
5.2.1 Material pretreatment . . . 55
5.2.2 TEM . . . 56
5.2.3 XRD analysis . . . 58
5.2.4 Thermogravimetric analysis . . . 59
5.2.5 Master plot analysis . . . 62
5.2.6 Parameter estimation . . . 67
5.3 Conclusions . . . 69

6 Process design and optimization 71
6.1 Process modeling . . . 74
6.1.1 Fixed bed . . . 75
6.1.2 Fluidized bed . . . 76
6.1.3 Reaction kinetics . . . 78
6.1.4 Model parameters and fluid dynamics . . . 85
6.1.5 Optimization . . . 88
6.1.6 Solution strategy . . . 92
6.2 Results and discussion . . . 93
6.2.1 Simulation . . . 93
6.2.2 Optimization . . . 98
6.3 Conclusions . . . 103

7 Conclusions and outlook **105**
7.1 Concluding remarks 105
7.2 Outlook and future research areas 107

Appendix A **111**
A.1 Minimum conversion for OSM selection 111
A.2 TGA model for parameter estimation 112
A.2.1 Balance equations 112
A.2.2 Kinetics 114
A.3 Fixed bed model derivation 114
A.4 Two-region fluidized bed model derivation 119
A.5 Numerical stability 125

References **129**

List of figures **143**

List of tables **145**

Publications and statements of authorship **147**

Curriculum vitae **151**

Nomenclature

Roman Symbols

C	Solar concentration factor	–
c_p	Molar heat capacity	J/mol/K
$D_v^{(\mathrm{s})}$	Average vertical dispersion coefficient for the solid	m^2/s
d_{b0}	Initial bubble size	m
d_{bm}	Limiting bubble size	m
d_{p}	Particle diameter	m
d_{t}	Fluidized bed reactor inner diameter	m
E_A	Activation energy	J/mol
F	Dimensionless energy factor	–
$\dot{F}$	Volume flow	m^3/s
g	Gravitational acceleration	m/s^2
G_0	Nominal solar influx	W/m^2
$\dot{H}$	Enthalpy flow	mol/s
HHV	Higher heating value	J/mol
h	Molar enthalpy	J/mol
j	Diffusive flux	$\mathrm{kg}/\mathrm{m}^2/\mathrm{s}$
k^0	Pre-exponential factor (Arrhenius equation)	s^{-1}
$K^{(\mathrm{be})}$	Bubble-emulsion gas interchange coefficient	s^{-1}
K_{eq}	Chemical equilibrium constant	–
L	Reactor length	m
L_H	Parameter for heat loss	–
M	Molar mass	g/mol
m	Reaction order (gas phase)	–
$\dot{N}$	Molar flow	mol/s
n	Reaction order (solid phase)	–
N_C	Number of components	–

N_{FV}	Number of finite volumes	–
N_R	Number of reactions	–
o	Experimental data point	–
p	Pressure	Pa
$\dot{Q}$	Heat flow	J/s
r	Reaction rate	varies
R	Universal gas constant	J/mol/K
R^2	Coefficient of determination	–
T	Temperature	K
t	Time	s
v	Velocity	m/s
$v^{(\mathrm{b'})}$	Bubble gas velocity	m/s
$v^{(\mathrm{b})}$	Rise velocity of bubble gas	m/s
v_{br}	Bubble rise velocity for single bubbles	m/s
v_{mf}	Minimum fluidization velocity	m/s
V	Volume	m^3
$\dot{W}$	Work flow/power	J/s
w	Mass fraction	–
X	Conversion	–
x	Mole fraction	–
$\bar{x}_{\mathrm{CO}}$	Average CO concentration	–
X_{OSM}	OSM utilization	–
y	Ratio of mole fractions	–
Y_{CO}	CO yield	$\mathrm{mol_{CO}/kg}$
Y_{C}	Gas phase carbon content	–
Y_{H}	Gas phase hydrogen content	–
z	Axial spatial coordinate	m

Greek Symbols

α	Degree of reduction	–
$\Delta_R g$	Free Gibbs energy change of reaction	kJ/mol
$\Delta_R h$	Enthalpy change of reaction	kJ/mol
δ	Bubble fraction	–
$\varepsilon_{\mathrm{mf}}$	Minimum fluidization voidage	–
ε	Fixed bed void fraction	–
η	Steepness parameter for sigmoid function	–
η_{eff}	Effectiveness factor of the reaction rate	–

η_{S}	Separation efficiency	–
η_{SEC}	Solar energy collection efficiency	–
η_{StE}	Solar-to-electricity efficiency	–
η_{StS}	Solar-to-syngas efficiency	–
μ	Dynamic viscosity	$\mathrm{Pa \cdot s}$
ν	Stoichiometric coefficient	–
Ψ	Influence of the solid on the reaction rate	–
ρ	Density	$\mathrm{kg/m^3}$
σ	Stefan-Boltzmann constant	$\mathrm{W/m^2/K^4}$
σ^M	Specific source term	$\mathrm{kg/m^3/s}$
Θ	Generalized time	s
$\dot{\xi}$	Reaction extent per unit time	mol/s
ξ	Reaction extent	–

Superscripts

0	Value at standard conditions (298 K and 0.1 MPa)
(b)	Bubble phase
(E)	Electrolyzer
(e)	Emulsion phase
(g)	Gas component
(C)	Condenser/H_2O flash
Ox	Oxidation reaction
(R)	Reactor
Red	Reduction reaction
(s)	Solid component
(S)	Separator

Subscripts

+	Forward reaction
−	Reverse reaction
act	Actual
α	Gas component index
β	Solid component index
eff	Effective
in	Inlet conditions
int	Interstitial
out	Outlet conditions

rev	Reversible
TG	Thermogravimetric unit

Acronyms / Abbreviations

CCS	Carbon capture and storage
CCU	Carbon capture and utilization
CLC	Chemical looping combustion
CL	Chemical looping
CLDR	Chemical looping dry reforming
CLOU	Chemical looping with oxygen uncoupling
CLR	Chemical looping reforming
CWGS	Cyclic water-gas shift
HR-TEM	High resolution transmission electron microscopy
iG-CLC	In-situ gasification chemical looping combustion
LPG	Liquefied petroleum gas
MEA	Monoethanolamine
NLP	Nonlinear programming
OSC	Oxygen storage capacity
OSM	Oxygen storage material
RWGSCL	Reverse water-gas shift chemical looping
RWGS	Reverse water-gas shift
SEC	Solar energy collection
SERWGS	Sorption enhanced RWGS
SNG	Synthetic natural gas
SOFC	Solid oxide fuel cell
StE	Solar-to-electricity
STL	Solar thermochemical looping
StS	Solar-to-syngas
TEM	Transmission electron microscopy
TG	Thermogravimetry
TPO	Temperature programmed oxidation
TPR	Temperature programmed reduction
XRD	X-ray diffraction

1 | Introduction

The system of nature, of which man
is a part, tends to be self-balancing,
self-adjusting, self-cleansing.
Not so with technology.

E. F. Schumacher

1.1 Motivation

Biophysical subsystems on Earth evolved dynamically over the course of millions of years through natural selection and proved to be stable within certain boundaries over a limited time frame. However, several mass extinction events led to the collapse of a great number of subsystems. These events are hypothesized to be caused by a combination of prolonged multi-generational stress on ecosystems (e.g. change in sea level, volcanism and resulting CO_2 emissions, etc.) and a sudden, catastrophic event (e.g. asteroid impact) [16]. To the best of our knowledge none of the mass extinction events has been caused by a single living species but they were a result of global environmental change. However, increasing evidence shows how today humankind disturbs the global environment on Earth far more than any other living being, throwing many of its subsystems out of balance. In a paper by Rockström et al. [146], nine planetary boundaries are identified in which humankind is expected to be able to operate safely without triggering global, abrupt environmental change. While these boundaries can only be roughly estimated with the current state of knowledge, their existence is certain. It is furthermore estimated that humanity already transgressed three of the nine planetary boundaries. These are for climate change, rate of biodiversity loss and change in the global nitrogen cycle. Thus, humans are already

causing prolonged multi-generational stress on ecosystems. Transgressing even more boundaries for too long will eventually result in a functional collapse of our current environment.

Today, the most widely recognized transgression of a planetary boundary is for climate change caused by extended green house gas emissions, most importantly CO_2. While no one can ascribe climate change effects to humankind (and humankind alone) with full certainty, strong and convincing evidence exists that we are at least a major contributor [91]. The science community worldwide agrees on this as seen by the fact that approximately 97% of published papers directly or indirectly dealing with climate change endorse a strong human influence [45, 46]. However, the predicted global temperature rise may not be interpreted as a "climate disaster" as it is often referred to in the public media. While the climate just is disturbed from the current state to a new state the "disaster" occurs for the human species (among many other species [5]) as we are neither adapted to the world we are about to create nor are we able to adapt to it in a sufficiently short amount of time. Once we disturbed the Earth; now we are the disturbed ones. The recent political developments regarding the deceleration and/or reversal of climate change (most importantly the Kyoto Protocol and the Paris Agreement) reflect the growing concerns of human-made climate change. They show that we can no longer reject the responsibility we have to our planet. Reductions of global fossil fuel use and the resulting CO_2 emission are the foremost goals of the recent debates about climate change. Nonetheless, concern was raised if the planned intergovernmental actions negotiated in the Paris Agreement (among other treaties) are sufficient and suitable to keep the global temperature rise below 2 K compared to pre-industrial levels [148]. The main reason is the lack of enforcing mechanisms for the agreed upon policies. In a recent paper, Victor et al. warn that all major industrialized countries are failing to meet the pledges they made and that they are not even enacting all the policies that they planned to do [170].

What is needed now more than ever are efficient technologies that reduce further emissions of CO_2 and replace fossil fuels in the long run. These technologies must be feasible and affordable to be able to compete with solutions that use (still) inexpensive fossil fuels. Carbon capture and storage (CCS) is one major technology for reducing CO_2 emissions by capturing CO_2 preferably from large-scale point sources like fossil fuel power plants and storing it in underground geological formations (CO_2 sequestration) like depleted oil or gas reservoirs. While it is a technologically feasible [79] and economically attractive way to reduce CO_2 within the coming years [91], CCS has several problems. When implemented in power plants, carbon capture uses

up 10 – 40% of the energy produced [129] leading to a net increase in fossil fuel consumption [145]. Furthermore, CO_2 emissions may be reduced but on the other hand the emission of air pollutants like ammonia and nitrous oxides are increased [91] and the potential risks of storing massive amounts of CO_2 underground for thousands of years can hardly be assessed.

Another emerging technology branch is Carbon Capture and Utilization (CCU) in which CO_2 is captured (just as in CCS) but instead of being stored it is used as a reactant for chemical processes like the production of methanol, carbon-neutral fuels and other chemicals (especially the production of synthetic fuels from CO_2 is attractive because our current carbon based economy would not need to be refitted to run on alternative fuels like hydrogen). CCU is not a technology for reducing CO_2 emissions or the total atmospheric CO_2 but it plays an important role in closing the carbon loop (i.e. stabilizing the net CO_2 amount in the atmosphere). For CCU to be carbon-neutral the energy that is needed for the chemical transformation of CO_2 into the desired product must be supplied by renewable and carbon-neutral energy. Otherwise, CCU processes become just another source of CO_2. By collecting CO_2 from the atmosphere the carbon loop can be closed in theory and a steady atmospheric CO_2 level can be established (i.e. if renewable energy is abundantly available). Since there are economic sectors where reasonable alternatives for fossil fuels are yet to be found (e.g. aviation) the need for CCU is indisputable. If large parts of human economy remain based on carbon, CCU processes must be established on a large scale to create a sustainable foundation for our future (possible future economies based on hydrogen or methanol are not discussed here for the sake of space).

CCS and CCU are both important technologies in light of the climate change debate, but they serve very different purposes. While CCS is a relatively mature technology, most CCU processes are in an earlier stage of development. This thesis focuses on CCU as it is seen as one foundation for a sustainable carbon economy.

1.2 Aim of this work

Since there are only few direct uses of CO_2 (e.g. for the production of urea and salicylic acid, carbonated water or as dry ice), the heart of every CCU technology is the conversion of CO_2 into another substance which can be used instead. This work investigates possibilities for converting CO_2 by hydrogen via the reverse water-gas shift reaction (RWGS). The RWGS can be used to produce synthesis gas (from here on abbreviated

as syngas) which is a platform chemical used in a variety of large scale chemical processes and for the production of liquid fuels via Fischer-Tropsch synthesis (see Fig. 1.1). Sternberg et al. compared power-to-gas routes for syngas and methane production and estimated that syngas production is environmentally more friendly than methane production [164]. Thus, producing syngas sustainably from CO_2 offers high potential reductions in CO_2 emissions. Within this thesis the reverse water-gas shift

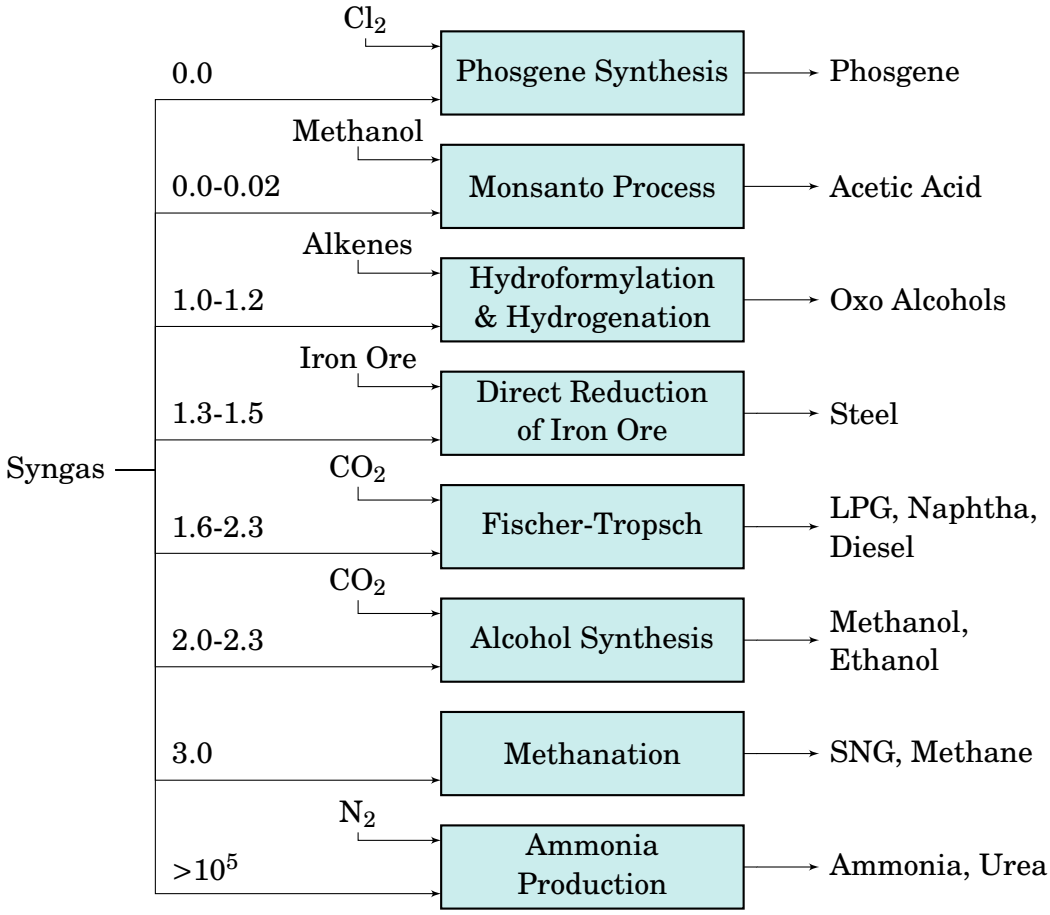

Fig. 1.1 Most important reaction routes for syngas with corresponding products. Numbers on the left indicate the necessary H_2/CO-ratio for the respective production route. Data taken from [85, 154]. Figure adapted from [176] with permission of Wiley and Sons.

chemical looping (RWGSCL) process is introduced and analyzed in detail. The process is based on the RWGS reaction and intensified by using an oxygen storage material (OSM). The analysis of the RWGSCL process is broadly structured into three parts: (1) thermodynamic analysis as proof of concept, (2) kinetic measurements, (3) detailed process simulation and optimization with the previously measured kinetics. The aim

of this thesis is to provide a systematic analysis of the RWGSCL process to show the advantages and drawbacks of using this approach for syngas production from CO_2 compared to the RWGS and other competing technologies.

This thesis is divided in seven chapters. Chapter 2 gives a short theoretical overview of the RWGS reaction and its possible applications for CO_2 utilization. A brief summary of the history is given and the importance of the RWGS with regard to CO_2 utilization in the future is emphasized. Process intensification options for the RWGS reaction are discussed.

Chapter 3 introduces the concept of chemical looping in general and gives an overview of the most important current applications. The advantages and drawbacks of chemical looping are discussed and the chemical looping concept is applied to the RWGS reaction. The resulting RWGS chemical looping (RWGSCL) process for syngas production from CO_2 is introduced and the general idea is explained. The unique features of the RWGSCL process are highlighted and compared to other chemical looping processes. A systematic OSM selection framework is proposed based on thermodynamic properties. Based on the results it is argued why modified iron oxide is chosen as OSM for RWGSCL within this thesis.

In Chapter 4 thermodynamic analysis is applied to the RWGSCL process to give a first estimate of its possibilities and limitations. The analysis is based on the assumption that renewable and CO_2-neutral energy is available to power the electrolyzer for hydrogen generation and all other processes. It is shown that with the RWGSCL process different syngas compositions can be supplied with an overall efficiency comparable to competing technologies. This chapter acts as a proof of concept and lays the foundation for more detailed investigations into the process.

Kinetics measurements on modified iron oxide particles are presented in Chapter 5. The preparation of the particles is followed by long term experiments in which the particles are thermally aged under operating conditions to give reasonable results which are comparable to real reactors. The material is characterized by in-situ x-ray diffraction (XRD) and transmission electron microscopy (TEM). Thermogravimetric analysis is used to measure the kinetics of the reduction and oxidation reactions. A mathematical model for the thermogravimetric unit is derived to simulate the results. The master plot method is used to discriminate between suitable kinetic models. Kinetic parameters are estimated for the most reasonable kinetic model.

In Chapter 6 the kinetic model is used to simulate real reactor behavior of the RWGSCL process. Mathematical models are derived for a fixed bed and a fluidized

bed reactor concept each based on two simultaneously operated reactors to systematically compare the two reactor designs for the RWGSCL process. The simulation results are analyzed and the unique reactor behavior due to the equilibrium limited gas-solid reactions is highlighted. Two different optimization problems are defined for the continuous production of CO_2. The optimal operating conditions for both reactor concepts are found and it is shown that the fixed bed reactor design gives superior performance over the fluidized bed reactor design.

Chapter 7 summarizes the thesis and puts it in perspective of the current state of CO_2 utilization. An outline is given for possible future research activities.

A graphical overview of the thesis is provided in Fig. 1.2.

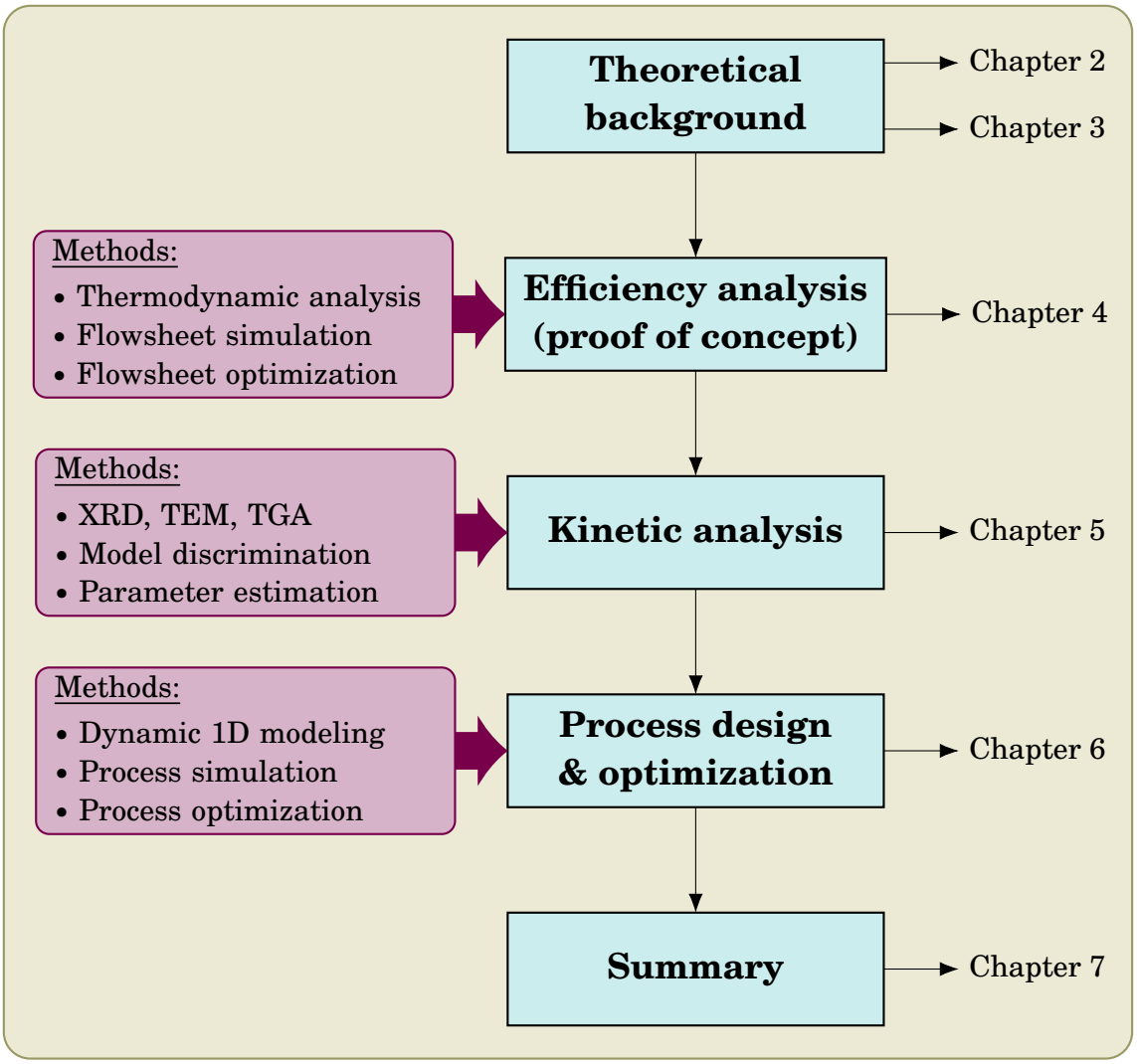

Fig. 1.2 Overview of the thesis.

2 | Theoretical background

If one does not know to which port
one is sailing, no wind is favorable.

Seneca

This chapter gives an introduction to CO_2 utilization reactions. Important reactions in the context of the climate change debate are highlighted and compared. It is illustrated how the RWGS reaction can be used to activate CO_2 and how it compares to competing CO_2 activation routes. The thermodynamic properties of the RWGS reaction are analyzed and critically discussed to illustrate its advantages and weaknesses for CO_2 utilization. An overview of process intensification options for the RWGS reaction is given.

2.1 CO_2 utilization reactions

Although CO_2 is a very stable molecule there are numerous reactions that it can theoretically undergo to form useful products [17, 25]. Currently, the industrial production of urea consumes the most CO_2 annually ($\approx 130\,\mathrm{Mt}$) [13]. However, the necessary CO_2 is usually extracted from the exhaust gas of an ammonia plant that is often combined with the urea plant for this reason. Incorporating CO_2 into other industry sector is important to decrease the net release of CO_2 into the atmosphere. In particular, reactions for producing bulk chemicals like syngas, methane (synthetic natural gas, SNG) or methanol gained increasing attention in the last years since high potential reductions of CO_2 emissions can be achieved if the traditional production routes are replaced by CO_2-based routes. Table 2.1 lists some of the most important power-to-gas reactions which are actively researched within the climate change debate (selected sources for reference in the context of CCU are given in the last column, the CO_2 dis-

sociation reaction is listed as a reference). As can be seen, the heat of reaction of CO_2

Table 2.1 Enthalpy change of reaction for important power-to-gas reactions using CO_2 as reactant with CO_2 dissociation as a reference. Values of $\Delta_R h^0$ given in kJ/mol at 298 K and 0.1 MPa. Selected sources for reference are given in the last column.

Name	Chemical reaction	$\Delta_R h^0$	References
CO_2 dissociation	$CO_2 \rightleftharpoons CO + \frac{1}{2}O_2$	+283	[43, 40, 97]
Dry reforming	$CO_2 + CH_4 \rightleftharpoons 2CO + 2H_2$	+247	[61, 26, 136]
Reverse water-gas shift	$CO_2 + H_2 \rightleftharpoons CO + H_2O$	+41	[98, 47, 176]
CO_2 hydrogenation	$CO_2 + 3H_2 \rightleftharpoons CH_3OH + H_2O$	−49	[18, 89, 172]
CO_2 methanation	$CO_2 + 4H_2 \rightleftharpoons CH_4 + 2H_2O$	−165	[31, 30, 149]

dissociation is very high due to the chemical stability of CO_2. Thus, large amounts of energy (e.g. heat or radiation) must be supplied to drive the reaction. On the other hand, contacting CO_2 with substances with increasing energy density (like methane and hydrogen) lowers the necessary energy input for the corresponding reaction. The CO_2 hydrogenation and the Sabatier reaction are exothermic because the high energy content of hydrogen relative to CO_2 provides more energy than necessary to split CO_2 (even though the temperature has to be sufficiently high in the first place to initiate the reaction by overcoming kinetic resistances). Thus, to overcome the energy barrier and to activate CO_2 (i.e. break the chemical bonds between C and O) it has to be contacted either with a highly reactive substance, a large amount of energy (e.g. heat, radiation, electrical energy) or both depending on the specific reaction [77, 41].

However, all reactions are driven by the difference of the Gibbs free energy between the the products and reactants at certain conditions. Therefore, even if enough energy is supplied to overcome the activation energy barrier of a reaction involving CO_2 as a reactant, the CO_2 conversion may still be very low due to thermodynamic limitations. Fig. 2.1 shows the Gibbs free energy of reaction $\Delta_R g$ for the reactions in Table 2.1. As can be seen, the RWGS reaction and dry reforming are thermodynamically favored (exergonic) by higher temperatures while CO_2 methanation is favored by lower temperatures. The CO_2 dissociation and CO_2 hydrogenation to methanol are thermodynamically unfavored (endergonic) within the depicted temperature range. From a thermodynamic perspective an operating temperature in the exergonic region should be preferred to achieve high CO_2 conversions. However, other aspects like reaction kinetics and catalyst operating temperature further restrict the permissible operating region making CO_2 activation a complex engineering problem.

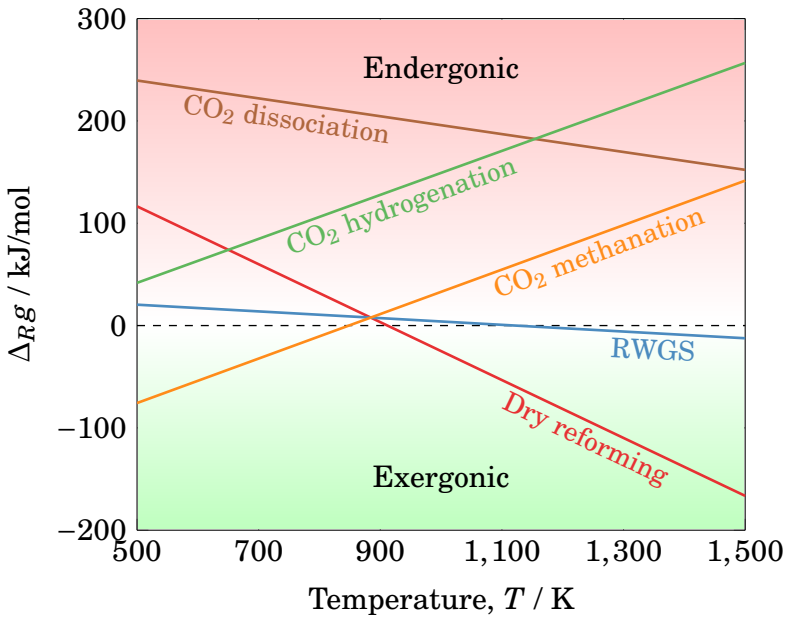

Fig. 2.1 Comparison of the Gibbs free energy of reaction $\Delta_R g$ for the reactions in Table 2.1. Data taken from [80] and [182].

2.2 RWGS for CO_2 activation

Due to the challenges stated above, the number of feasible and industrially interesting CO_2 activation reactions is highly limited by thermodynamic and engineering considerations. Furthermore, CO_2 activation remains economically unattractive due to the low price of fossil fuels and the lack of incentives to mitigate CO_2 emissions. Thus, in today's economy the main challenge is to find an energy efficient route for CO_2 activation [158, 157].

The RWGS reaction (and its counterpart, the water-gas shift reaction) has been studied extensively in the past as it occurs as an important side reaction in large scale industrial processes (e.g. steam reforming [114], methanol synthesis [183], conditioning of syngas [155], ect.). The main research focus has been on catalyst development (mostly Cu, Pt and/or Rh are used and immobilized on a variety of supports [47]), studies on the reaction mechanism and kinetic studies for the aforementioned processes. However, the literature on RWGS-based processes for CO_2 activation and syngas production is still scarce even though the number of publications is rising.

The most important reasons for the minor interest in the RWGS reaction for CO_2 utilization are arguably the high necessary operating temperature and the limited

CO_2 conversion. However, the technological readiness of the RWGS gives the process an important edge over other competing technologies for CO_2 utilization. The importance of the RWGS in present and future CCU scenarios is recognized and highlighted in recent literature. Mallapragada et al. compared different CO_2 conversion routes to liquid fuels based on the assumption that only renewable energy (solar energy) is used to make all routes sustainable. The pathway that uses the RWGS reaction for CO_2 activation was estimated to be the most promising with regard to energy efficiency in the present and the future [122]. Dimitriou et al. analyzed different concepts for liquid fuels production from CO_2 in which the RWGS reaction is used for CO_2 activation [53]. They found that all concepts are not yet economically viable. One of the reasons was the low CO_2 conversion in the RWGS process. Thus, active research on improving the RWGS reaction is needed. Nonetheless, the RWGS reaction followed by Fischer-Tropsch synthesis is already successfully used to produce liquid fuel in a pilot plant near Dresden by the German company Sunfire [4]. To further facilitate the rapid replacement of traditional production routes for chemicals by CCU processes, more successful implementations have to be demonstrated and scaled to industrial size in the future by innovative companies.

2.2.1 Thermodynamic considerations

In the RWGS reaction CO_2 reacts with hydrogen according to the following equation:

$$H_2 + CO_2 \rightleftharpoons H_2O + CO \qquad \Delta_R h(1073\,\mathrm{K}) = 36.84\,\mathrm{kJ/mol} \tag{2.1}$$

The reaction is mildly endothermic and strongly equilibrium limited as shown Fig. 2.1. To achieve an equilibrium CO_2 conversion of 50% a reaction temperature of $T \approx 1090\,\mathrm{K}$ is necessary (assuming equimolar amounts of hydrogen and CO_2). Higher temperatures lead to higher conversion but the thermal stress on the reactor parts and the catalyst limit the permissible reaction temperature. Therefore, the outlet gas of the RWGS unit consists of significant amounts of reactants. This is especially important to consider for downstream processing (see Fig. 1.1 in the introduction).

Fig. 2.2 shows the equilibrium composition of the RWGS reaction assuming equimolar amounts of hydrogen and CO_2 and a reaction pressure of $p = 0.1\,\mathrm{MPa}$. At temperatures below 900 K the CO_2 methanation is thermodynamically more favorable than the RWGS reaction (also see Fig. 2.1). Therefore, CH_4 is formed instead of CO. To avoid the formation of methane the temperature must be increased. Above 900 K

there is virtually no CH_4 formation. Alternatively CO-selective catalysts must be used (e.g. copper-based) for decreasing the methane content in the outlet gas [39, 147]. Pressure does not influence the equilibrium composition of the RWGS since there is no change in the total number of moles during the reaction (two moles on the reactant and product side).

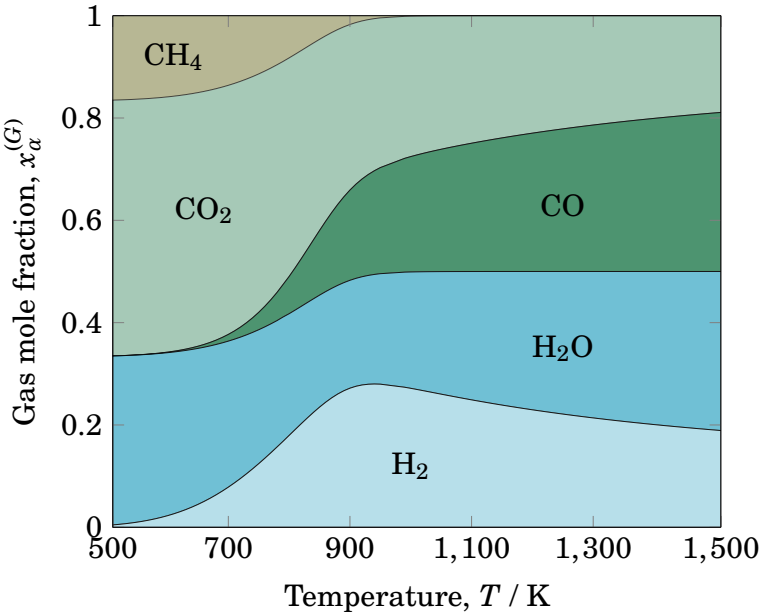

Fig. 2.2 Equilibrium gas composition calculated by Gibbs energy minimization for equimolar amounts of CO_2 and hydrogen at different temperatures and $p = 0.1\,\mathrm{MPa}$. CH_4 is stable for temperatures below 900 K.

2.2.2 Advantages of RWGS for CO_2 activation

To further reinforce the argument for the RWGS reaction, the advantages over some of the other CO_2 activation options are summarized in the following.

Most importantly, the RWGS produces syngas which is widely used in chemical industry (see Fig. 1.1). While worldwide syngas production was $\approx 70000\,\mathrm{MW_{th}}$ in 2010 [2], the production capacity today is $\approx 110000\,\mathrm{MW_{th}}$ with an increasing trend in the future. Producing these amounts by RWGS is of course inconceivable at the present moment but the large possible reduction of CO_2 emissions is justification enough to actively research alternatives to the traditional syngas production routes based on fossil fuels.

Compared to the CO_2 hydrogenation and methanation routes in Table 2.1 the RWGS reaction only needs one mole of hydrogen per mole of CO_2 to produce a value-added product (syngas). This is especially important considering the high cost of H_2 produced from renewables.

The RWGS reaction is mildly endothermic compared to other reactions discussed in Section 2.1. Thus, problems like hotspot formation in highly exothermic reactions like the CO_2 methanation can be avoided. Compared to the highly endothermic dry reforming reactions, the RWGS needs low energy supply. However, the energy still has to be supplied at a high temperature.

Direct CO_2 dissociation options via concentrated solar-thermochemical pathways seem promising in the future since they do not need an additional energy carrier like hydrogen or methane to activate CO_2. However, the technology is still in the research and development stage [124]. In a recent review Koepf et al. point at the "stubbornly stable resurgence of fossil fuel energy discovery and utilization" that perpetually delays the commercial breakthrough of solar-thermochemical CO_2 utilization among other sustainable technologies [107]. On the other hand, hydrogen production by electrolysis is commercially available already. Furthermore, the RWGS reaction is a standard heterogeneously catalyzed reaction that can be implemented today on a larger scale [75]. Thus, syngas production via the RWGS reaction is a technology ready for implementation.

2.2.3 Intensification of RWGS

Process intensification in the context of CO_2 utilization is concerned mostly with increasing the energy efficiency of the process and/or reducing the amount of CO_2 that is exhausted by the process. The main problems of the RWGS reaction are the high reaction temperature and the strong equilibrium limitation. Overcoming these problems could potentially make the RWGS reaction more attractive for commercial applications. In this section an overview is given of possible intensification options that have been already applied to the RWGS or that are actively researched. For a comprehensive list of process intensification options in general the reader is referred to textbooks on that topic [162, 142].

Sorption enhanced RWGS (SERWGS) In a paper by Carvill et al. from 1996 the concept of sorption enhancement for process intensification was proposed and studied

on the RWGS reaction as an example [36]. It was shown that nearly pure CO was produced at 523 K using a commercial NaX zeolite for water adsorption. The SERWGS process was mentioned in a perspective paper by Haije and Geerlings highlighting the potential for large scale syngas production [75]. However, the author could not find any other published work on the SERWGS process. It can only be guessed why further research stalled but reasons might include the inherently periodic operation of the reactors, low adsorption amounts per reactor volume and the difficult and complex pressurization and depressurization strategy of the reactor. Instead, active research is now focused on the sorption enhanced water-gas shift (SEWGS) process for pre-combustion carbon capture [169]. Since this concept is concerned with CCS it is not further discussed in this thesis.

Membrane reactors Whitlow and Parish published a paper on a RWGS membrane reactor concept in 2003 [178]. Optimal operating conditions for the demonstration reactor were found at 673 K and 310 kPa achieving a CO_2 conversion close to 100%. However, this was a small scale demonstration which was motivated by using the RWGS for space exploration (CO_2 is readily available on Mars and H_2 is obtained as a byproduct of oxygen generation). The author did not find scientific literature outside of space exploration for an RWGS membrane reactor.

Electrochemical promotion Some articles have been published on electrochemical promotion of the RWGS reaction. Bebelis et al. showed that the rate of CO formation can be increased by a factor of 6.7 by decreasing the catalyst potential to 0.34 V [24]. In another work by Pekridis et al. the RWGS was performed in a solid oxide fuel cell (SOFC) and CO formation rates were increased ten times in closed circuit operation compared to open circuit operation [139]. Karagiannakis et al. compared the reaction rates of the conventional, catalyzed RWGS to the RWGS performed with protons instead of molecular hydrogen in a H^+ conducting cell [99]. They found the reaction rates to be one order of magnitude higher for the electrochemically supplied hydrogen (protons).

Chemical looping Another process intensification option for RWGS is the concept of chemical looping, where the reaction is split into two reactions using a chemical intermediate, the so called oxygen storage material. In the next chapter the concept of chemical looping is introduced in general and applied to the RWGS reaction.

3 | Chemical looping for process intensification

We are all apprentices in a craft
where no one ever becomes a master.

Ernest Hemingway

The concept of chemical looping (CL) dates back to 1910 when a US patent was issued for a novel hydrogen production process [128]. The proposed process which is known as the steam-iron process is based on the water-gas shift reaction which is split into two reactions by an oxygen storage material (iron oxide in this example). The steam-iron process was used in the beginning of the 20th century for hydrogen production until competing technologies based on fossil fuels led to its gradual phasing out [57]. In recent years, the process gained renewed interest for clean hydrogen production for fuel cell applications [74, 181, 81]. The term chemical looping itself was coined in a paper by Ishida et al. published in 1987 [95]. Chemical looping in this thesis refers to any process in which an overall reaction is decomposed into multiple sub-reactions (at least two) by an oxygen storage material (OSM) that is cyclically reacted and regenerated [57]. Furthermore, the oxygen storage materials considered are limited to metal oxides as the majority of published literature is concerned with metal oxides. Thus, an arbitrary gas phase reaction

$$\mathrm{A} + \mathrm{B} \rightleftharpoons \mathrm{C} + \mathrm{D} \tag{3.1}$$

may be decomposed into two reactions by using an OSM:

$$\mathrm{A} + \mathrm{Me_yO_{x-1}} \rightleftharpoons \mathrm{C} + \mathrm{Me_yO_x} \tag{3.2}$$

$$\mathrm{B} + \mathrm{Me_yO_x} \rightleftharpoons \mathrm{D} + \mathrm{Me_yO_{x-1}} \tag{3.3}$$

Here, Me_yO_{x-1} and Me_yO_x refer to an arbitrary metal in its reduced and oxidized state, respectively. Adding up equations (3.2) and (3.3) yields the original equation 3.1 of the gas phase reaction. As can be seen, the OSM acts as an intermediate and is oxidized in the first reaction step (eq. (3.2), oxygen uptake) from its reduced state (Me_yO_{x-1}) to its oxidized form (Me_yO_x) and then reduced in the second reaction step (eq. (3.3), oxygen release). Therefore, cyclic oxygen release and uptake from and by the OSM is the key concept of chemical looping (see Fig. 3.1).

The successful implementation of any chemical looping concept requires that the reactions between the OSM and the gas are heterogeneous, i.e. the OSM is in the solid phase and reacts with a gas. It is in principle conceivable that the OSM reacts with another solid or liquid but these types of reactions are typically orders of magnitude slower than the preferred gas-solid reactions. In those cases the condensed phases should be gasified first and then reacted with the OSM [130].

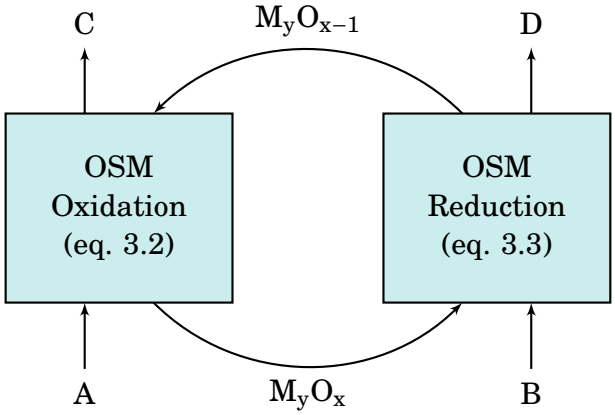

Fig. 3.1 Chemical looping concept for an arbitrary gas phase reaction $A + B \rightleftharpoons C + D$. The OSM is cyclically oxidized and reduced.

This chapter will first highlight the motivation for using chemical looping. Selected examples for important CCS and CCU applications are explained and compared. The reverse water-gas shift chemical looping (RWGSCL) process is introduced. The important role of the oxygen storage material will be highlighted and an OSM selection framework is presented for the RWGSCL process.

3.1 Rationale for chemical looping

The application of chemical looping as a process intensification option is motivated by some advantages that are discussed in the following. Principle thermodynamic

analyses of chemical looping processes were conducted by Richter and Knoche [143] as well as Anheden and Svedberg [15]. They found that process irreversibility can be minimized by applying the chemical looping concept to combustion reactions. Thus, the overall energy efficiency of a process can be enhanced. Furthermore, splitting a gas phase reaction into two or more sub-reactions leads to an inherent product separation. Considering the example above, the reaction products C and D are already separated in the chemical looping process (see Fig. 3.1) as opposed to the conventional gas phase reaction (eq. (3.1)), where a mixture of C and D is present at the reactor outlet. Therefore, energy expenditure for downstream product separation is potentially lowered. This advantage is the main motivation for using the chemical looping concept for CO_2 capture. Another important advantage is that undesired side reactions can effectively be avoided. In the previous example, the reactants A and B are never in direct contact in the chemical looping process. Thus, 100% selectivity towards the desired reaction is ensured.

On the other hand, using the chemical looping concept also entails some disadvantages. From an engineering perspective, using an OSM to split an arbitrary gas phase reaction into multiple sub-reactions means that a previously continuous process is turned into a cyclic semi-batch process. While this leads to increased degrees of freedom for operation, continuous operation is usually preferred for industrial processes (especially large scale processes). Thus, there is a natural barrier for industrial plant operators to adopt a semi-batch process instead of a truly continuous process. Another problem associated with chemical looping is the handling of the OSM. A frequent problem is gradual material degradation through sintering [86, 90, 153, 57, 12]. Furthermore, efficient contacting between the gas and the OSM has to be ensured. Therefore, the active surface area of the OSM must be maximized. This can be achieved for instance by special design of the material in a fixed bed type reactor (e.g. reticulated, porous structures [64, 12] or nanparticles embedded on a structural matrix [26]) or by using fluidization techniques. Heat recovery is another problem that has frequently been addressed in the literature. The problem of heat recovery occurs whenever the OSM reduction and oxidation (see Fig. 3.1) proceed at different temperatures. In that case, the reactors have to be cyclically cooled and heated which is detrimental to the overall energy efficiency [152, 33, 20, 55, 113].

3.2 RWGS chemical looping (RWGSCL)

The idea of chemical looping is now applied to the RWGS as a possible process intensification option. The RWGS reaction given in eq. (2.1) is split into two sub-reactions using a general metal oxide (MeO) as follows:

$$\text{Oxidation:} \qquad \mathrm{Me} + \mathrm{CO_2} \rightleftharpoons \mathrm{MeO} + \mathrm{CO} \tag{3.4}$$

$$\text{Reduction:} \qquad \mathrm{MeO} + \mathrm{H_2} \rightleftharpoons \mathrm{Me} + \mathrm{H_2O} \tag{3.5}$$

The metal is oxidized by CO_2 in the first reaction step and reduced by hydrogen in the second reaction step. Adding up both equations yields the RWGS reaction.

A comparison of general process schemes for the production of syngas by the conventional RWGS reaction and by RWGSCL is illustrated in Fig. 3.2. In both schemes renewable energy is used to fuel all process units (red dashed line=the system boundary). The gas mixture after the conventional RWGS unit (Fig. 3.2, left) has to be separated or conditioned to obtain syngas with a specified composition since all four components are present at the reactor outlet according to chemical equilibrium (see Fig. 2.2). Hydrogen may be added optionally to adjust the syngas composition further (dashed line). In the RWGSCL scheme (Fig. 3.2, right) CO leaves the RWGSCL unit and is mixed with H_2 to obtain any desired syngas composition. Water is recycled back to the electrolysis unit. Thus, it is theoretically more straightforward to produce CO-rich syngas with the RWGSCL process scheme. However, it must be noted that residual amounts of CO_2 may be present in the CO stream depending on the process conditions and the used OSM (a detailed comparative analysis is given in the Chapter 4).

First investigations of the RWGSCL process were conducted by Bhavsar et al. and Najera et al. [132, 26]. Their original goal was to combine chemical looping with dry reforming (see Table 2.1) and to obtain kinetic data by thermogravimetric measurements on iron-based OSMs. However, in their experiments they used hydrogen instead of CH_4 as a reducing gas effectively resulting in the RWGSCL process. Their experimental results showed that the process is feasible on a laboratory scale.

Similar research was conducted at Ghent University. Galvita et al. proposed chemical looping dry reforming (see Section 3.3) on cerium-doped iron oxide but they performed temperature programmed reduction and oxidation (TPR and TPO, respec-

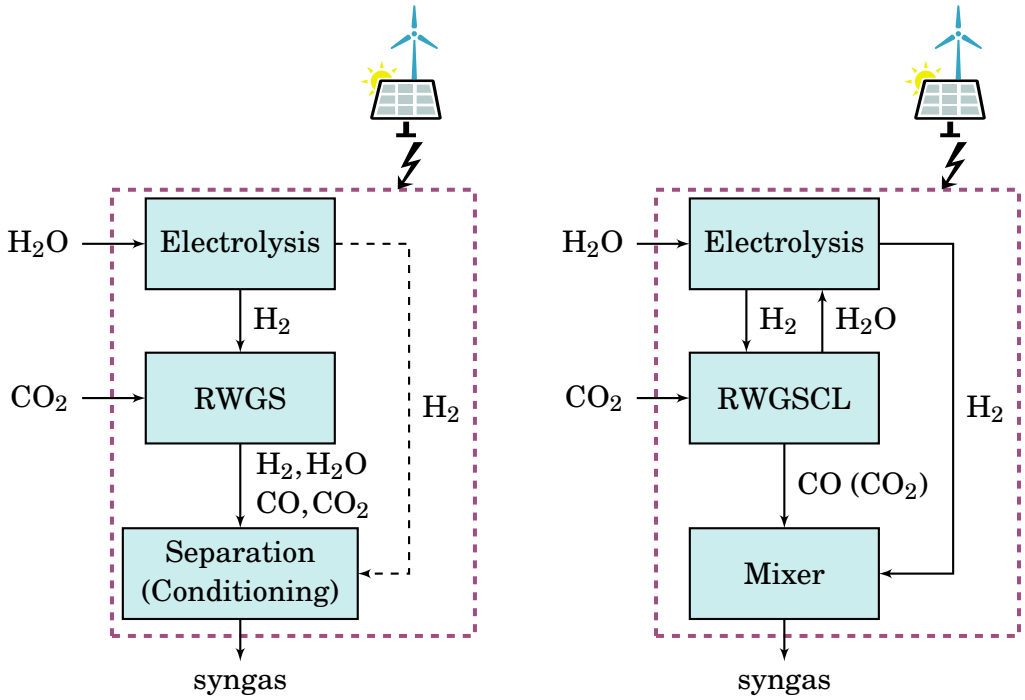

Fig. 3.2 General process schemes for the sustainable production of syngas from renewable energy, CO_2 and H_2O. Left: process based on the conventional RWGS reaction. Right: process based on RWGSCL. Red dashed lines indicate the system boundaries.

tively) with hydrogen and CO_2, respectively [67]. Thus, proving again the feasibility of the RWGSCL process.

Daza et al. were the first reserch group to name the process RWGSCL [48, 49]. Their work focused specifically on the RWGSCL process as opposed to the previously mentioned studies where hydrogen was used as a surrogate for other fuels like methane. They used XRD as well as TPR and TPO to analyze perovskite-type OSMs. Strontium-doped lanthanum cobaltites ($La_{1-x}Sr_xCoO_{3-\delta}$ and) were used in their first work on RWGSCL and they observed CO-formation at temperatures as low as 723 K [48]. In another paper they proved isothermal operation with a similar OSM ($La_{0.75}Sr_{0.25}Co_{1y}Fe_yO_3$) at 823 K [49]. Structural stability was observed over five reaction cycles (i.e. oxidation and reduction).

This thesis builds up on the work previously done in the field and aims to provide new insights for energy efficient operation of the RWGSCL process as most of the work done so far focused on OSM characterization and improvement. In the next section a brief overview of important chemical looping applications is given and the RWGSCL process is put into context.

3.3 Comparison of chemical looping applications

Since numerous applications of the chemical looping concept emerged in the last few decades and only few are interesting in the context of this thesis, the following overview is not meant to be comprehensive. It rather serves the purpose of putting the RWGSCL process into context and highlight the main competing processes.

First of all it is important to differentiate between CCS and CCU applications of chemical looping. The convention in this thesis is that CL processes in which CO_2 is produced are grouped into CCS and CL processes in which CO_2 is used as a reactant are grouped into CCU. Fig. 3.3 and Table 3.1 provide an overview of chemical looping processes that are important within the scope of this thesis. In the following all processes are shortly introduced and compared to RWGSCL.

Table 3.1 Classification of important chemical looping based processes. CLC=chemical looping combustion, CLOU=chemical looping with oxygen uncoupling, CLR=chemical looping reforming, CLDR=chemical looping dry reforming, STL=solar thermochemical looping, RWGSCL=reverse water-gas shift chemical looping. The reactions for CLC and CLR are based on methane for simplicity but any general gaseous fossil fuel C_nH_m may be used instead.

Process	Purpose	CCS/CCU?	Original reaction(s)
CLC	Power production	CCS	$CH_4 + O_2 \rightleftharpoons CO_2 + H_2O$
CLOU	Power production	CCS	$C + O_2 \rightleftharpoons CO_2$
CLR	Syngas production	–	$CH_4 + H_2O \rightleftharpoons CO + 3H_2$ $CH_4 + 2H_2O \rightleftharpoons CO_2 + 4H_2$
CLDR	Syngas production	CCU	$CH_4 + CO_2 \rightleftharpoons 2CO + 2H_2$
STL	Syngas production	CCU	$2H_2O \rightleftharpoons 2H_2 + O_2$ $2CO_2 \rightleftharpoons 2CO + O_2$
RWGSCL	Syngas production	CCU	$CO_2 + H_2 \rightleftharpoons CO + H_2O$

Most research on chemical looping has been conducted for chemical looping combustion (CLC, see Fig. 3.3), in which gaseous fossil fuels (generally C_nH_m, often natural gas) are burned without contacting air and the fuel directly. Thus, a pure CO_2 stream is obtained ready for sequestration. The concept of CLC was first proposed in

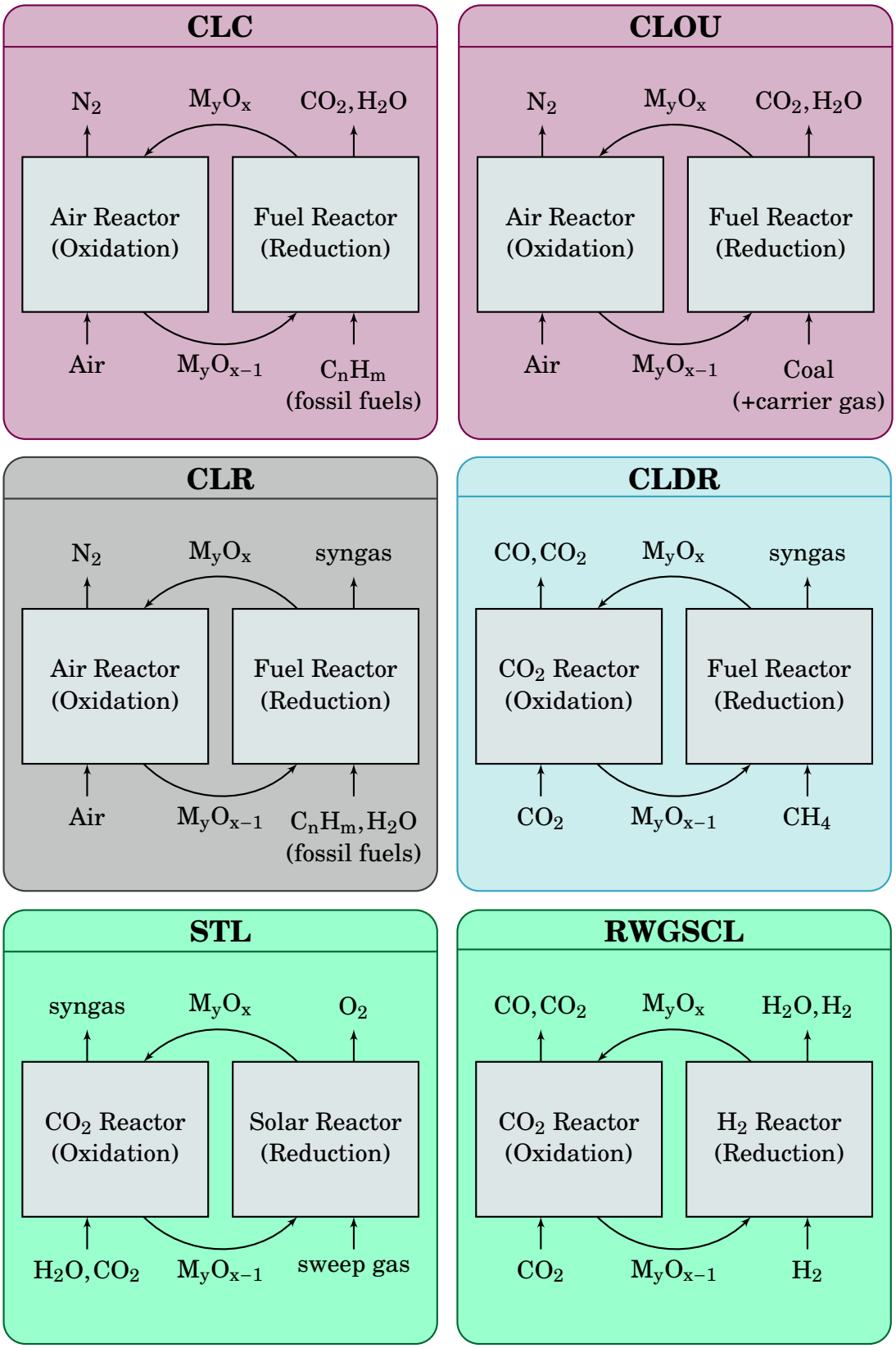

Fig. 3.3 Overview of important chemical looping based processes. Red: Power production with CCS. Gray: Non-sustainable syngas production from fossil fuels. Blue: Non-sustainable syngas production from fossil fuels and CO_2 (CCU). Green: Sustainable syngas production from renewables and H_2O and CO_2 (CCU). Reduction and oxidation refer to the OSM. Further explanation given in Table 3.1.

theory by Ishida et al. in 1987 [95]. CLC was later proven experimentally by Ishida et al. [92–94] and the first pilot-scale experiments in a continuously operated fluidized bed reactor were performed by Lyngfelt et al. [121]. Since then numerous papers have been published on CLC and several reviews summarized important advancements [86, 58, 11].

CLC can be seen as the chemical looping alternative to natural gas power plants and therefore has great potential in reducing the CO_2. However, an even larger fraction of the world's total power production is supplied by coal [1]. Thus, to obtain sequestration-ready CO_2 in coal-fueled power plants as well, the concept of chemical looping combustion was applied to solid fuels, particularly coal (research on CLC with liquid fuels like heavy oils is under way as well [151]). However, as discussed earlier, solid-solid reactions are extremely slow. Therefore, there are two distinct options in which solid fuels can be used in CLC: (1) the solid fuel is gasified before CLC or within the fuel reactor of the CLC plant (in-situ gasification CLC, iG-CLC) [11] (2) using OSMs which release gaseous O_2 which reacts with the solid fuel [126]. The second option which is called chemical looping with oxygen uncoupling (CLOU, see Fig. 3.3) is relatively new and shows superior performance compared to the first option because the slow gasification step can be avoided [11]. A thorough review on CLOU is given by Lyngfelt and Linderholm [120].

CLC and CLOU are mentioned here as very important examples for CCS applications of chemical looping. As research on CLC is far more advanced than on any other chemical looping process, the insights gained from CLC on OSM design and reactor design have been partially adapted to other chemical looping processes. The chemical looping processes discussed in the following are concerned with syngas production instead of power production because syngas production is the main motivation of this thesis. Thus, the CLC process can be modified to produce syngas if the air to fuel ratio is kept low in order to prevent full oxidation of the fuel. This process is the chemical looping alternative to steam reforming and was first proposed by Mattisson and Lyngfelt as autothermal chemical looping reforming (short CLR, see Fig. 3.3) [125]. Just as in CLC, gaseous fuel (C_nH_m) is used in the fuel reactor but ideally the reactor outlet consists mainly of H_2 and CO. CLR has been studied extensively by several research groups in the last decade [150, 50, 160]. The use of solar energy to power the CLR process (solar CLR) has also been studied extensively [109]. The CLR process neither belongs to CCU (CO_2 is not used as a reactant) nor CCS (no sequestration-ready CO_2 stream is produced in CLR).

Another chemical looping process for syngas production emerged recently by applying the chemical looping concept to the dry reforming reaction (see Table 2.1). The chemical looping dry reforming (CLDR, see Fig. 3.3) process was first proposed by Najera et al. [132]. Several other research groups published papers on the process recently [67, 88, 69, 116]. A further intensification option of CLDR was proposed and investigated by Buelens et al. in which different chemical looping cycles are combined in one reactor [32]. The process is called "super-dry reforming" and it potentially yields a higher CO production per mole of methane. Because CO_2 is used as a reactant, the CLDR process is classified as a CCU process. However, the main problem of CLDR from the sustainability perspective is that the majority of methane comes from fossil sources. Producing methane from renewable hydrogen by methanation first and then using that methane for producing syngas by CLDR seems unattractive since renewable hydrogen can be used to produce syngas directly by RWGS or RWGSCL. Using renewable methane from biogas is possible in principle but the CLDR concept requires CO_2 and methane to be separate streams. However, a prior gas phase separation step requires additional energy. Löfberg et al. investigated the possibility of feeding biogas directly to the fuel reactor of the CLDR process [116]. They found that as long as methane is in excess with respect to CO_2 the reactor performance (particularly the selectivity towards H_2) is not significantly decreased. However, the experiments were conducted with highly diluted gas streams and the results have not been verified with real biogas yet. Therefore, the majority of methane for CLDR is expected to come from fossil sources.

In the following solar thermochemical looping (STL) is introduced and compared to the RWGSCL process. STL is based on the idea that the OSM reduction reaction can in principle also be realized by high temperature instead of a chemical reducing agent. In STL concentrated solar energy is used to provide high temperature for OSM reduction (i.e. release of oxygen from the metal). In that respect, STL is different from all the previously discussed chemical looping processes and RWGSCL because STL does not use a chemical reducing agent for OSM reduction (see Fig. 3.3). The first proposal for H_2 production by STL date back to 1977 when Nakamura [133] and Bilgen et al. [27] published similar ideas independently from each other almost simultaneously (Funk and Reinstrom first proposed two-step cycles for hydrogen production in 1966 but not based on solar energy [62]). Back then the idea was not popular as there was yet no social and political pressure to reduce carbon emissions. In the last decades water and CO_2 splitting by the STL process gained renewed interest with extensive research efforts by several groups [165, 163, 9, 65, 106]. However, the first results for

co-splitting both substances to produce syngas were published in 2010 by Stamatiou et al. [161] (an extensive review of syngas production by STL is given by Agrafiotis et al. [12]). Even though STL is very attractive since no additional fuels is needed, new problems arise due to the need for concentrated solar energy. The OSM has to be able to withstand temperatures as high as 2000 K, heat recovery is needed between the reduction and oxidation reactor for efficient operation and low pressure and/or an inert carrier are necessary during OSM reduction for facilitating the oxygen release [118, 12] (OSM reduction at reduced pressure has been shown to be beneficial for the reduction extent of many OSMs [37, 112]).

Summarizing all the chemical looping processes discussed above, RWGS does not stand in direct competition to CCS processes (CLC and CLOU) because it is clearly a CCU process. It also does not compete with CLR or CLDR because RWGSCL uses no fossil fuels for syngas production. Therefore, the only competing technology is STL as it is the only process that uses renewable energy and CO_2 and water to produce syngas. In this sense, it was demonstrates that many chemical looping processes are not directly comparable to RWGSCL since the process constraints are fundamentally different (either their applications or their inputs and outputs are not comparable). Thus, in this thesis RWGSCL is exclusively compared to the traditional RWGS reaction as its benchmark and to STL as its main competitor for sustainable syngas production.

3.4 Oxygen storage materials

All of the chemical looping processes mentioned in Section 3.3 are dependent on an oxygen storage material. Finding suitable OSMs has been one of the key research areas in the last years [86]. Generally, important criteria for suitable OSMs include high reactivity, high oxygen storage capacity, morphological stability (low tendency for attrition as well as agglomeration), low raw material cost, low production cost (easy preparation), low environmental impact, high temperature stability and the ability of the material to be fluidized. [58, 50, 86]. Many of these criteria are conflicting and it is a difficult task to find an OSM that provides a useful trade-off for a specific process.

3.4.1 Classification of OSMs

Due to the large number of possible OSMs, they have been classified according to some of their most relevant properties. In the literature it is often distinguished between volatile vs. non-volatile cycles, pure metal vs. mixed metal oxides and stoichiometric vs. non-stoichiometric cycles.

In volatile cycles the OSM in its oxidized form is typically in solid state whereas the reduced form is in gaseous state. Example materials for these cycles include Zn and Sn. While these cycles provide very high oxygen storage capacities per amount of OSM they suffer from the fact that the volatile products must be quickly quenched to avoid recombination [153, 12]. There has not been found an energetically efficient way to solve this problem, yet [14]. Non-volatile cycles refer to any OSM that remains in the solid state throughout reduction and oxidation. In the following only non-volatile cycles are discussed.

Pure metal oxides are typically easy to synthesize but it has been shown numerous times that pure metal oxides tend to sinter and, thus, do not perform well for prolonged cycling [104, 57]. Pure metal oxides may be doped to obtain mixed metal oxides which show superior resistance to sintering but the synthesis of uniformly distributed mixed oxide materials is more complicated. A typical example are perovskites which have been thoroughly researched in recent years [127, 48, 153, 12].

The distinction between stoichiometric vs. non-stoichiometric cycles refers to the extent that the metal oxide is reduced. In stoichiometric cycles (e.g. iron oxide) the reduction and oxidation of the OSM generally proceeds according to the following reaction

$$\mathrm{A} + \mathrm{M_yO_x} \rightleftharpoons \mathrm{B} + \mathrm{M_yO_{x-1}}, \tag{3.6}$$

where A and B are gas phase components. More specifically, A is a reducing gas and B is an oxidizing gas with regards to the chosen metal/metal oxide pair. The metal oxide undergoes a change from one oxidation state to another and oxygen is released in stoichiometric proportion. In contrast, in non-stoichiometric cycles the OSM releases only small relative amounts of oxygen leading to a non-stoichiometric state according to equation

$$\mathrm{A} + \mathrm{M_yO_x} \rightleftharpoons \mathrm{B} + \mathrm{M_yO_{x-\delta}}. \tag{3.7}$$

Here, δ denotes the non-stoichiometry. Stoichiometric cycles typically yield much higher oxygen storage capacities as more oxygen is released per amount of OSM compared to non-stoichiometric cycles. However, the change of oxidation states in stoichiometric cycles often results in severe morphological changes in the OSMs crystal structure (due to volume contraction and expansion during reduction and oxidation, respectively) potentially decreasing the long term stability of the material [104, 153].In non-stoichiometric cycles the crystal structure is often maintained during oxidation and reduction which results in superior material stability over prolonged cycling [57] (a well known example is CeO_2 [137]). Non-stoichiometric cycles are also associated with faster reaction kinetics compared to stoichiometric cycles [153].

3.4.2 Selection of OSMs for RWGSCL

The selection process for OSMs for a chemical looping process typically starts with thermodynamic screening to identify suitable candidate materials [12] since the thermodynamic boundaries determine the maximum possible performance of any given material. Aspects like reaction kinetics and physicochemical properties (e.g. thermal stability) are equally important but they can be assessed and compared only after extensive measurements on different OSMs since there is a lack of reliable and comparable data in the literature. Conversely, reliable standard thermodynamic data for pure OSMs is readily available which makes thermodynamic screening an attractive method for preliminary OSM selection. Further kinetic investigations are warranted only if the process is found to be thermodynamically feasible and efficient within the given restrictions in the first place [34].

One of the key thermodynamic properties for OSM selection is the oxygen storage capacity (OSC), i.e. the amount of oxygen that an OSM is able to release and take up again upon cycling at given process conditions. The OSC is defined as

$$\mathrm{OSC} = \frac{M_{\mathrm{Ox}} - M_{\mathrm{Red}}}{M_{\mathrm{Ox}}} \tag{3.8}$$

where M_{Ox} and M_{Red} denote the molar mass of the OSM in its oxidized and reduced form, respectively. The maximum possible amount of CO that can be produced from a certain amount of OSM is linked to the OSC value since for every oxygen atom that is taken up by the OSM one molecule of CO can be produced from CO_2 according to

equation (3.4). This value is defined as the CO yield (Y_{CO}) and calculated as follows:

$$Y_{CO} = \frac{OSC}{M_O} \tag{3.9}$$

where M_O is the molar mass of oxygen. The CO yield is expressed as mol_{CO}/kg of material in its oxidized state. Table 3.2 lists the oxygen storage capacity and the CO yield for various commonly used pure oxide OSMs [166, 34]. Ceria has the low-

Table 3.2 Oxygen storage capacity (OSC, as defined by eq. (3.8)) and CO yield (Y_{CO}, as defined by eq. (3.9) of commonly used OSMs.

OSM	OSC	Y_{CO} / mol_{CO}/kg	Classification
$Fe_3O_4 \rightleftharpoons Fe$	0.2764	17.24	Stoichiometric, non-volatile
$FeO \rightleftharpoons Fe$	0.2227	13.92	Stoichiometric, non-volatile
$NiO \rightleftharpoons Ni$	0.2142	13.39	Stoichiometric, non-volatile
$CoO \rightleftharpoons Co$	0.2135	13.35	Stoichiometric, non-volatile
$ZnO \rightleftharpoons Zn$	0.1966	12.29	Stoichiometric, volatile
$SnO \rightleftharpoons Sn$	0.1188	7.42	Stoichiometric, volatile
$Cu_2O \rightleftharpoons Cu$	0.1118	6.99	Stoichiometric, non-volatile
$Mn_3O_4 \rightleftharpoons MnO$	0.0699	4.37	Stoichiometric, non-volatile
$CeO_2 \rightleftharpoons Ce_2O_3$	0.0465	2.91	Stoichiometric, non-volatile
$CeO_2 \rightleftharpoons CeO_{1.9}$	0.0093	0.58	Non-stoichiometric, non-volatile

est OSC and is listed as the only non-stoichiometric OSM. However, perovskites and other non-stoichiometric OSMs have similarly low OSCs compared to stoichiometric OSMs. In the literature, CO yields of approximately $0.15\,mol_{CO}/kg_{CeO_2}$ were experimentally observed for ceria [63] and $0.2-4.0 mol_{CO}/kg$ for state-of-the-art perovskite type materials [52, 48]. Iron oxide exhibits the highest OSC among the listed materials due to the relatively low molar mass of iron compared to the other metals. The theoretical CO yield of the Fe_3O_4/Fe couple is nearly 30 times the value for ceria. High OSC values are beneficial for all chemical looping processes as they potentially lead to a smaller reactor size since more oxygen can be stored per volume.

Another important thermodynamic criterion of material selection for RWGSCL is the reaction equilibrium between the OSM and CO_2 and H_2 according to equations (3.4) and (3.5). Fig. 3.4 and Fig. 3.5 show the Gibbs free energy of reaction, $\Delta_R g$, for the oxidation and the reduction of various OSMs, respectively. The gray area in both Figures indicates the region where the equilibrium conversion of CO_2 (oxidation) or H_2 (reduction) is at least 20%. While this value was chosen arbitrarily, it is important to ensure that a reasonable equilibrium conversion can be expected at least in the-

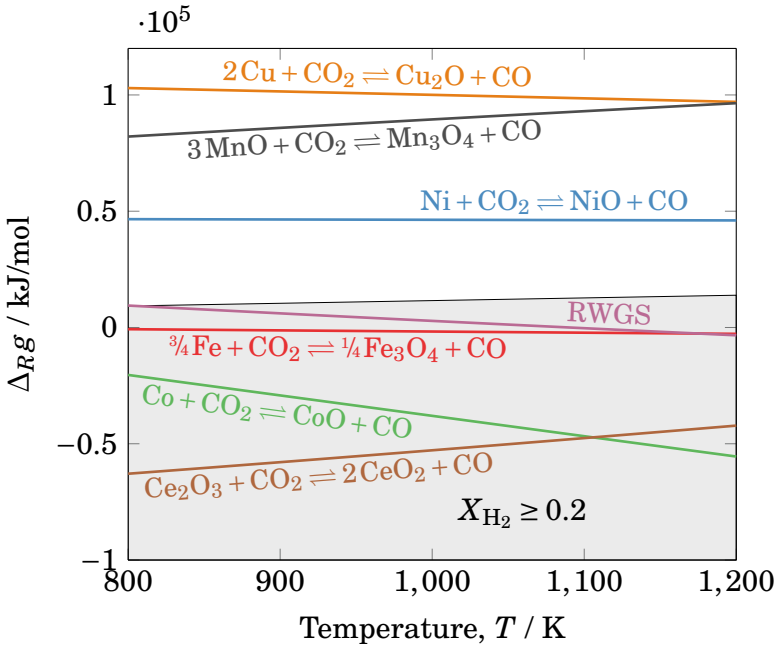

Fig. 3.4 Gibbs free energy of the oxidation reaction (eq. (3.4)) for various commonly used OSMs (see Table 3.2) as a function of temperature. The gray area indicates the region where the CO_2 equilibrium conversion is at least 20%. Thermodynamic data taken from [21, 29]. See Appendix A.1 for detailed calculations.

ory according to thermodynamics. If the equilibrium conversion is too low for either the oxidation or the reduction reaction the OSM must be rejected. As can be seen in Fig. 3.4 some OSM couples like CeO_2/Ce_2O_3 or Cu_2O/Cu have a very promising CO_2 equilibrium conversion for the oxidation reaction (low $\Delta_R g$ values). However, for thermodynamic reasons $\Delta_R g$ of the oxidation and the reduction reaction for every OSM must add up to $\Delta_R g$ of the RWGS reaction. Thus, OSMs that yield a high equilibrium conversion during oxidation must yield a low equilibrium conversion during reduction (at the same temperature, respectively). This can be seen exemplary in Fig. 3.5 for the OSM couples CeO_2/Ce_2O_3 or Cu_2O/Cu which show poor performance during reduction (low $\Delta_R g$ values). Hence, for thermodynamic reasons OSM selection for RWGSCL is a difficult task. One solution would be to allow a different temperature for oxidation and reduction but this gives rise to the problem of heat recovery between both stages (this is one of the main problems of STL as was discussed in Section 3.3). From the perspective of energy efficiency isothermal operation is preferred over temperature swings. Thus, a trade-off solution must be found that yields sufficiently high equilibrium conversions for both the oxidation and reduction reaction of RWGSCL under isothermal conditions. The Fe_3O_4/Fe couple is the only material that lies within

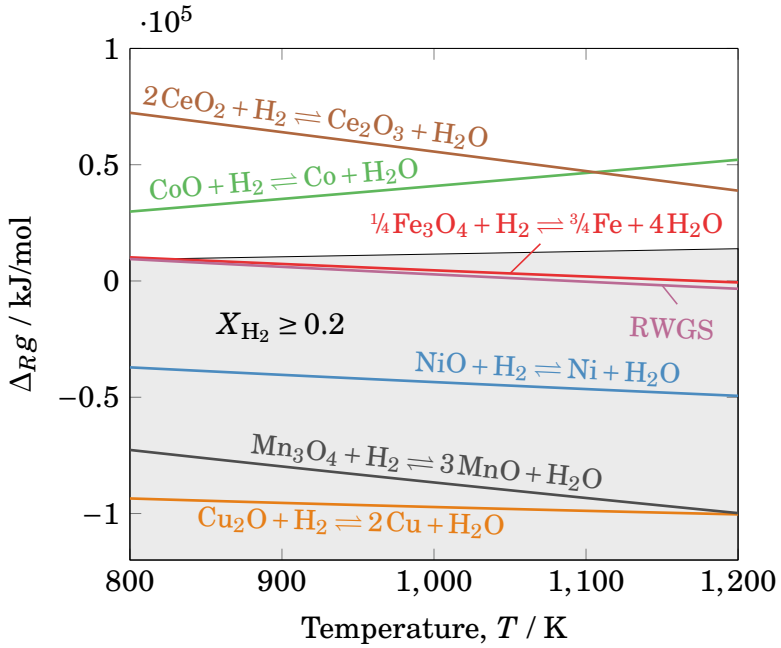

Fig. 3.5 Gibbs free energy of the reduction reaction (eq. (3.5)) for various commonly used OSMs (see Table 3.2) as a function of temperature. The gray area indicates the region where the H_2 equilibrium conversion is at least 20%. Thermodynamic data taken from [21, 29]. See Appendix A.1 for detailed calculations.

the gray area in both Fig. 3.4 and Fig. 3.5 indicating an equilbrium conversion of at least 20% for both reactions. This is what makes iron oxide a promising candidate for RWGSCL in addition to the high oxygen storage capacity. Doped or mixed metal OSMs have not been investigated here because of the lack of reliable thermodynamic data but it can be expected that the values for $\Delta_R g$ are similar to those of the corresponding pure metal OSMs since the amount of dopant is usually small compared to the bulk metal.

Iron oxide was chosen in this work since it is thermodynamically promising, abundantly available, inexpensive and non-toxic [10, 6, 58]. Iron based materials have been investigated extensively in the context of CLC, CLR and STL [57, 166]. Besides being thermodynamically promising for those processes iron based materials also show high resistance to attrition (important for fluidized bed operation) and a low tendency for carbon formation. However, especially for CLC it was shown that reactivity with methane is comparably low and only the phase change between Fe_2O_3 and Fe_3O_4 yields near complete conversion [6, 11]. However, the oxygen storage capacity of the Fe_2O_3 and Fe_3O_4 couple that is often is in CLC is only 0.0334 (or $Y_{CO} = 2.09\,mol_{CO}/kg$). For STL iron based materials are promising but the high tem-

perature necessary for thermal reduction together with the low melting point of FeO (1650 K) severly limits the equilibrium conversion and, therefore, the cycle efficiency [44]. Thus, much work has been devoted to promote the stability of iron oxides (among other OSMs).

The typical approach for stabilizing an OSM is by combining it with an (often inert) material which acts as a support providing a higher surface area for reaction [58]. Furthermore, the mechanical stability can be increased and the volume contraction and expansion upon cycling can be minimized to maintain structural integrity of the OSMs over prolonged cycling [57]. Popular support materials include Al_2O_3, $MgAl_2O_4$, ZrO_2, TiO_2 or SiO_2 among many others [6, 11]. A drawback of using support metals is that the oxygen storage capacity is usually decreased because the support metal is often inert and, therefore, the relative amount of active metal is reduced. However, since sintering is a largely irreversible process it should be avoided at all cost because maintaining structural integrity is much easier than to restore it once it has been destroyed [22].

A thorough analysis of 26 support materials for iron oxide was conducted by Otsuka et al. for clean hydrogen production for PEM fuel cells via the steam-iron process in which iron oxide is repeatedly oxidized and reduced by water and hydrogen, respectively [135]. They found that Al, Mo and Ce were the most promising support materials to preserve the reactivity of the Fe/Fe_3O_4 couple (further oxidation to irons highest oxidation state, Fe_2O_3, is thermodynamically unfavored with water as oxidant). In an effort to further increase the sintering resistance, Galvita et al. investigated different mixtures of ceria-modified iron oxides for CLDR [67]. However, the mixtures were reduced with H_2 (instead of methane) and oxidized with CO_2 making their results highly relevant for RWGSCL. Adding CeO_2 was shown to be beneficial for the activity and stability of pure iron oxide. They found that 80 wt% Fe_2O_3-CeO_2 results in the highest CO yield (twice the value of pure iron oxide) even though 50 wt% Fe_2O_3-CeO_2 and 30 wt% Fe_2O_3-CeO_2 mixtures were slightly more stable upon cycling. Daza et al. compared the CO formation rate (expressed as $mol_{CO}/g_{OSM}/min$) of various literature sources in which H_2 and CO_2 were used for material reduction and oxidation, respectively. They concluded that 80 wt% Fe_2O_3-CeO_2 yields the highest values of all reported sources [47].

In another publication by Galvita et al. for the cyclic water gas shift (CWGS) process (which is the reverse of the RWGSCL process) for clean H_2 production, the effect of $Ce_{0.5}Zr_{0.5}O_2$ on iron oxide was investigated [66]. However, contrary to RWGSCL,

OSM reduction and oxidation was performed with syngas and H_2O, respectively. It was found that a mixture of 80 wt% Fe_2O_3 and 20 wt% $Ce_{0.5}Zr_{0.5}O_2$ yields the highest amount of H_2 (expressed as mol_{H_2}/g_{OSM}). Furthermore, a relatively stable H_2 production over 100 consecutive redox cycles was proven. Deactivation by sintering was significantly reduced compared to pure iron oxide. Although $Ce_{0.5}Zr_{0.5}O_2$ did not increase the oxygen capacity of the material it improves the structural properties compared to those of the pure Fe/Fe_3O_4 couple. ZrO_2 has been known to increase the micro-structural stability against sintering [105], whereas CeO_2 increases material activity, enhancing the rate of reaction [67].

Given the promising results of 80 wt% Fe_2O_3-$Ce_{0.5}Zr_{0.5}O_2$ (see [66]) for the CWGS process, the material was chosen as an OSM for RWGSCL in this work.

3.5 Conclusions

This chapter gave an introduction to the chemical looping concept and some of the most important applications. The RWGSCL was explained and compared to other chemical looping processes that are relevant within the scope of this thesis. Furthermore, it was argued why STL is the only true competitor for RWGSCL. In the last part of this chapter necessary properties of oxygen storage materials were discussed. The OSMs were classified into different groups according to their properties and a framework for the rational selection of OSMs for the RWGSCL process based on thermodynamic principles was presented. It was shown how numerous the potential material candidates can be for a single chemical looping process like RWGSCL. Since the choice of the OSM is of critical importance the majority of the past and current research activities on chemical looping technology is on new and promising materials. However, equally important are considerations on energy efficiency and reactor design as well as operation. Thus, the next chapters of this thesis address those aspects rather than materials research.

4 | Efficiency analysis

To go wrong in one's own way is better than to go right in someone else's.

Fyodor Dostoyevsky

In the previous chapter thermodynamic principles were used to establish a rational framework for OSM selection. It was shown that the thermodynamic properties of iron-based OSMs are the most promising for RWGSCL. Reported experimental results from the literature verified the theoretical findings [47]. Since the process thermodynamics and kinetics are dictated by the OSM for every chemical looping process, the selection of 80 wt% Fe_2O_3-$Ce_{0.5}Zr_{0.5}O_2$ as OSM for RWGSCL was the first important step in this thesis. Further investigations into RWGSCL can only be conducted after the OSM has been selected. The work presented in this chapter has been published previously in [176] and is reproduced with permission of Wiley and Sons.

In this chapter, the RWGSCL process is analyzed within the scope of sustainable syngas production based on thermodynamic principles to get a first estimate of the overall possible process efficiency. Energy efficiency is a crucial factor in CO_2 utilization processes since they are naturally energy intensive. Therefore, energy efficiency must be optimized to facilitate a future mass market adoption of CO_2 utilization processes. One method to assess the energy efficiency is the analysis based on the first and second law of thermodynamics. The results give the maximum thermodynamic potential of a process and reveal the process steps which contribute most to exergy losses.

While thermodynamic analysis has been applied extensively to syngas production processes based on STL [152, 33, 20, 108, 118, 65], a systematic comparison to RWGS or RWGSCL has not yet been conducted. Furthermore, the direct comparison of energy efficiencies for syngas production by STL is difficult because each research

group defines the system boundaries differently. An analysis with comparable system boundaries will enable us to identify the most promising concepts for energy efficient CO_2 conversion to syngas.

In this chapter, process systems are designed for the conventional RWGS and the RWGSCL process for syngas production from CO_2 and renewable energy (solar). The systems are optimized in terms of energy efficiency and the results are compared and discussed. Special emphasis is put on the gas separation after reaction. While some downstream operations (e.g. Fischer-Tropsch) are not affected by remaining CO_2, other applications require the removal of CO_2 and/or H_2O from syngas. Even though it has been shown that the separation of reactants from the products affects the overall process efficiency [102, 103], gas separation is ignored in the efficiency calculation in many studies. Here, literature data is used for separation processes to include gas separation in the analysis. The aim is to estimate realistic efficiencies for sustainable syngas production systems using CO_2.

For reasons of simplicity and due to a lack of reliable thermodynamic data for $Ce_{0.5}Zr_{0.5}O_2$, the analysis presented in this chapter is based on pure iron oxide as an OSM (thermodynamic data on iron and its oxides is readily available in the literature [80, 29]). Since iron oxide makes up the majority (80 wt%) of the OSM it is assumed that the effects of $Ce_{0.5}Zr_{0.5}O_2$ on the thermodynamic properties of iron oxide can be neglected as a first estimate in this part of this thesis. The effects of $Ce_{0.5}Zr_{0.5}O_2$ on the structural stability and the reaction kinetics of iron oxide are discussed in the following chapter.

4.1 Process systems

4.1.1 Reverse water-gas shift (RWGS)

A flow sheet of the conventional reverse water-gas shift (RWGS) process for CO_2 conversion to syngas is depicted in Fig. 4.1. The heat and electrical power for the process is supplied by solar energy. Water (1) is electrolyzed to produce H_2 (2a), which reacts with CO_2 (3) in the RWGS unit to form a mixture of syngas, water and CO_2 (4), according to the following reaction:

$$\text{RWGS:} \qquad H_2 + CO_2 \rightleftharpoons H_2O + CO \qquad \Delta h_R(1073\,\text{K}) = 36.84\,\text{kJ/mol} \qquad (4.1)$$

The majority of water is removed by condensation in a flash unit (5b). The remaining gas (5a) is separated in a separation unit to yield pure component streams. Residual water after the flash unit is assumed to be removed in the gas phase (6d). Unreacted CO_2 is recycled to the RWGS unit (6b). To obtain syngas with a low H_2/CO ratio, H_2 might be recycled to the reactor (6c). In the conventional RWGS process, the H_2/CO ratio of the product syngas (8) can be adjusted either by varying the feed H_2/CO_2 ratio or by keeping the initial H_2/CO_2 ratio constant and adding additional H_2 after the reaction (7). By definition, the arrow of the heat streams always points toward the units. This, however, does not imply the actual direction of heat transfer (heat flow out of a unit is signed negative).

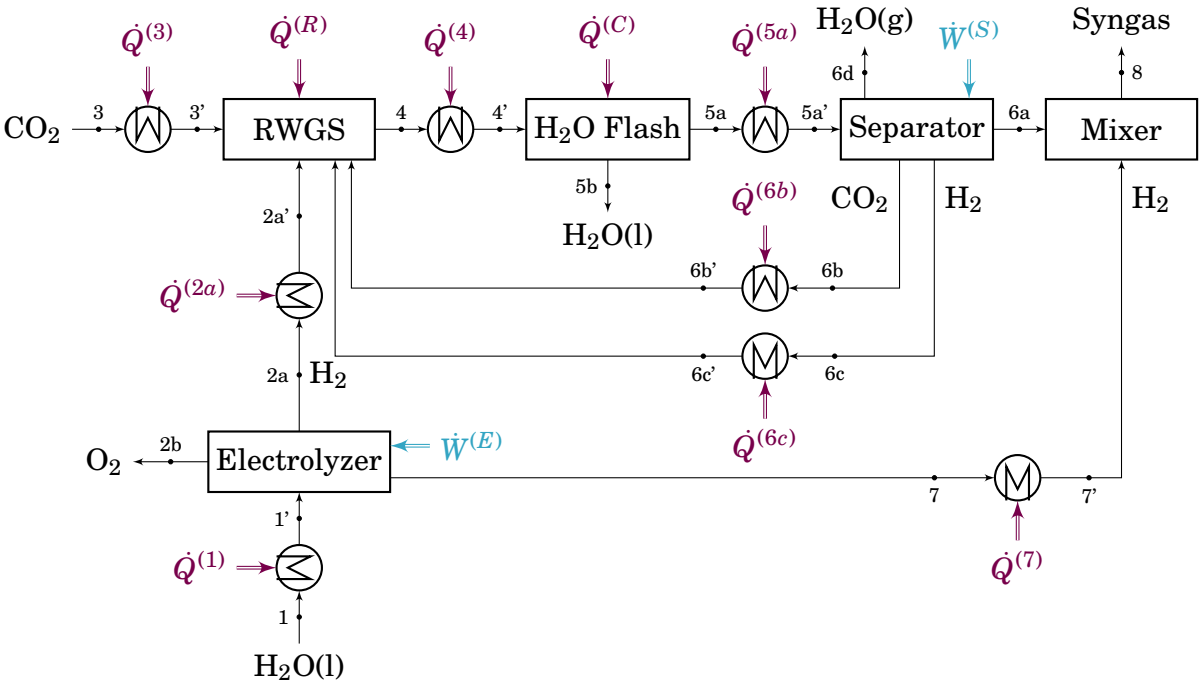

Fig. 4.1 Idealized process system for syngas production by RWGS. Figure adapted from [176] with permission of Wiley and Sons.

4.1.2 Reverse water-gas shift chemical looping (RWGSCL)

Fig. 4.2 shows a flow sheet for the RWGSCL process. While there are several similarities to the conventional RWGS process, some crucial differences do exist. Note, however, that the system boundaries remain unchanged allowing fair process comparison. In the electrolyzer, H_2 (2a) is produced by electrolysis. Since the RWGSCL

unit is a two-stage process with spatially separated reactions, CO_2 and H_2 enter the reactor at separate locations (CO_2 for oxidation and H_2 for reduction of the material). For the RWGSCL reactor, the reaction equations can be expressed as

$$\text{Oxidation:} \quad 3/4\,\text{Fe} + \text{CO}_2 \rightleftharpoons 3/4\,\text{FeO}_{4/3} + \text{CO} \qquad \Delta h_R(1073\,\text{K}) = 8.98\,\text{kJ/mol} \tag{4.2}$$

$$\text{Reduction:} \quad 3/4\,\text{FeO}_{4/3} + \text{H}_2 \rightleftharpoons 3/4\,\text{Fe} + \text{H}_2\text{O} \qquad \Delta h_R(1073\,\text{K}) = 27.86\,\text{kJ/mol} \tag{4.3}$$

Equations (4.2) and (4.3) are expressed using $FeO_{4/3}$ instead of Fe_3O_4 to make it easily visible that they add up to yield the RWGS reaction (eq. (4.1)). Similarly to the RWGS reaction, the reactions considered for the RWGSCL process are equilibrium limited (discussed in detail in Section 4.2.3). The most simple RWGSCL reactor consists of at least two fixed bed reactors: one for the reduction and one for the oxidation reaction. Upon complete conversion of solid iron (oxide) the gas flows to the reactors are switched, ideally allowing a quasi-continuous operation. More complex reactor designs are currently investigated to enhance reaction kinetics and heat transfer [63, 54]. The oxidation reactor outlet (4a) contains a mixture of CO_2 and CO, which must be separated. The unreacted CO_2 is fed back to the oxidation stage of reactor (5b). The reduction reactor outlet (4b) contains H_2O, which is separated by condensation (6a), and H_2, which is recycled to the reduction stage of the reactor (6b). Due to phase equilibrium in the flash unit, the hydrogen stream (6b) is saturated with water vapor. The H_2/CO ratio of the syngas is adjusted by adding H_2 (7) to the CO stream (5a) to yield the desired product syngas (8). It is also conceivable to use some fraction of stream (6b) to adjust the H_2/CO ratio in the mixer. However, H_2 from stream (7) is always preferable because it bypasses heating and cooling in the reactor/separator sequence and, thus, contributes less to the total energy demand.

4.2 Thermodynamic model

Modeling of an ideal process systems entails a number of assumptions that are discussed in the following. All gases are treated as ideal gases. Potential and kinetic energies are neglected. The gas composition in the heaters and coolers remains unchanged (no chemical reactions occur). The systems operate at atmospheric pressure. Specific assumptions for each process unit are discussed in the following.

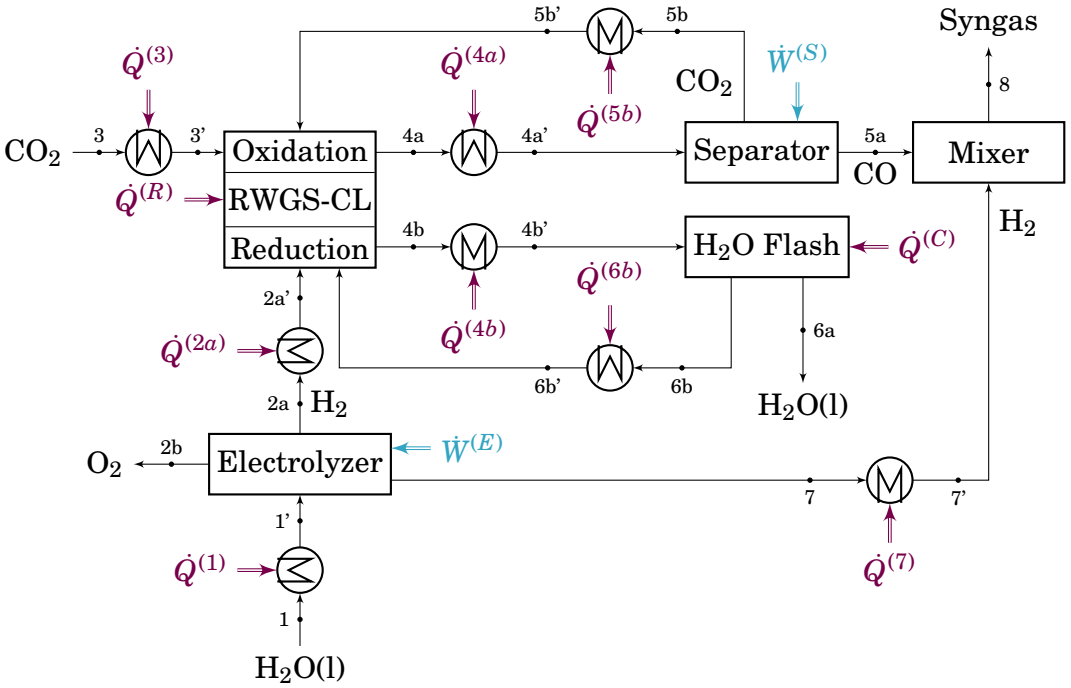

Fig. 4.2 Idealized process system for syngas production by RWGSCL. Figure adapted from [176] with permission of Wiley and Sons.

4.2.1 Solar energy collection

It is assumed that high temperature heat from solar energy is readily available, which supplies the necessary heat for the process units. Solar energy ($\dot{Q}^{(\text{solar})}$) is assumed to be absorbed by a black body receiver. Losses in solar collection and thermal losses due to reradiation ($\dot{Q}^{(\text{rerad})}$) are accounted for by the solar energy collection (SEC) efficiency, which is defined as

$$\eta_{\text{SEC}} = \frac{L_H(\dot{Q}^{(\text{solar})} - \dot{Q}^{(\text{rerad})})}{\dot{Q}^{(\text{solar})}} = \frac{L_H\left(G_0 C - \sigma(T^{(\text{R})})^4\right)}{G_0 C}. \tag{4.4}$$

Here, L_H in an adjustable parameter for the total heat loss of the system and $\dot{Q}^{(\text{rerad})}$ accounts for losses due to reradiation. Heat loss factors of $L_H = 0.8$ [20] and 0.9 [33] were used in studies for solar thermochemical processes at temperatures above 1273 K. The heat losses are assumed to be lower in this analysis since the highest temperature in the reactor is 1073 K. Thus, a heat loss factor of $L_H = 0.95$ is assumed. G_0 is the nominal solar flux incident on the concentrator. Its value is assumed to be 1 kW/m^2 [20] which is slightly lower than the mean solar irradiance on earth (1.37 kW/m^2 [73]). The solar concentration factor C is set to 3000 suns, which

can be achieved by Dish-Sterling concentrators [123]. Reradiation losses depend on the temperature of the reactor unit ($T^{(\mathrm{R})}$) [20]. It should be noted, however, that this approximation assumes that all solar heat to the system is supplied at reactor temperature (1073 K) even though some of the process heat is required at a lower temperature. This leads to a slight overestimation of reradiation losses.

4.2.2 Electrolysis

Water for electrolysis is supplied at ambient temperature ($T^{(0)} = 298\,\mathrm{K}$) and electrolysis is performed at 353 K which is typical for alkaline or PEM electrolyzers [60, 35]. Their actual specific energy demand in terms of electrical energy is approximately $5.5\,\mathrm{kWh/Nm^3_{H_2}}$ or $444\,\mathrm{kJ/mol_{H_2}}$ [35]. This includes purification of the produced hydrogen up to 99.8% [187]. Therefore, the produced hydrogen can be considered practically pure for the efficiency analysis. The energy for electrolysis is assumed to be generated from solar energy by a Dish-Sterling power system with a solar-to-electricity (StE) efficiency of $\eta_{\mathrm{StE}} = 0.25$ [123]. Thus, the corresponding solar heat required for the electrolyzer ($\dot{Q}^{(\mathrm{E})}$) is given by

$$\dot{Q}^{(\mathrm{E})} = \frac{\dot{W}^{(\mathrm{E})}}{\eta_{\mathrm{StE}}} = \frac{444\,\mathrm{kJ/mol_{H_2}}(\dot{N}^{(2\mathrm{a})}_{\mathrm{H_2}} + \dot{N}^{(7)}_{\mathrm{H_2}})}{\eta_{\mathrm{StE}}}. \tag{4.5}$$

4.2.3 Reactor

Concentrated CO_2 is assumed to be available at 313 K, which is preheated to the reactor temperature $T^{(\mathrm{R})}$ prior to entering the reactor. It is assumed that chemical equilibrium is achieved in the reactor for RWGS and RWGSCL. The heat that must be supplied to the RWGS reactor is calculated by

$$\dot{Q}^{(\mathrm{RWGS})} = \Delta_R h^{(\mathrm{RWGS})} \dot{\xi}^{(\mathrm{RWGS})}, \tag{4.6}$$

where $\dot{\xi}^{(\mathrm{RWGS})}$ is the reaction extent per unit time of the RWGS reaction. For RWGSCL, the heat of reaction for oxidation and reduction can be calculated analogously:

$$\dot{Q}^{(\mathrm{RWGSCL,Ox})} = \Delta_R h^{(\mathrm{RWGSCL,Ox})} \dot{\xi}^{(\mathrm{RWGSCL,Ox})} \tag{4.7}$$

$$\dot{Q}^{(\mathrm{RWGSCL,Red})} = \Delta_R h^{(\mathrm{RWGSCL,Red})} \dot{\xi}^{(\mathrm{RWGSCL,Red})} \tag{4.8}$$

The overall heat demand of the RWGSCL reactor includes the heat required for the oxidation and reduction reaction:

$$\dot{Q}^{(\mathrm{RWGSCL})} = \dot{Q}^{(\mathrm{RWGSCL,Ox})} + \dot{Q}^{(\mathrm{RWGSCL,Red})} \tag{4.9}$$

For both RWGS and RWGSCL, the reactor temperature is set to 1073 K, which is typical for iron oxide. This temperature ensures adequate rates of reaction while minimizing temperature related problems (e.g. material sintering). In RWGSCL, both reactors operate at 1073 K. The RWGS reaction and RWGSCL reactions are

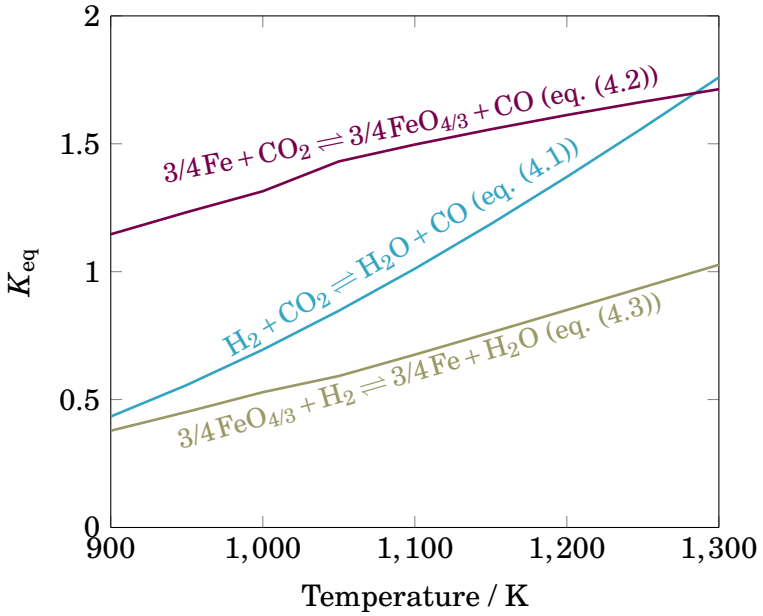

Fig. 4.3 Temperature dependence of the equilibrium constant K_{eq} for the RWGS reaction (eq. (4.1)) and for the RWGSCL reactions with iron oxide (eq. (4.2) and (4.3)). Figure adapted from [176] with permission of Wiley and Sons.

mildly endothermic and the heat of reaction depends weakly on the temperature. The equilibrium constants (K_{eq}) for the RWGS reaction and the RWGSCL reactions are depicted in Fig. 4.3 as a function of temperature. For $T > 1093\,\mathrm{K}$, the reaction equilibrium for the RWGS reaction (eq. (4.1)) lies on the product side ($K_{\mathrm{eq}} > 1$). For the

oxidation reaction of RWGSCL (eq. (4.2)) this is the case for the whole range of temperature inspected, while the equilibrium of the reduction reaction (eq. (4.3)) lies on the product side only at temperatures above 1273 K. The higher K_{eq} of the oxidation reaction in RWGSCL results in a higher equilibrium CO_2 conversion and lower CO_2 content in the CO/CO_2 mixture compared to the conventional RWGS reaction. This comes at the cost of decreased conversion of H_2 in the reduction reaction. However, since a H_2/H_2O mixture is easier to separate (e.g. by condensation) than a CO/CO_2 mixture, this gives a potential advantage of RWGSCL over RWGS, most notably for the production of pure CO.

4.2.4 H_2O flash

Water is separated from the product gas by condensation at 313 K. The gas and liquid outlet streams are assumed to be in phase equilibrium. For the RWGS process, the energy released during condensation can be calculated from the enthalpy balance according to

$$\dot{Q}^{(\mathrm{C})} = -\dot{H}^{(4')} + \dot{H}^{(5\mathrm{a})} + \dot{H}^{(5\mathrm{b})}, \tag{4.10}$$

where $\dot{H}$ is the enthalpy flow which can be calculated from the molar flow $\dot{N}$ and the molar enthalpy $h(T)$ by

$$\dot{H} = \dot{N} h(T). \tag{4.11}$$

For the RWGSCL process, an analogous relationship is used (see Fig. 4.2).

4.2.5 Separator

For an ideal separation unit with one inlet stream and N_{out} outlet streams, the minimum thermodynamic energy of separation (reversible energy) under isothermal and isobaric conditions is given by

$$\dot{W}_{\mathrm{rev}}^{(\mathrm{S})} = -RT\left(\sum_{\alpha}^{N_{\mathrm{C}}} \dot{N}_\alpha \ln x_\alpha - \sum_{i}^{N_{\mathrm{out}}} \sum_{\alpha}^{N_C} \dot{N}_\alpha^{(i)} \ln x_\alpha^{(\mathrm{i})}\right), \tag{4.12}$$

where N_C is the number of components in each stream. However, the reversible work $\dot{W}_{\text{rev}}^{(\text{S})}$ is a poor estimate of the actual work needed to separate gases [179, 51], which depends strongly on the specific separation technology that is used (e.g. absorption, adsorption or distillation). The ratio of the reversible energy of separation to the actual energy can be expressed by the separation efficiency, defined as

$$\eta_{\text{S}} = \frac{\dot{W}_{\text{rev}}^{(\text{S})}}{\dot{W}_{\text{act}}^{(\text{S})}}. \tag{4.13}$$

The separation efficiency for real separation processes lies in the range of $5-40\%$ [87]. House *et al.* [87] and Wilcox [179] reviewed the separation efficiencies for typical separation processes in industry. Based on this information, we estimate the separation efficiency as a function of the initial mole fraction of the component that is separated. While the data points for the separation efficiency span a wide range, the trend is that a low initial mole fraction leads to a low separation efficiency. In Fig. 4.4, the data points are shown together with the least squares fit of a nonlinear model $\eta_{\text{S}} = f(x_\alpha)$. The correlation $\eta_{\text{S}} = f(x_\alpha)$ is used to estimate the actual energy from the reversible energy of a separation process. The actual energy of separation is assumed to be generated by solar energy with a StE efficiency of $\eta_{\text{StE}} = 0.25$ [123]. Thus, the actual energy demand for separation can be expressed in terms of the solar heat required by

$$\dot{Q}^{(\text{S})} = \frac{\dot{W}_{\text{rev}}^{(\text{S})}}{\eta_{\text{S}}\eta_{\text{StE}}}. \tag{4.14}$$

The gases are assumed to be separated at a temperature of 313 K, which is typical for a monoethanolamine (MEA) absorption process for CO_2 separation [179].

4.2.6 Heating and cooling

Heating and/or cooling of the process streams is necessary since each unit operates at a specific temperature. The energy for heating is supplied by solar energy. The streams and the flash unit ($\dot{Q}^{(\text{C})}$) are cooled by water at ambient temperature. Since all process streams have temperatures ≥ 313 K, water at 298 K can be used for cooling and expensive refrigeration systems are not necessary. Assuming that the energy demand for pumping the water is negligible, cooling of the process streams does not affect the StS efficiency. The overall amount of energy required for stream heating is

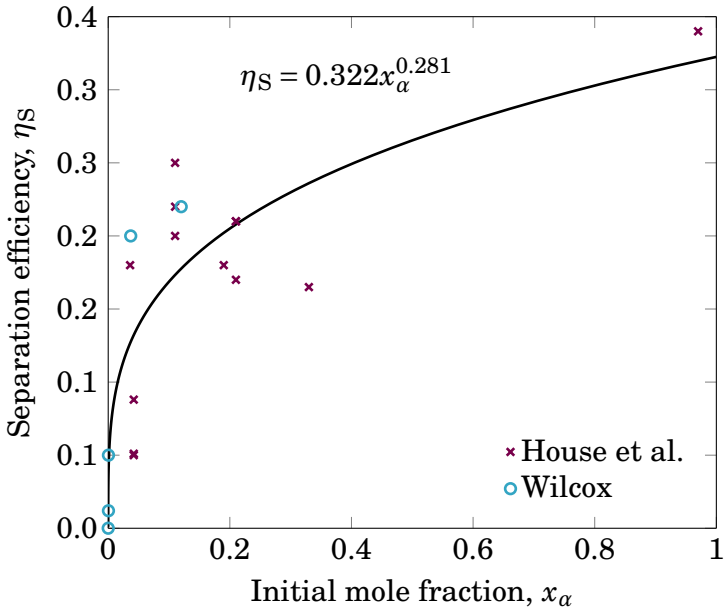

Fig. 4.4 Separation efficiency η_S as a function of the initial mole fraction of the component to be separated. Literature data for real separation process taken from House *et al.* [87] and Wilcox [179]. Figure adapted from [176] with permission of Wiley and Sons.

summarized by $\dot{Q}^{(\text{Stream})}$, which is calculated by

$$\dot{Q}^{(\text{Stream})} = \sum_{k}^{N_S} \dot{Q}^{(\text{k})}, \tag{4.15}$$

where k is the identifier of the heater and N_S is the total number of streams to be heated. For RWGS, $k = \{1, 2\text{a}, 3, 6\text{b}, 6\text{c}\}$ (see Fig. 4.1) and for RWGSCL, $k = \{1, 2\text{a}, 3, 5\text{b}, 6\text{b}\}$ (see Fig. 4.2). The heat demand for heater k can be calculated by

$$\dot{Q}^{(k)} = \dot{N}^{(k)} \int_{T^{(k)}}^{T^{(k')}} c_p^{(k)}(T) \mathrm{d}T, \tag{4.16}$$

where $c_p^{(k)}(T)$ is the temperature dependent molar heat capacity of stream k, and $T^{(k)}$ and $T^{(k')}$ are the temperatures before and after the heater/cooler, respectively.

4.2.7 Mixer

It is assumed that no heat is produced during mixing since the enthalpy change of mixing is zero for ideal gases.

4.3 Results and discussion

The idealized process systems are evaluated using the solar-to-syngas (StS) efficiency η_{StS}, which is defined as

$$\eta_{\mathrm{StS}} = \frac{\eta_{\mathrm{SEC}} \left(\dot{N}_{\mathrm{H_2}}^{(8)} \mathrm{HHV}_{\mathrm{H_2}} + \dot{N}_{\mathrm{CO}}^{(8)} \mathrm{HHV}_{\mathrm{CO}} \right)}{\dot{Q}^{(\mathrm{E})} + \dot{Q}^{(\mathrm{Stream})} + \dot{Q}^{(\mathrm{R})} + \dot{Q}^{(\mathrm{S})}} \tag{4.17}$$

where HHV is the higher heating value and $\dot{Q}^{(\mathrm{E})}$, $\dot{Q}^{(\mathrm{Stream})}$, $\dot{Q}^{(\mathrm{R})}$ and $\dot{Q}^{(\mathrm{S})}$ are the energy demands for the electrolyzer, stream heating, reactor heating and gas separation, respectively. It is convenient to express these terms as dimensionless energy factors F by normalizing each $\dot{Q}$ by the energy stored chemically (HHV) in the product syngas [96]:

$$\eta_{\mathrm{StS}} = \frac{\eta_{\mathrm{SEC}}}{F^{(\mathrm{E})} + F^{(\mathrm{Stream})} + F^{(\mathrm{R})} + F^{(\mathrm{S})}} \tag{4.18}$$

The relative magnitude of each F factor indicates which process contributes most to the total energy demand.

The idealized process systems are optimized to yield the maximum StS efficiency, η_{StS}. The optimization variables are the molar flows $\dot{N}_{\alpha}^{(i)}$ where i denotes streams 1 to 8 and the reaction extent of the electrolyzer ($\dot{\xi}^{(\mathrm{E})}$) and the reactor ($\dot{\xi}^{(\mathrm{R})}$). They constitute a nonlinear programming problem (NLP) which is solved with the *fmincon* routine using the standard sequential linear programming (SQP) solver in MATLAB:

$$\begin{aligned} \min_{\dot{N}_{\alpha}^{(i)}, \dot{\xi}^{(\mathrm{E})}, \dot{\xi}^{(\mathrm{R})}} \quad & 1/\eta_{\mathrm{StS}} \\ \text{s.t.} \quad & \text{Mass balances} \\ & \text{Eq. (4.6) to (4.18)} \\ & 0 \leq \dot{N}_{\alpha}^{(i)} \leq 1\,\mathrm{mol/s} \\ & 0 \leq \dot{\xi}^{(\mathrm{E})} \leq 1\,\mathrm{mol/s} \\ & 0 \leq \dot{\xi}^{(\mathrm{R})} \leq 1\,\mathrm{mol/s} \end{aligned} \tag{4.19}$$

Pinch analysis was included as a subroutine within the optimization problem for heat integration of the streams to obtain a minimum external heating and cooling demand [100]. Thus, the influence of heat integration on the optimal solution could be investigated. For the case with heat integration, $\dot{Q}^{(\mathrm{Stream})}$ includes only the heat that has to

be provided by external sources. The considered heating and cooling duties for heat integration were all $\dot{Q}$ except for $\dot{Q}^{(\mathrm{R})}$ since reactor heating is considered separately. The minimum temperature difference at the pinch point was set to 10 K. The heat integration network depends on the optimal solution and is, therefore, not depicted in Fig. 4.1 or Fig. 4.2.

4.3.1 Optimization results

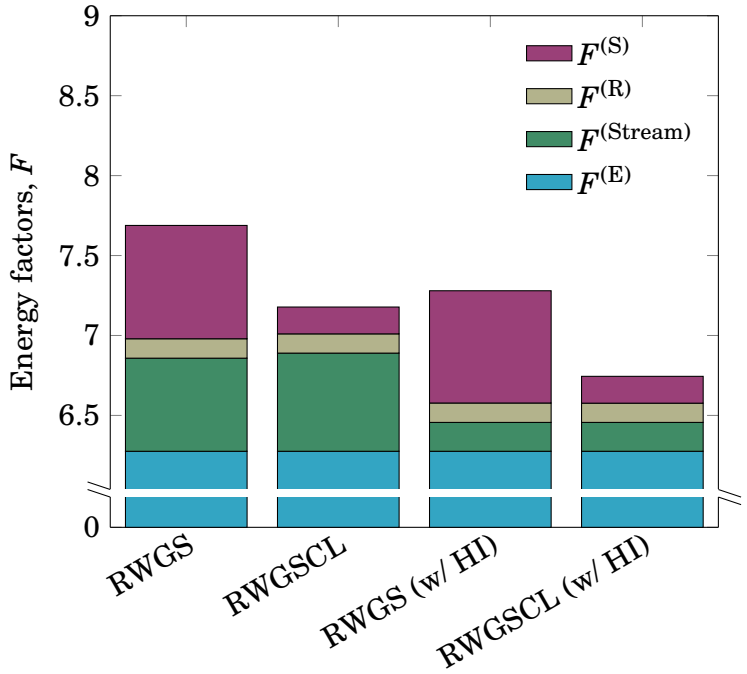

Fig. 4.5 Dimensionless energy factors F for pure CO production. RWGS and RWGSCL refer to the process schemes in Fig. 4.1 and Fig. 4.2, respectively. Results with heat integration are denoted by (w/ HI). Figure adapted from [176] with permission of Wiley and Sons.

Fig. 4.5 shows the F values for pure CO production by RWGS and RWGSCL with and without gas phase heat integration. With a value of $F^{(\mathrm{E})} = 6.27$, the electrolyzer is dominating the overall energy demand in all cases contributing to more than 80%. This is mainly due to the low StE efficiency for electricity generation. The second largest contributor to the overall energy demand is stream heating ($F^{(\mathrm{Stream})}$) with approximately 8% for the cases without heat integration. The energy demand for reactor heating ($F^{(\mathrm{R})}$) only accounts for approximately 2% of the total energy demand. Significant reductions in energy consumption can be achieved in the reactor/separator sequence. For the RWGSCL process, $F^{(\mathrm{S})}$ is reduced by 77% as compared to the

RWGS process due to the partial gas separation in the RWGSCL reactor. Furthermore, heat integration leads to a reduction of $F^{(\mathrm{Stream})}$ by $\approx 70\%$ for both processes. $F^{(\mathrm{Stream})}$ accounts for $\approx 1.5\%$ of the total energy demand for the cases with heat integration. A reduction of 54% in the sum of $F^{(\mathrm{Stream})}$, $F^{(\mathrm{R})}$ and $F^{(\mathrm{S})}$ can be achieved by using RWGSCL compared to RWGS (both cases with heat integration). RWGSCL without heat integration has a lower overall energy demand than RWGS with heat integration. Thus, RWGSCL is significantly more efficient in the reactor/separator sequence of the process. This, however, comes at the cost of a more complicated reactor design.

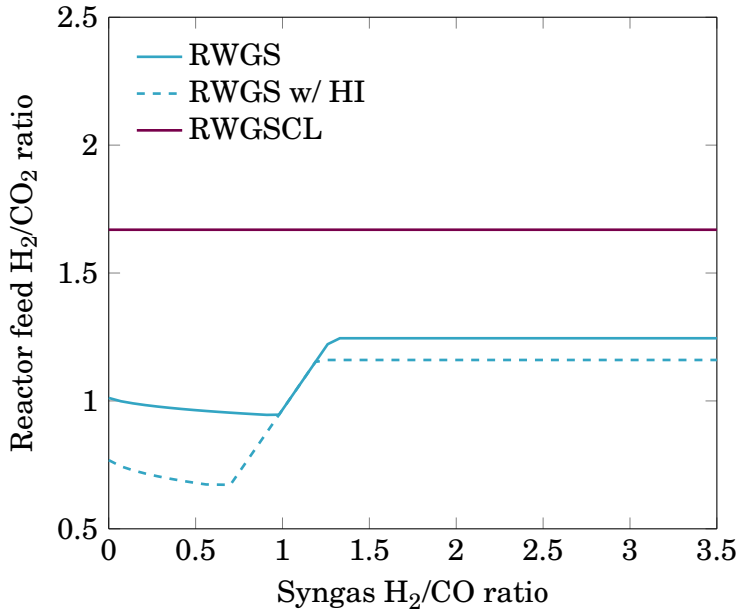

Fig. 4.6 Optimal reactor feed H_2/CO_2 ratios for maximal StS efficiency according to eq. (4.19). The feed consists of all input streams into the reactor, including recycle streams. RWGS and RWGSCL correspond to the process schemes Fig. 4.1 and Fig. 4.2, respectively. The line for RWGSCL with heat integration is identical to the RWGSCL line. Figure adapted from [176] with permission of Wiley and Sons.

The optimal H_2/CO_2 ratios into the reactor are illustrated in Fig. 4.6. In the RWGSCL process, the optimal reactor feed ratio is constant for all syngas H_2/CO ratios because the reaction extents for oxidation and reduction are coupled to ensure that the same amount of solid material is oxidized and reduced, which is necessary for quasi-stationary operation. Therefore, a constant value of 1.67 is obtained for the cases with and without gas phase heat integration. For the RWGS process, the optimal H_2/CO_2 ratio in the reactor depends on the desired H_2/CO ratio. In the case without heat integration, the optimal reactor feed ratio declines slightly from 1 to

approximately 0.95 for H_2/CO ratios between 0.0 and 1.0. This leads to an increase in the CO_2 mole fraction of the product stream. This is beneficial for the overall efficiency, since the separation efficiency is higher at higher CO_2 concentrations in the separator inlet. The reactor feed ratio increases to approximately 1.25 for H_2/CO ratios > 1. For H_2/CO ratios > 1.4, the reactor feed ratio remains constant and higher H_2/CO ratios are achieved by adding H_2 *via* stream (7) after the reaction, which is beneficial for StS efficiency, as it leads to high degrees of conversions for H_2 and CO_2 in the reactor and therefore minimizes the heat needed for reheating reactants in the recycle. The results indicate that for the RWGS process without heat integration a reactor feed H_2/CO_2 ratio of approximately 1.25 is beneficial for the production of syngas with H_2/CO > 1.4. With heat integration included, the optimal solution to equation (4.19) is qualitatively similar to the optimal solution without heat integration but shifted to lower reactor feed H_2/CO_2 ratios. At these H_2/CO_2 ratios, optimal heat integration is achieved and external heat supply is minimized.

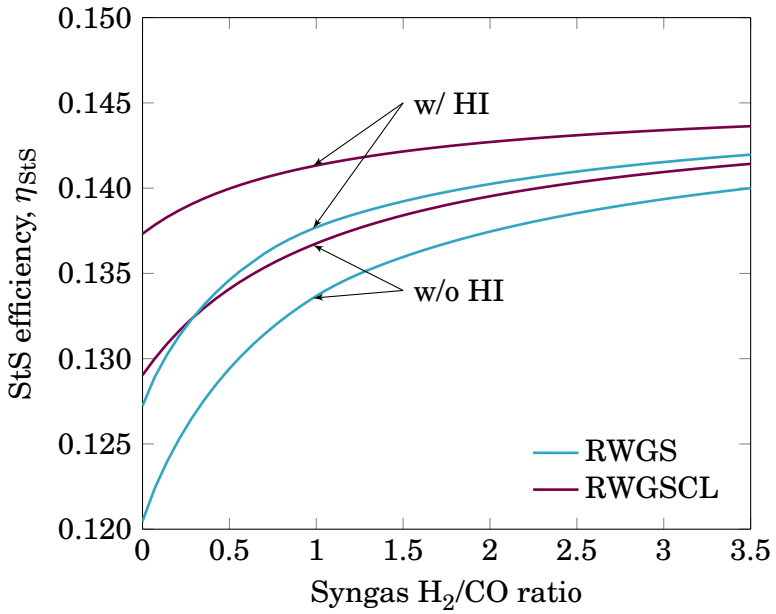

Fig. 4.7 StS efficiency η_{StS} with (w/) and without (w/o) gas phase heat integration (HI) as a function of syngas H_2/CO ratio. Lines for RWGS and RWGSCL correspond to the process schemes in Fig. 4.1 and Fig. 4.2, respectively. Figure adapted from [176] with permission of Wiley and Sons.

The StS efficiency obtained by optimization with and without gas phase heat integration is shown in Fig. 4.7. With heat integration enabled, the StS efficiency varies between 0.127 and 0.142 for RWGS and between 0.137 and 0.144 for RWGS depending on the desired syngas H_2/CO ratio. With the assumptions made in this analysis,

the solar energy collection efficiency is $\eta_{SEC} = 0.926$, i.e. 7.4% of the solar energy input is lost due to reradiation and heat loss in the process. The StS efficiency is increasing with increasing H_2/CO ratios in all cases because the energy demand for gas separation and reheating of reactants decreases as less CO is formed. The maximum StS efficiency for each process is obtained at syngas H_2/CO ratios of 3.5. The StS efficiency at all syngas ratios is dictated by the low overall efficiency of H_2 production. The RWGSCL process achieves an StS efficiency up to one percent point higher than compared to the RWGS process for pure CO production. However, the difference decreases to 0.2 percent points for syngas with H_2/CO = 3.5. Thus, the advantage of inherent gas separation in the RWGSCL reactor is most pronounced for the production of pure CO. Despite the dominating influence of H_2 production on the energy demand, heat integration leads to efficiencies up to 1 percent point higher compared to the processes without heat integration.

4.3.2 Comparison with syngas production by STL

Thermochemical processes for syngas production based on solar heat have been investigated extensively in the last years and are generally considered an important pathway towards CO_2 utilization alongside other emerging technologies [122]. Syngas is produced by simultaneously splitting H_2O and CO_2 [63, 12]. However, there are several drawbacks to this approach. First, very high temperatures (usually > 1273 K) and/or reduced pressure are needed for the thermal reduction of the oxygen storage material, resulting in high stability requirements for the reactor and the oxygen storage material [12]. Sintering is a problem that has been addressed extensively in the literature [12, 153]. Second, several research groups remarked that solid phase heat recovery between the oxidation and reduction reactions is a critical factor for the overall process efficiency [152, 33, 20, 55, 113]. While new reactor concepts are being developed [54] to address this problem, efficient solid phase heat recovery remains a major issue [12]. Third, the CO yield per solid mass is relatively low for STL processes. Reported values in the literature range from 0.15 mol_{CO}/kg_{CeO_2} for ceria [63] to 0.2-1.0 mol_{CO}/kg for state-of-the-art perovskite type materials [49, 52].

Syngas production by RWGSCL has several advantages over STL processes. By using H_2 for material reduction, temperatures can be lowered significantly. Although in this analysis a reactor temperature of 1073 K was assumed, operating temperatures as low as 823 K have been reported for RWGSCL [49]. Contrary to STL, reduced pressure is neither needed nor beneficial in RWGSCL since oxidation and reduction

are equimolar reactions with respect to the gaseous components. This potentially leads to lower equipment and operating costs. Furthermore, due to isothermal operation solid phase heat recuperation can be avoided. Oxidation and reduction can be carried out at equal temperature. Isothermal operation of STL has been proposed by Bader et al. for STL with ceria [20]. However, if isothermal operation is realized for STL, inert purge gas (e.g. nitrogen) must still be supplied to drive the oxygen release and an even lower pressure must be applied during reduction to obtain the same non-stoichiometry in ceria as would be obtained at higher temperature. Thus, isothermal operation could be realized in theory but it creates new problems for STL. Since both reactions in RWGSCL with iron oxide (eq. (4.2) and (4.3)) are endothermic, no heat is produced. Thus, there is no need for solid phase heat recuperation in the reactor. The desired reaction temperature is maintained during reduction and oxidation by external heating. Furthermore, hot spots which often occur in exothermic reactions and may damage the oxygen storage material can be avoided. The use of H_2 for material reduction increases the difference in attainable oxidation states compared to STL processes, which only use a small range in material non-stoichiometry (e.g. ceria-based) [12]. For iron oxide (Fe/Fe_3O_4), the thermodynamically possible CO yield per cycle is $17.2\,mol_{CO}/kg_{Fe_3O_4}$, which is nearly 30 times the amount that can be produced by using cerium oxide (see also Section 3.4.2). Assuming a cycle between CeO_2 and $CeO_{2-\delta}$ with a non-stoichiometry of $\delta = 0.1$, a maximum CO yield of $0.58\,mol_{CO}/kg_{CeO_2}$ is achievable per cycle. Daza *et al.* reported a CO yield of approximately $4\,mol_{CO}/kg$ of $La_{0.75}Sr_{0.25}CoO_{3-\delta}$ for the RWGSCL process [48]. A higher CO yield per cycle can potentially reduce the reactor size and minimize the equipment cost.

Theoretical overall efficiencies exceeding 20% have been reported for syngas production by STL by several research groups [152, 65, 55]. However, the system boundary in these studies often includes only the reactor and gas phase heating and cooling. The energy demand of important ancillary process steps (e.g. vacuum pumping, sweep gas production, gas separation) is often disregarded, leading to very optimistic process efficiencies. Studies that include these process steps deliver more realistic values for the efficiency. Bulfin *et al.* estimated the maximum efficiency of solar thermochemical production of syngas to be 7.5% without heat recovery and 11.5% for 60% solid phase heat recovery [33]. Bader *et al.* estimated realistic efficiencies to be 10% and 18% for solar thermochemical production of H_2 and CO, respectively [20]. For a reduction temperature of 1800 K, Falter *et al.* estimated a realistic efficiency of approximately 16% [56]. These results are still optimistic taking into account the practical problems associated with STL processes discussed above, which makes large scale implemen-

tation a rather distant reality. In contrast, efficiencies of up to 14.2% and 14.4% could be achieved by using the RWGS or the RWGSCL process, respectively, with state-of-the-art equipment.

4.4 Conclusions

This chapter served as a proof of concept for the RWGSCL process. Thermodynamic analysis was performed to compare RWGS and RWGSCL based on idealized process systems. The energy demand for product separation was estimated based on literature data of separation processes. The difference in process efficiency between RWGS and RWGSCL is most pronounced for syngas with a low H_2/CO ratio. The energy demand for H_2 production contributes most to the StS efficiency (η_{StS}). Without considering the energy demand of the electrolyzer, the energy consumption for the reactor/separator sequence can be reduced by up to 54% using the RWGSCL process as compared to the conventional RWGS process. Heat integration reduces the energy demand for process stream heating by up to 70%, depending on the desired syngas H_2/CO ratio. For pure CO production with heat integration, StS efficiencies of 12.7% and 13.7% can be achieved for RWGS and RWGSCL, respectively. The syngas H_2/CO ratio in RWGS is adjusted either by adjusting the H_2/CO_2 ratio in the reactor or by adding H_2 after the reaction. The preferred method depends strongly on the desired syngas H_2/CO ratio and if gas phase heat is integrated. The proposed process schemes for RWGS and RWGSCL offer reasonable alternatives for solar syngas production with efficiencies comparable to STL processes. RWGSCL is advantageous especially for the production of pure CO.

5 | Kinetic analysis

Truth is not what you want it to be; it is what it is, and you must bend to its power or live a lie.

Miyamoto Musashi

So far, only thermodynamic aspects have been taken into account in this thesis. The material selection framework (Chapter 3) and the efficiency analysis (Chapter 4) were both based on thermodynamic principles. However, thermodynamics only give a static view of the whole process. To fully understand and evaluate the RWGSCL process one needs to account for process kinetics as well because thermodynamic limits only show the theoretical boundaries of process operation. The real process occurs within these limits. Reaction equilibrium may never be reached and the OSM may deactivate over time. To include these and other dynamic phenomena kinetic aspects of the RWGSCL process have to be analyzed. Therefore, the aim of this chapter is to analyze and quantify the kinetic phenomena that govern the repeated oxidation and reduction of the OSM (modified iron oxide). The work of this chapter has been published previously in [175] and is reproduced with permission of Elsevier. Parts of the experimental analysis (Sections 5.1.3, 5.1.4, 5.2.2 and 5.2.3) were performed in collaboration with the Laboratory for Chemical Technology at Ghent University in Belgium. The parts of this publication [175] that were not written originally by the author of this thesis are included but indicated by quotation marks.

The reasons why modified iron oxide (80 wt% Fe_2O_3-$Ce_{0.5}Zr_{0.5}O_2$) is used in this thesis have been thoroughly discussed in Chapter 3. Even though the material is prepared in its fully oxidized state (Fe_2O_3) the oxidation and reduction reactions occur

only between Fe and Fe_3O_4 according to the following equations:

$$\text{Reduction:} \quad Fe_3O_4 + 4H_2 \rightleftharpoons 3Fe + 4H_2O \tag{5.1}$$

$$\text{Oxidation:} \quad 3Fe + 4CO_2 \rightleftharpoons Fe_3O_4 + 4CO \tag{5.2}$$

This is because the fully oxidized state (Fe_2O_3) is not achievable by is not achievable by oxidation with CO_2 at the considered reaction conditions. Oxygen would be required to further oxidize Fe_3O_4 to Fe_2O_3 [186]. On the other hand, pure iron can be obtained by reduction with H_2. Verification of this behavior is given by the experimental results presented in this chapter. For reasons of simplicity, the reactions of the support metal oxides ($Ce_{0.5}Zr_{0.5}O_2$) are not considered here because of the small amount of oxygen that is released and taken up by them compared to iron oxide. Since the OSM consists primarily of iron oxide which has a much higher oxygen storage capacity, this simplification is valid. The thermodynamically possible CO yield per cycle for the modified iron oxide is $13.8\,mol_{CO}/kg$ of Fe_3O_4-$Ce_{0.5}Zr_{0.5}O_2$ ($Ce_{0.5}Zr_{0.5}O_2$ is assumed to be inert) compared to $17.2\,mol_{CO}/kg$ for the Fe/Fe_3O_4 couple (see also Table 3.2). This value is still over 20 times higher than the theoretical value of non-stoichiometric ceria cycle.

In this chapter, the effect of repeated cycling on the crystallographic structure of the OSM is investigated via transmission electron microscopy (TEM) and x-ray diffraction (XRD). Long term experiments are conducted to analyze the deactivation behavior of the OSM and to obtain a material that is stabilized (i.e. that does not further deactivate upon cycling) under certain conditions. Further, the kinetics of the reduction and oxidation of the modified iron oxide material are analyzed by thermogravimetric analysis (TGA) as a basis for process design and analysis (see Chapter 6). A systematic methodology is applied to identify a kinetic model for the oxidation and reduction of the material, enabling the mathematical description of the process. Precise kinetic information available in the literature for various materials is still rather limited and often restricted to oxidation kinetics for thermochemical cycles [8, 119, 127, 131]. To the best of our knowledge, there are as of yet no kinetic expressions reported for modified iron oxide for the RWGSCL process.

5.1 Experimental

5.1.1 Material synthesis

The Fe_2O_3-$Ce_{0.5}Zr_{0.5}O_2$ samples were synthesized by urea hydrolysis using $Fe(NO_3)_3 \cdot 9H_2O$ (99.0%, Fluka), $Ce(NO_3)_3 \cdot 6H_2O$ (99.0%, Fluka) and $ZrO(NO_3)_3 \cdot 6H_2O$ (99.0%, Fluka). The mixed metal salt solution (0.1 M) was added to a 0.4 M solution of urea (99.0%, Fluka) to yield a salt to urea solution ratio of 2 : 1 (v/v). The precipitate solution was mixed at 100°C for 24 h. After the suspension was cooled to room temperature, the precipitate was separated from the solution. The solid product was washed with ethanol and dried overnight in an oven at 110°C. Then, the prepared Fe_2O_3-$Ce_{0.5}Zr_{0.5}O_2$ was calcinated at 800°C. To obtain particles of a defined size between 260 and 520 µm the finely powdered material was pelletized, crushed and sieved.

5.1.2 Material pretreatment and stabilization

The aim of the experiments was to obtain kinetic information about the reduction and oxidation cycles of modified iron oxide. It is well known that the activity of oxygen storage materials decreases over repeated redox cycles [153, 57]. The deactivation mainly occurs due to sintering of the particles and changes in their crystallographic structure. Thus, it can be expected that kinetic measurements with as-prepared material will not yield representative results. Therefore, the material sample was exposed first to repeated redox cycles to stabilize its structure before thermogravimetric experiments were conducted.

For material stabilization, a sample of 250 mg was fixed inside a quartz reactor with glass wool. The reactor was placed in an oven and heated to the reaction temperature (1073 K) under inert atmosphere. The gas composition was then repeatedly switched between a mole fraction of $x_i = 0.5$ of either H_2 (material reduction) or CO_2 (material oxidation) balanced with He as inert gas. The reaction time for reduction and oxidation was 5 min with 3 min of inert gas flushing (He) between the steps, which were repeated until 500 cycles were reached. During the pretreatment, the outlet gas composition was followed by mass spectrometry (Agilent 5973Network MSD) to obtain information about material activity over repeated redox cycles.

5.1.3 TEM

"A morphological and local elemental analysis was carried out in a microscope JEOL JEM-2200FS, Cs-corrected, operated at 200 kV and equipped with a Schottky-type field-emission gun (FEG) and EDX JEOL JED-2300D. Samples were prepared by immersion of a lacey carbon film on a copper support grid into the powder. Particles sticking to the carbon film were investigated. A beryllium sample retainer was used to eliminate secondary X-ray fluorescence in EDX spectra originating from the sample holder." [175]

5.1.4 Conventional and in-situ XRD

"The crystallographic changes in the sample were followed in a homebuilt Bruker-AXS D8 Discover apparatus (Cu Kα radiation of 0.154 nm). The reactor consisted of a stainless steel chamber with Kapton window to allow X-ray transmission. The sample was uniformly spread on a Si wafer and no interaction of sample with Si wafer was observed during the reaction. The diffraction data were recorded using a linear Vantec detector which allowed capturing diffracted X-rays in a 20° window with an angular resolution of 0.1°. The reactor chamber was evacuated to a base pressure of 4 Pa by a rotation pump before reaction. Gases were supplied to the reactor chamber from a rig with calibrated mass-flow meters. H_2 (x_{H_2} = 0.05 in He) was used as reducing gas, CO_2 (x_{CO_2} = 0.3 in He) for oxidation and pure He for purging the reactor. The in situ experiment was performed at a temperature of 1073 K. After heating to the reaction temperature in He, the sample was monitored with in situ XRD during isothermal cycling." [175]

5.1.5 Thermogravimetric analysis

The mass change of 100 mg of the stabilized sample was recorded under alternating gas composition in a thermogravimetric analyzer (Mettler Toledo TGA/SDTA 851e). The sample was placed in a cylindrical sample holder and a constant gas flow rate of 100 ml/min was applied in all experiments. Additionally, a constant flow of 20 ml/min of He was added to protect the precision balance from reactive gas. Therefore, the total gas flow rate was 120 ml/min. For the reduction and oxidization steps, H_2 and CO_2 were used in varying concentrations, respectively, balanced with He as inert gas.

The sample was heated to the desired temperature in the TG unit with a constant rate of 20 K/min under an inert atmosphere (He). Then, reactive gas was applied under isothermal conditions. At first, a reducing environment was established with H_2, ensuring that the sample was completely reduced to Fe. The next 45 min an oxidizing environment (CO_2) was applied to re-oxidize the sample to Fe_3O_4. This was followed by 45 min of reduction with H_2. At last, the sample was cooled to ambient conditions with a constant rate of 10 K/min.

The outlet gas composition was analyzed by mass spectrometry (Pfeiffer Vacuum GSD320) to assure that no other gaseous substances were produced.

Blank runs were conducted without sample before each experiment to account for buoyancy effects. The mass change without sample was subtracted from the experiment with sample. Thus, the recorded mass change is only attributable to the mass change of the sample. The same sample was used in all the experiments with various gas concentrations and temperatures.

Preliminary experiments showed that reaction rates become very slow at temperatures below 1023 K. Conversely, at temperatures exceeding 1123 K, the material's structure collapsed due to excessive sintering up to the point of surface melting (not shown) which led to severely decreased activity. Thus, the feasible temperature range for TG experiments was bounded between 1023 and 1123 K. Measurements were conducted at temperatures of 1023, 1073 and 1123 K and reactive gas mole fractions of 0.08, 0.25, 0.5 and 0.75. However, at T = 1023 K the experiment with a reactive gas mole fractions of 0.08 was not performed because the reaction rate was too slow. Therefore, 11 TG experiments were conducted in total.

5.2 Results and discussion

5.2.1 Material pretreatment

The CO production per cycle during the stabilization treatment is shown in Fig. 5.1. In the first cycle, ≈ 72% of the theoretically possible amount of CO was obtained. After the gradual deactivation of the material during the first 100 cycles, a steady CO yield was achieved for the next 400 cycles, resulting in a stable CO yield of approximately 1.0 mol/kg_{OSM} per redox cycle. Even though only a fraction of the theoretically possible value was achieved, the measured CO production per cycle in steady state

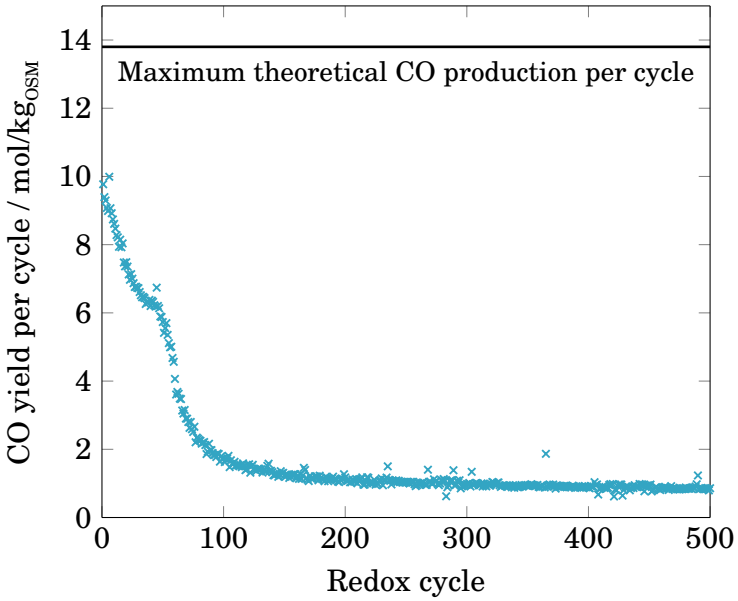

Fig. 5.1 CO yield per cycle for 500 redox cycles at 1073 K with a reactive gas mole fraction of 0.5 for CO_2 and H_2 in He, respectively. OSM refers to the oxidized material (Fe_3O_4-$Ce_{0.5}Zr_{0.5}O_2$). Reaction times for oxidation and reduction were 5 min each with 3 min inert gas (He) flushing between. The CO yield per cycle decreases gradually during the first 100 cycles, then reaches a steady state.

is comparable to the numbers reported by other research groups with more advanced materials (e.g. perovskites) at temperatures well above 1273 K [63, 52] (see also Chapter 3). The long time stability and the reaction kinetics of the OSM may be further improved by nanostructuring as recently demonstrated by Gao *et al.* [68]. with internal structural stability.

5.2.2 TEM

“The HR-TEM images of the as-prepared and 500 times cycled sample are displayed in Fig. 5.2 and Fig. 5.3. The TEM micrograph for the as-prepared material (Fig. 5.2a) shows the presence of particles (~ 35 – 50 nm) with similar morphology. The elemental composition of this material was identified by means of EDX mapping, showing the presence of Fe (red), Ce (green) and Zr (blue) (Fig. 5.2b). Zr is distributed throughout the sample (Fig. 5.2c), as is Fe (not shown), whereas strong clustering of Ce (Fig. 5.2d) is observed. Prolonged cycling of the sample results in increased particle sizes (Fig. 5.3) due to sintering. However, this phenomenon led to an evolution into two particles with different morphologies. In the first type (Fig. 5.3a), very large particles

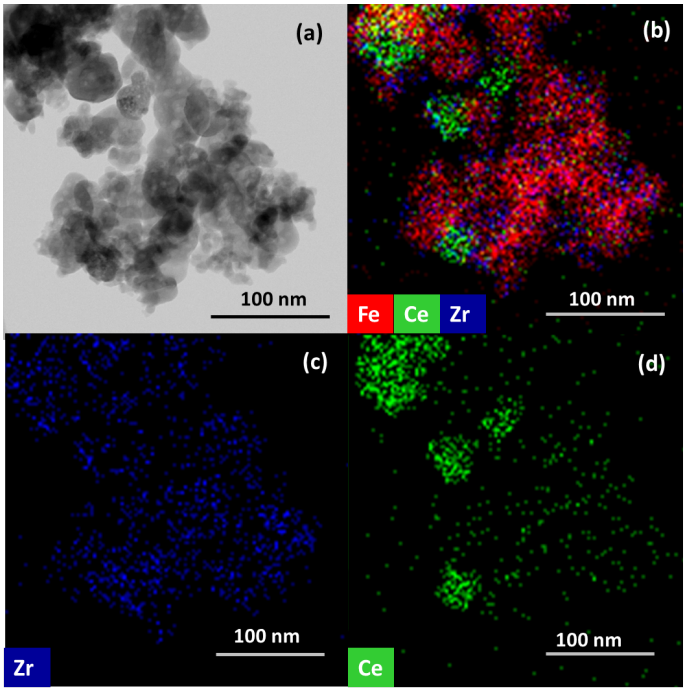

Fig. 5.2 HR-TEM image of as-prepared Fe_2O_3-$Ce_{0.5}Zr_{0.5}O_2$ showing (a) the sample morphology; (b) the EDX mapping of the constituent elements (Fe, Ce, Zr) along with the individual elemental maps of (c) Zr and (d) Ce. Figure taken from [175] with permission of Elsevier.

are observed (~ 200 – 600 nm), consisting of segregated Fe rich and Ce-Zr rich phases, based on the EDX overlay of images (Fig. 5.3b). Compared to the as-prepared sample (Fig. 5.2b), the distribution of Ce is more uniform in the Ce-Zr rich phase. In the second type of morphology (Fig. 5.3c) small particles (~ 100 nm) are incorporated inside relatively large particles (~ 300 nm). The EDX mapping (Fig. 5.3d) reveals Ce and Zr are both spread out throughout the large particles, while Fe is located in smaller particles inside the Ce-Zr phase." [175]

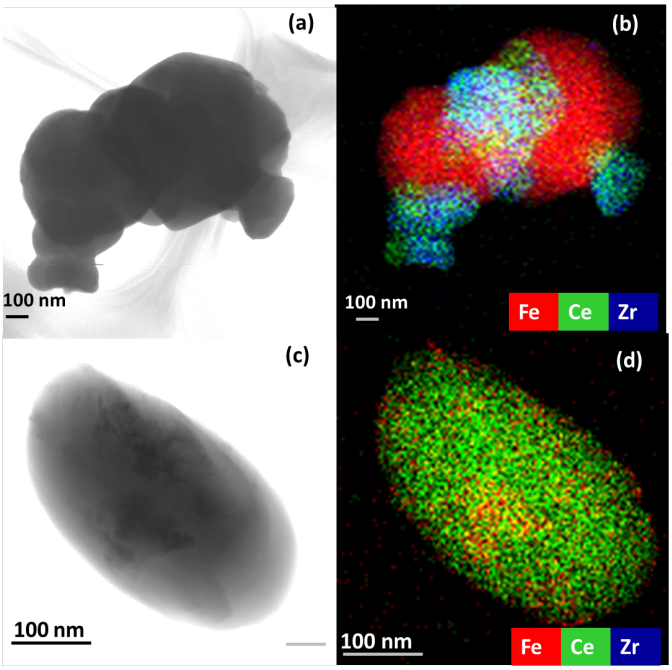

Fig. 5.3 TEM micrograph of a 500 times cycled sample with different morphologies. (a) Morphology with separated particles (b) EDX mapping of Fe, Ce, Zr. (c) Morphology with embedded structure, and (d) the EDX mapping showing the distribution of constituent elements. Figure taken from [175] with permission of Elsevier.

5.2.3 XRD analysis

"The crystalline phases in as-prepared and 500 times cycled Fe_2O_3-$Ce_{0.5}Zr_{0.5}O_2$ were identified using XRD (Fig. 5.4). The as-prepared materials (Fig. 5.4a) show diffraction peaks corresponding to Fe_2O_3 (33.15°, 35.61°, 40.85°, 49.48°, 54.09°, PDF: 00-033-0664), CeO_2 (28.55°, 33.08°, 47.47°, 56.33°, PDF: 00-033-0394) and $Ce_{0.5}Zr_{0.5}O_2$ (29.10°, 33.70°, 48.50°, 57.50°, PDF: 00-038-1439) phases. The diffraction pattern of Fe_2O_3 is clearly identified, whereas CeO_2 and $Ce_{0.5}Zr_{0.5}O_2$ show a close overlap of peak

positions. However, the presence of separate CeO_2 and $Ce_{0.5}Zr_{0.5}O_2$ phases can be discerned from the diffraction peaks at higher angles (~ 48° and ~ 57°) where they are relatively well resolved in comparison to lower angles (~ 29° and ~ 33°). The lattice parameter calculated from the overall peak at ~ 29° yielded a value of 0.5361 nm, which is intermediate to $Ce_{0.5}Zr_{0.5}O_2$ (0.5301 nm) and pure CeO_2 (0.5410 nm). Based on the resolved diffractions at higher angle, it is likely that this low angle diffraction equally contains contributions from CeO_2 and $Ce_{0.5}Zr_{0.5}O_2$. The TEM images reveal homogeneous distribution of Zr with strong clustering of Ce (Fig. 5.2c and Fig. 5.2d). The results from TEM and XRD hence imply the existence of Ce in solid solution between Ce and Zr, present throughout the sample, and in separate dispersed CeO_2 clusters, next to the Fe_2O_3 phase. On the other hand, no separate diffraction peaks of ZrO_2 were identified. Similarly, in the 500 times cycled sample (Fig. 5.4b), phases of Fe_3O_4 (30.10°, 35.45°, 47.17°, 43.09°, 53.45°, 56.98°, PDF: 03-065-3107) along with $Ce_{0.5}Zr_{0.5}O_2$ are identified. Unlike the as-prepared sample no diffraction peaks pertaining to Fe_2O_3 and CeO_2 are present. Reoxidation of reduced material with CO_2 results in the formation of Fe_3O_4, instead of Fe_2O_3, which can only be obtained by using oxygen/air as re-oxidizing agent [186]. No peaks or shoulders typical for pure CeO_2 are noticed. Further, the lattice parameter calculation for the peak at ~ 29° exhibits a value of 0.5312 nm indicating a solid solution between Ce and Zr. Hence the XRD patterns represent a mixed Ce-Zr phase in line with the TEM images (Fig. 5.3) where Ce and Zr are more evenly distributed in comparison to the as-prepared sample." [175]

In situ XRD for one complete redox cycle is depicted in Fig. 5.5. At the start of the experiment, only Fe_3O_4 is detected in He atmosphere. At 2.5 min, the gas mole fraction of H_2 was switched to 0.05 H_2 in He, resulting in a reducing environment, in which Fe_3O_4 was first converted into FeO and then into Fe. At t = 17.5 min an oxidizing environment was established with x_{CO_2} = 0.3 in He. Again, FeO is formed in an intermediate step, which reacts further to Fe_3O_4. The results indicate that under the investigated conditions full conversion for reduction and oxidation is achieved according to equations (5.1) and (5.2).

5.2.4 Thermogravimetric analysis

In Fig. 5.6, TG data of the stabilized OSM is shown together with the MS signal of the outlet gas composition during oxidation and reduction at 1073 K with reactive gas mole fractions of 0.75 for both CO_2 and H_2. The production of CO during oxidation and

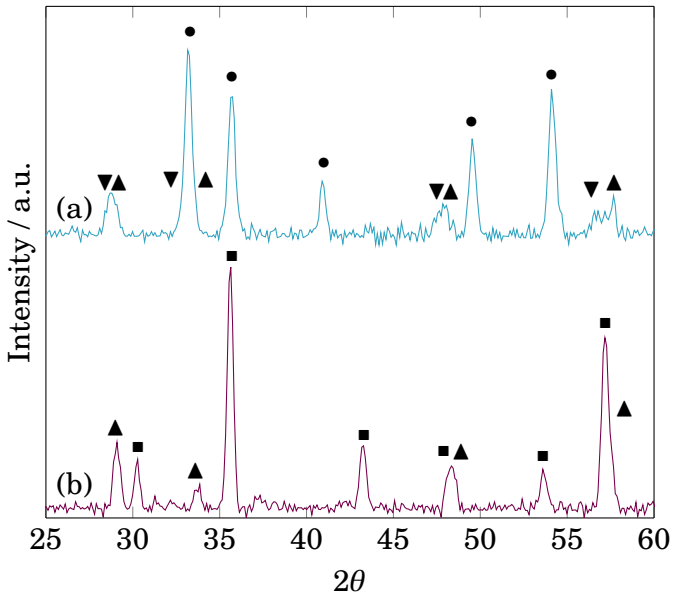

Fig. 5.4 XRD patterns of (a) as-prepared and (b) 500 times cycled Fe_2O_3-$Ce_{0.5}Zr_{0.5}O_2$. (•) Fe_2O_3, (▪) Fe_3O_4, (▲) $Ce_{0.5}Zr_{0.5}O_2$ and (▼) CeO_2.

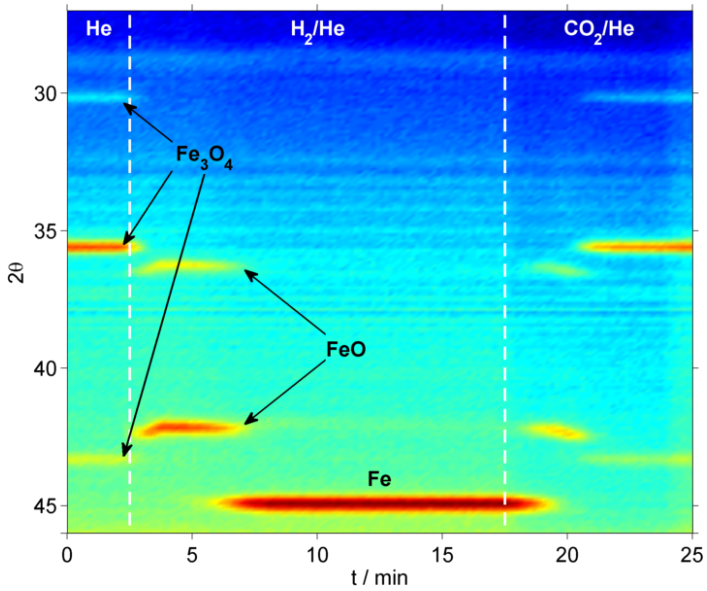

Fig. 5.5 In situ XRD for one full redox cycle at 1073 K and a total gas flow of 1 l/min. Fe_3O_4 is reduced to Fe with H_2 and re-oxidized to its initial state with CO_2. In both transitions, the presence of FeO is detected, which is formed in an intermediate step. Both reduction and oxidation yield to full conversion, as described in equations (5.1) and (5.2). Figure taken from [175] with permission of Elsevier.

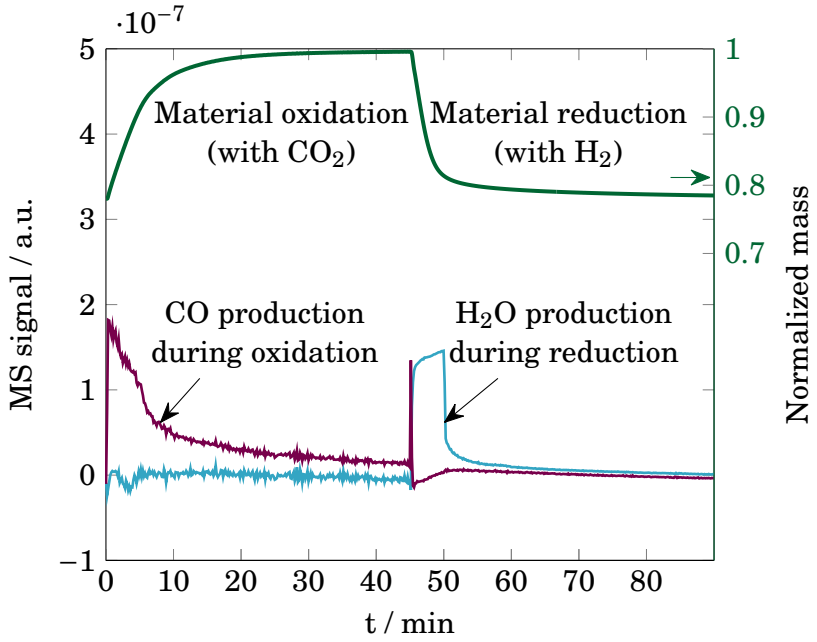

Fig. 5.6 Thermogravimetry results for stabilized OSM (green, right axis) at 1073 K and a reactive gas mole fraction of 0.75 for CO_2 (oxidation) and H_2 (reduction) balanced with He together with mass spectrometry signal of the corresponding outlet gas (left axis). The MS signal was corrected by subtracting the measured signal from the blank run without OSM in the TG unit. The red and blue lines indicate the MS signal for CO and H_2O, respectively.

water formation during reduction of the material was observed according to equations (5.2) and (5.1). No other substances were detected apart from the reactants. The rate of CO production is directly coupled with the material oxidation according to equation (5.2). Initially, CO yield is high and then gradually decreases until the material is fully oxidized.

The mass change of the stabilized OSM under different conditions is shown in Fig. 5.7 for oxidation (left) and reduction (right). The measured mass of the sample was normalized to the mass of the sample in its oxidized state (a value of 1.00 was assigned for Fe_3O_4-$Ce_{0.5}Zr_{0.5}O_2$). In the experiments, a normalized mass of approximately 0.78 was measured initially, which is very close the theoretical normalized value of 0.779 for the reduced state Fe-$Ce_{0.5}Zr_{0.5}O_2$ (assuming $Ce_{0.5}Zr_{0.5}O_2$ is not reduced). This indicates that the mass change upon reduction is likely due to the reduction of iron oxide only and $Ce_{0.5}Zr_{0.5}O_2$ is not reduced. If it is assumed that $Ce_{0.5}Zr_{0.5}O_2$ is reduced to $Ce_{0.5}Zr_{0.5}O$, slightly lower values of 0.765 could be obtained theoretically. Upon oxidation, values of approximately 1.00 are reached (in some experiments, the reaction rates for oxidation were too slow to reach the final oxidation state). Overall, the reaction rates of oxidation and reduction increase as a function of temperature and concentration of reactive gas, while the rate of reduction is higher than that of oxidation. Even at low gas concentration of $x_{H_2} = 0.08$, the reduction at 1073 K leads to complete conversion within 25 min, while during oxidation the material is still not fully oxidized after 45 min.

Even though the material showed deactivation during 500 redox cycles in the stabilization pretreatment (see Fig. 5.1), the mass change of the material in the subsequent TG experiments indicates that the material is cycled between Fe and Fe_3O_4 according to equations (5.1) and (5.2). The observed deactivation during the pretreatment obviously did not influence the attainable oxidation states of the material in TG experiments. The observed decline of CO yield during the material pretreatment (see Fig. 5.1) is likely explained by reduced rate of reactions due to sintering. During oxidation and/or reduction the material is not completely converted within the limited reaction time in the plug flow reactor.

5.2.5 Master plot analysis

The rate equations for various reaction mechanisms were compared to the experimental TG data by master plot analysis [72]. This graphical method allows to deduce

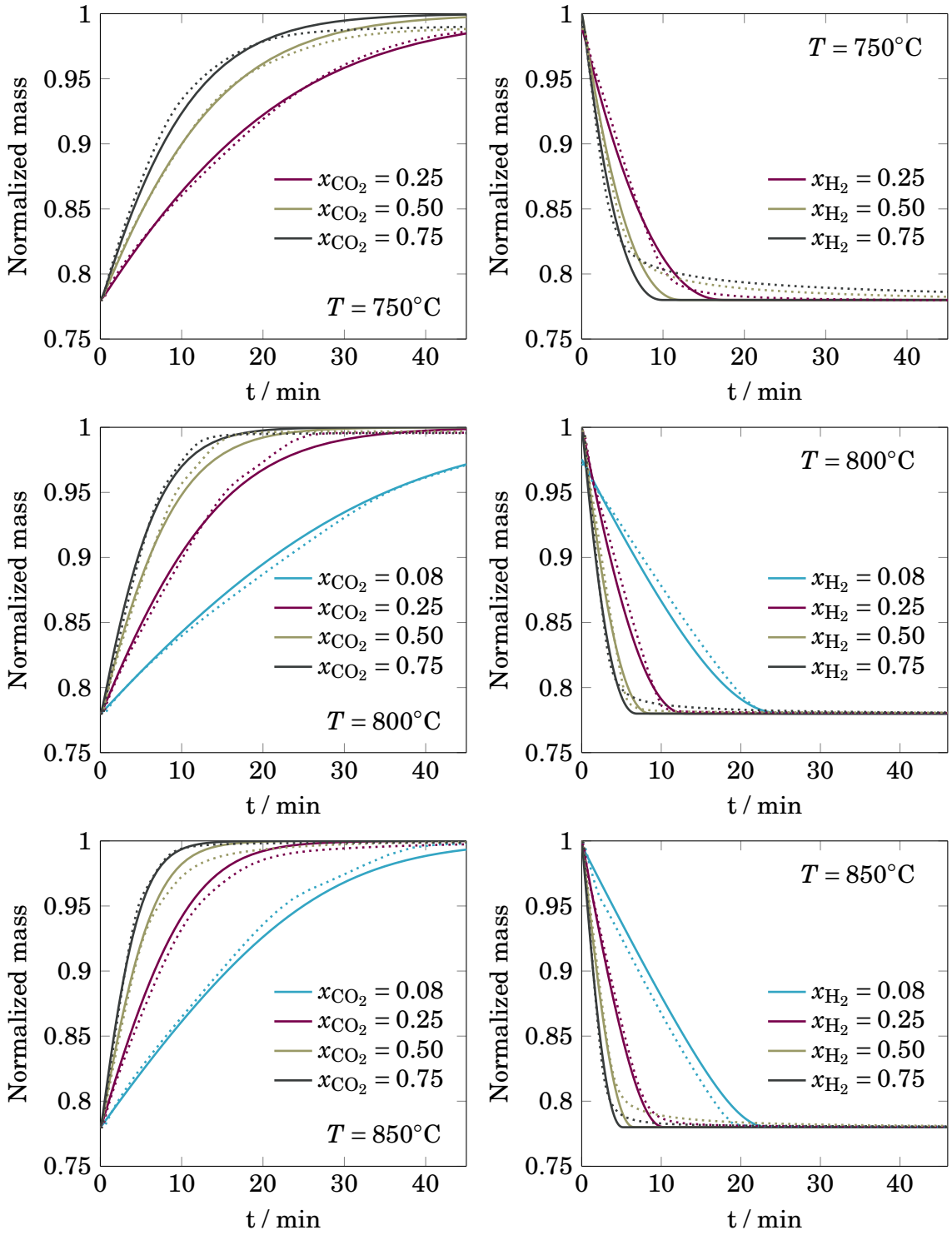

Fig. 5.7 Thermogravimetry results for stabilized OSM (dotted lines) and simulated model (solid lines) for oxidation (left, R2 model) and reduction (right, R2 model) at 1023, 1073 and 1123 K. Different colors indicate the corresponding mole fractions of CO_2 and H_2 (balanced with He), respectively. The mass is normalized with the mass of the oxidized sample (Fe_3O_4-$Ce_{0.5}Zr_{0.5}O_2$).

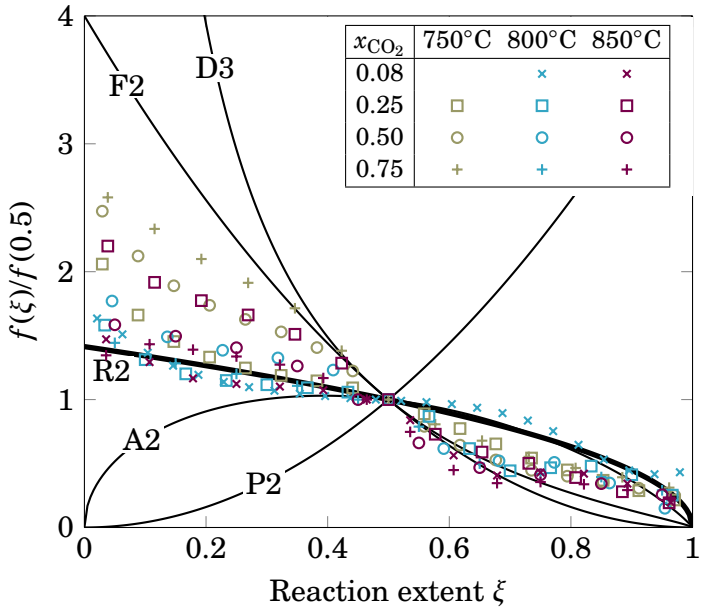

(a) Oxidation

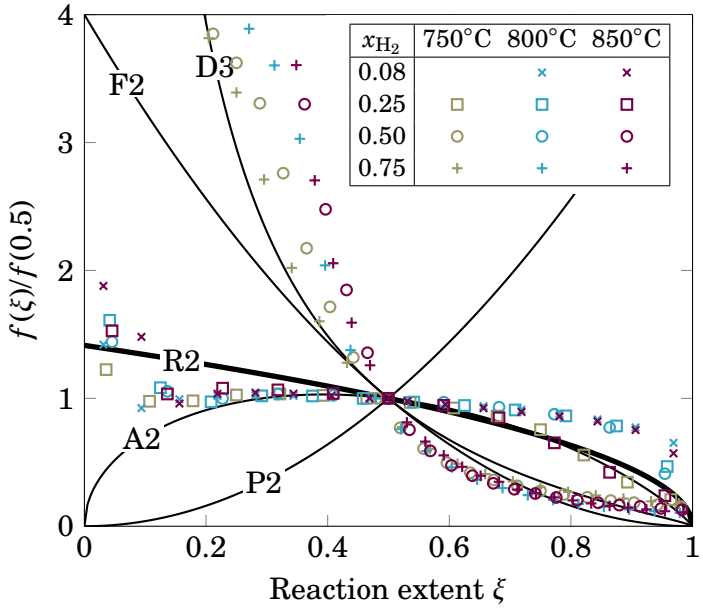

(b) Reduction

Fig. 5.8 Master plot results for oxidation (top) and reduction (bottom). Experimental results shown as markers, theoretical models as lines with their respective abbreviations (see Table 5.1). Thick lines indicate the chosen models for oxidation and reduction, respectively.

and compare kinetic models with the experimental data without prior identification of the kinetic parameters of the rate equations. Thus, a qualitative indication about the reaction mechanism is obtained and possible erroneous conclusions due to weakly identified parameters can be avoided. Finally, the parameter estimation can be done only for the most probable model instead of for numerous models.

To apply the method, the generalized solid-state kinetic rate expression

$$\frac{\mathrm{d}\xi}{\mathrm{d}t} = k^0 \exp\left(-\frac{E_A}{RT}\right) f(\xi) f(x_i) \tag{5.3}$$

is used, where ξ is the reaction extent at time t, $f(\xi)$ a function depending on the reaction mechanism, $f(x_i)$ a function of the reactive gas mole fraction x_i, E_A the activation energy, k^0 the pre-exponential factor of Arrhenius, and T the absolute temperature. By introducing the generalized time, Θ (reaction time to attain a certain ξ at any temperature), defined as

$$\Theta = \int_0^t \exp\left(-\frac{E_A}{RT}\right) \mathrm{d}t \tag{5.4}$$

the kinetic rate expression at any temperature can be derived by differentiation of eq. (5.4)

$$\frac{\mathrm{d}\Theta}{\mathrm{d}t} = \exp\left(-\frac{E_A}{RT}\right) \tag{5.5}$$

The combination of eq. (5.3) and (5.5) yields

$$\frac{\mathrm{d}\xi}{\mathrm{d}\Theta} = k^0 f(\xi) f(x_i) \tag{5.6}$$

Using a reference point at $\xi = 0.5$, the following equation is derived from eq. (5.6)

$$\frac{\mathrm{d}\xi/\mathrm{d}\Theta}{(\mathrm{d}\xi/\mathrm{d}\Theta)_{\xi=0.5}} = \frac{f(\xi)}{f(0.5)} \tag{5.7}$$

Being only dependent on ξ, eq. (5.7) compares the experimental data (left-hand side) with the suggested model (right-hand side). Both sides are equal when the chosen model exactly describes all experimental data points. Thus, by plotting the experimental data against various theoretical models according to eq. (5.7), one ob-

tains a graphical way to choose a suitable model without determination of the kinetic parameters.

A list of the common kinetic functions for gas-solid reactions is given in Table 5.1. The gas-solid reaction kinetics considered here are categorized in the geometrical contraction (Rn), the reaction order (Fn), the nucleation (Pn and An) and the diffusion groups (Dn), where n is the reaction order. For geometrical contraction models (Rn), a rapid nucleation is assumed and the rate is dependent on the progress of the reaction interface towards to the crystal center. Reaction order models (Fn) are based on homogeneous mechanistic assumptions. Power law models (Pn) are applicable for reactions where the formation and growth of nuclei are rate limiting. Avrami-Erofeev models (An) include further restrictions on nuclei growth like coalescence and ingestion. Thus, they yield s-shaped curves which account for a restricted rate of reaction in the final stage. Diffusion models (Dn) are used to describe reactions where the rate is controlled by the limited diffusion of reactants or products to or from the reaction interface. Khawam *et al.* provided a detailed discussion about the theoretical foundations of solid-state reaction kinetics [101].

Table 5.1 Used gas-solid kinetic equations for master-plot analysis, adapted from Heidebrecht *et al.* [82].

Name	$f(\xi)$
Contracting Cylinder (R2)	$(1-\xi)^{1/2}$
Contracting Sphere (R3)	$(1-\xi)^{2/3}$
Reaction Order (Fn)	$(1-\xi)^{n}$
Power Law (Pn)	ξ^{n}
Avrami-Erofeev (A2)	$(1-\xi)[-\log(1-\xi)]^{1/2}$
Avrami-Erofeev (A3)	$(1-\xi)[-\log(1-\xi)]^{2/3}$
Avrami-Erofeev (A4)	$(1-\xi)[-\log(1-\xi)]^{3/4}$
1D Diffusion (D1)	$(1-\xi)^{0}\left[1-(1-\xi)^{1}\right]^{-1}$
2D Diffusion (D2)	$(1-\xi)^{1/2}\left[1-(1-\xi)^{1/2}\right]^{-1}$
3D Diffusion (D3)	$(1-\xi)^{2/3}\left[1-(1-\xi)^{1/3}\right]^{-1}$

Fig. 5.8 shows the master plots for the experimental data (eq. (5.7), l.h.s.) together with theoretical models (eq. (5.7), r.h.s.) from Table 5.1 for oxidation (5.8a) and reduction (5.8b). For clarity, not all theoretical models were plotted but only representative ones from each model category. While all points coincide at the reference point of $\xi = 0.5$, they disperse clearly in the range of $\xi < 0.5$, allowing for model discrimination.

For oxidation (5.8a), most of the experimental points are located between the geometrical contraction model (R2) and the reaction order model (F2). We chose the R2 model as the most appropriate kinetic model to describe the material oxidation. However, by comparing the R and F models, one observes that they are mathematically very similar and only differ in their respective exponents. Thus, the exponent n_O is estimated in Section 5.2.6 to allow for more flexibility and to minimize the deviation between model simulation and experimental data.

For the reduction stage, a different behavior was observed for experiments with $x_{H_2} = 0.75$ and for experiments with gas mole fraction of $x_{H_2} = 0.5$ at temperatures of 1023 and 1123 K. The data of these experiments correlate better with a diffusion limited reaction model (D3). This behavior was observed only for reduction. However, similarly to oxidation most experimental observations for reduction are well described by the R2 model. The exponent n_R of the R2 model for the reduction was estimated together with all other parameters as discussed in the following.

5.2.6 Parameter estimation

Master plot analysis showed that kinetic models of the geometrical contraction group (the R2 model in particular) are most appropriate to describe the kinetic behavior of material oxidation and reduction. Since the observed mass change in TG experiments indicated that $Ce_{0.5}Zr_{0.5}O_2$ is not participating in the redox reactions, a mathematical model was derived based only on the oxidation and reduction of iron oxide (see equations (5.2) and (5.1), respectively). The intermediate step through FeO was not explicitly modeled as the reactions from Fe to FeO and from FeO to Fe_3O_4 (and *vice versa*) seem to proceed at a very similar rate. Therefore, the TG data the did not allow for a clear discrimination between the reaction steps. The proposed model is derived following an engineering approach and provides a trade-off between simplicity and accuracy. Using the R2 model, the reaction rates for oxidation and reduction are described by equations (5.8) and (5.9), respectively.

$$r_{\mathrm{Ox}} = k^0_{\mathrm{Ox}} \exp\left(-\frac{E_{A,\mathrm{Ox}}}{RT}\right)\left(1 - x_{\mathrm{FeO_{4/3}}}\right)^{n_{\mathrm{Ox}}} x_{\mathrm{CO_2}}^{m_{\mathrm{Ox}}} \tag{5.8}$$

$$r_{\mathrm{Red}} = k^0_{\mathrm{Red}} \exp\left(-\frac{E_{A,\mathrm{Red}}}{RT}\right)(1 - x_{\mathrm{Fe}})^{n_{\mathrm{Red}}} x_{\mathrm{H_2}}^{m_{\mathrm{Red}}} \tag{5.9}$$

Here, k^0, E_A, n and m are adjustable parameters for oxidation (index Ox) and reduction (index Red), adding up to a total of eight parameters. For modeling details, see appendix A.2. Parameter estimation was performed with the statistics toolbox in MATLAB. The nonlinear least-squares regression function *nlinfit* was used for parameter estimation. The confidence intervals were calculated with the function *nlparci* and the coefficient of determination R^2 was determined by the following equation

$$R^2 = 1 - \frac{\sum_i (o_i - f_i)^2}{\sum_i (o_i - \bar{y}_i)^2}, \tag{5.10}$$

where o_i are the experimental observations and f_i are the predicted values from the model at each point i, respectively. The mean of the experimental points is denoted by $\bar{o}_i$.

The estimates for all kinetic parameters are given in Table 5.2. In Fig. 5.7, the

Table 5.2 Estimated kinetic parameters and 95% confidence intervals for oxidation and reduction reaction described by equations (5.8) and (5.9), respectively. Parameters valid from 1023 to 1123 K with reactive gas mole fractions x_{H_2,CO_2} from 0.08 to 0.75. OSM refers to the material in its oxidized state Fe_3O_4-$Ce_{0.5}Zr_{0.5}O_2$.

Estimated parameter	Oxidation	Reduction
n	1.002 ± 0.004	0.724 ± 0.008
m	0.618 ± 0.002	0.461 ± 0.004
k^0 / mol/kg$_{OSM}$/s	18199 ± 827	1140 ± 125
E_A / kJ/mol	111.6 ± 0.4	80.7 ± 0.9
R^2	0.9930	0.9827

gravimetric data (dotted line) are shown together with the model prediction (solid line) for the different experimental conditions. For oxidation, the model simulates the data very well, which is reflected in a high R^2 value of 0.9930. For the reduction, slight deviations of the model prediction from the experimental data are observed for the experiments with gas mole fractions of $x_{H_2} \geq 0.5$, as discussed in Section 5.2.5. The deviations are more pronounced in the later stages of the reduction (see Fig. 5.7). Here, the model predicts a slightly higher reaction rate than observed in the experiments. However, a value of $R^2 = 0.9827$ for the reduction indicates an acceptable agreement between model and experimental data.

The estimated value of $n_{Ox} = 1.002$ confirms the previous conclusion from master plot analysis, that the reaction order for the oxidation lies between the Rn and Fn

group. However, the value indicates that the F1 model is most appropriate for the description of material oxidation. For reduction, the estimated value of $n_{\mathrm{Red}} = 0.724$ corresponds closely to the R3 model. The narrow confidence intervals for oxidation and reduction confirm a good correlation of the experimental data with the proposed models. The slightly larger confidence interval for k^0_{Red} ($\pm 11.01\,\%$) indicates that part of the experimental data for material reduction is weakly described by the model.

The reaction orders (m_i) for the gas concentrations are lower than one, indicating that the reaction rates increase only moderately for increasing reactive gas mole fractions. This is also observed experimentally. In Fig. 5.7, the increase of the reaction rates from reactive gas mole fractions of 0.25 to 0.5 is larger than that from 0.5 to 0.75 at all temperatures. This phenomenon is more pronounced in material reduction.

5.3 Conclusions

The redox behavior of modified iron oxide (80 wt% Fe_2O_3-$Ce_{0.5}Zr_{0.5}O_2$) was investigated for the RWGSCL process. The material was stabilized for 500 redox cycles. Deactivation takes place during the first 100 cycles. For the remaining 400 cycles, a steady CO yield per cycle was achieved. Repeated cycling led to increased crystallite sizes due to sintering and a phase segregation into Fe rich and Ce-Zr rich phases in the sample. Surface sintering is likely to be the main cause for material deactivation as it leads to slower reaction kinetics and a lower CO yield within a fixed time. The stabilization pretreatment using repeated cycling did not influence the attainable oxidation states of the material as was evidenced by the observed mass change in TG experiments, which closely matched the theoretically possible mass change according to equations (5.1) and (5.2). The kinetics for material oxidation with CO_2 and reduction with H_2 were studied by means of TG experiments. The reaction rates of reduction are always faster than those for oxidation under equivalent conditions. Low reaction rates ($T \leq 1023\,\mathrm{K}$) and material instability ($T > 1123\,\mathrm{K}$) limited the temperature range for TG experiments. CO was generated during material oxidation and no other substances were detected. The experimental data were modeled and kinetic parameters were estimated. Oxidation and reduction were best described by a reaction order model and a geometrical contraction model, respectively. The model presented here can be used for further analysis and design of the process as well as for comparison of RWGSCL to other chemical looping processes.

6 | Process design and optimization

The usefulness of a model is not what it can explain, but what it can't. If you are equally good at explaining any outcome, you have zero knowledge.

Eliezer Yudkowski

While the RWGSCL process was shown to be feasible in theory in Chapter 3, various experimental results were presented in Chapter 4 that confirmed the feasibility of the concept on a laboratory scale. Given these promising results, upscaling of the process is the next logical step. In addition to the thermodynamic data that was used to analyze the OSM and the RWGSCL process in Chapters 2 and 3, valuable kinetic information for modified iron oxide was obtained in Chapter 5 that can now be used for detailed process modeling. Given the data and the computing power that is available today, process simulation is gradually becoming more important as the first step towards upscaling since building a large scale plant is always expensive and time consuming. Extensive preliminary analysis based on process simulation is necessary to ensure that the best possible reactor or system configuration is chosen before attempting to build an actual plant. This is especially true for complex process like RGWSCL. While RWGSCL is easy in principle, building a large scale reactor entails numerous problems depending on the reactor type chosen (e.g. material handling, valve switching, heating/cooling). From an industrial perspective the biggest caveat of the RWGSCL process (or any chemical looping process) is arguably that it is inherently dynamic, i.e. conventional steady-state operation is not possible. Historically, steady-state operation is industrially preferred because it is generally easier to maintain and it usually yields a specific and stable product stream.

The aim of this chapter is to answer the question of how to ensure a steady and stable product stream (carbon monoxide) in the RWGSCL process. To achieve this

goal process simulation and optimization are used based on the kinetic data obtained in Chapter 5. The work presented in this chapter has been published previously in [177] and is reproduced with permission of Elsevier.

Due to the cyclic switching between two process steps, RWGSCL is more complex than the traditional RWGS process and a conventional steady-state operation is not possible. However, a cyclic steady-state (CSS) can be achieved after prolonged switching. The simplest design that allows a steady (i.e. quasi-continuous) production of CO via RWGSCL is comprised of two reactors as illustrated in Fig. 6.1. By switching the gas flows between at least two reactors after the OSM is reduced or oxidized, respectively, a quasi-continuous process can be established. Even though Fig. 6.1 implies a

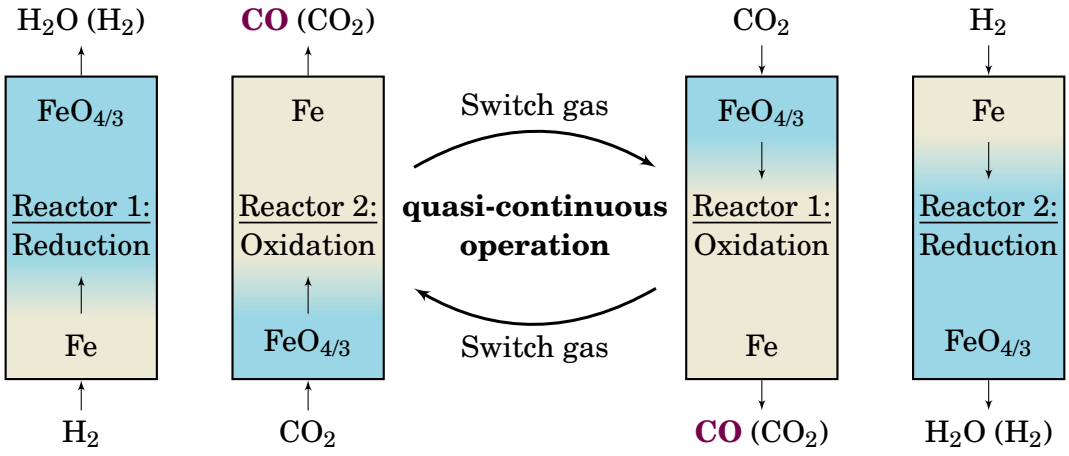

Fig. 6.1 Illustration of the RWGSCL concept with two fixed bed reactors which are operated simultaneously. After the OSM is exhausted (i.e. reduced or oxidized), the gas inlet composition is switched and the gas flow direction is reversed. Repeated switching yields a quasi-continuous process for CO production. Colors indicate different oxidation states of the OSM: blue=completely oxidized ($FeO_{4/3}$), beige=completely reduced (Fe).

fixed bed reactor design for both reactors, any reactor design can be used in principle. The main question for upscaling of the RWGSCL process is which reactor type to use.

Many advanced reactor designs have been proposed in the literature for chemical looping processes to deal with the operational difficulties arising from their cyclic nature and to increase their process efficiency. Cho *et al.* used a continuously operating moving bed chemical looping design with three reactors for the production of hydrogen and electricity [42]. Wei *et al.* investigated a 10 kW_{th} chemical looping gasification plant for biomass based on an interconnected fluidized bed reactor design [173]. For STL, Ermanoski *et al.* demonstrated a reactor with a continuously moving bed of

particles [54]. Another novel STL reactor design was proposed by Tou et al. which is based on a ceria membrane [167]. Continuous production of CO from CO_2 was demonstrated. Welte *et al.* showed a $2\,kW_{th}$ aerosol reactor using a downward gravity-driven aerosol flow [174]. For chemical looping combustion (CLC) rotating reactors have been proposed by Håkonsen and Blom [76]. While these reactor designs show promising results and avoid some of the challenges associated with conventional reactor designs (e.g. material sintering[184, 144, 171], heat recovery problems), most of them are still far from an industrial scale and face other challenges (e.g. material attrition, controllablity issues, complicated design). Often, conventional reactor designs such as fixed beds and fluidized beds are industrially preferred because of their relative simplicity and well known behavior. Of all chemical looping processes, CLC is arguably the most advanced technology in terms of scale of operation with several larger-scale plants ($50-150\,kW_{th}$) being mentioned in the literature [141, 28, 7, 134, 140, 115]. They are all based on interconnected fluidized bed reactor designs that operate continuously, which is the most common realization of CLC systems [11]. Zhou *et al.* noted that the main problem with fluidized bed reactors is attrition and that it may be avoided by using a fixed bed reactor design [185]. However, in simulation studies they found that the temperature gradients in the fixed bed can become problematic and, therefore, they argued for using fluidized bed reactors for large-scale implementation of CLC. In RWGSCL, temperature gradients are expected to be a minor problem because the involved reactions are only mildly endothermic. Furthermore, a better temperature control can be achieved by using multi-tube reactor designs instead of single-tube reactors. The advantages and disadvantages of fixed bed vs. fluidized bed reactors must be evaluated in detail for RWGSCL since not all results from CLC can be safely adopted.

Therefore, a fixed bed and a fluidized bed reactor design for the RWGSCL process for continuous production of syngas are analyzed here to show the possibilities and limitations of using simple, well known reactor designs. The goal is to investigate from a theoretical point of view whether fixed or fluidized bed reactors yield better performance for the RWGSCL process. With these insights informed decisions can be made on which reactor type warrants further investigation.

Zhang et al. [184] and Zhou et al. [185] compared fixed bed and fluidized bed reactor designs for CLC systems. Zhang et al. performed performed lab-scale experiments and concluded that the fixed bed reactor yields higher carbon conversion for CLC of coal with iron oxide (unmodified) as oxygen storage material. However, they also noted that a fluidized bed reactor type may prove advantageous for long term

operation since it effectively avoids sintering and agglomeration [184]. Zhou et al. performed simulation studies for CLC of methane on nickel oxide as oxygen storage material. They state that the fluidized bed reactor is “more appropriate for large-scale implementation of the CLC process because of its uniform temperature and pressure distribution, high CO_2 selectivity (> 95%), negligible carbon formation (< 2mol% C basis), and high fuel conversion (> 90%) over longer reduction periods”. [185]. While both studies are concerned with CLC the results and recommendations for reactor selection vary significantly due to several factors (different OSM, theoretical vs. experimental approach). It is therefore concluded that the selection of a specific reactor design for RWGSCL must be based on a detailed analysis.

In this chapter, the number of reactors studied is limited to two (compared to designs with a larger number of reactors operating simultaneously) which are switched repeatedly to minimize the investment costs and to simplify process operation (see Fig. 6.1). Previously, a conceptual study was conducted by Heidebrecht *et al.* [83] for the cyclic water-gas shift process, which is similar to RWGSCL. However, the reaction equilibria, which are crucial for the process were neither considered in that work [83] nor in an optimization study on the same process conducted by Logist *et al.* [117]. In a follow-up work by Heidebrecht and Sundmacher [81], a thermodynamic approach was used for the same process to consider the effects of equilibrium limitations. However, the process kinetics were not considered. In all of the previous studies only fixed bed reactor designs were studied. Thus, a detailed analysis considering the interplay between the reaction kinetics and thermodynamic limitations is still missing for the fixed bed reactor as well as for the fluidized bed reactor. The author is not aware of comparable studies for the RWGSCL being published yet. Process simulation is used to analyze the dynamic behavior of the RWGSCL process for a fixed bed and a fluidized bed reactor configuration. Optimization problems are formulated to maximize the average CO concentration and the OSM utilization. The mutual dependency of the optimization objectives is investigated and the results are discussed within the scope of process design.

6.1 Process modeling

A fixed bed and a fluidized bed reactor model are developed in the following to investigate their operational behavior for the RWGSCL process. In both cases 1D models were chosen as a trade-off between model accuracy and complexity since the trans-

port phenomena in radial direction are expected to be negligible compared to the axial transport.

6.1.1 Fixed bed

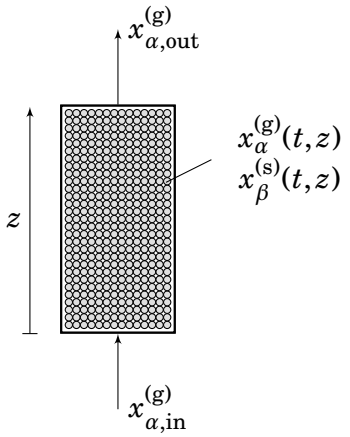

Fig. 6.2 Illustration of a heterogeneous 1D plug flow reactor filled with solid oxygen storage material (OSM).

The RWGSCL reactor is modeled as a 1D fixed bed reactor filled with solid oxygen storage material (OSM) as depicted in Fig. 6.2. The reactor inlet composition is repeatedly switched between pure CO_2 (oxidation stage) and H_2 (reduction stage), resulting in a cyclic process. Due to the two stages, two different operation modes are possible: co-flow and reverse-flow. Heidebrecht *et al.* showed that application of flow reversal is advantageous [83]. Therefore, reverse-flow operation is used for the fixed bed reactor design, i.e. the gas flows in opposite direction during the reduction and oxidation stage. Isothermal operation is assumed since all reactions have only moderate reaction enthalpies. Sufficient heating and cooling for isothermal operation can be ensured by using multi-tube reactor designs to enlarge the heat transfer area. Thus, the mass balance equations are sufficient to model the reactor. The change of the mole fraction of a gas component α in the gas phase, $x^{(g)}_{\alpha}$, is described by

$$\frac{\partial x^{(g)}_{\alpha}}{\partial t} = -\frac{v^{(g)}}{\varepsilon}\frac{\partial x^{(g)}_{\alpha}}{\partial z} + \frac{(1-\varepsilon)\rho^{(s)}}{\varepsilon c^{(g)}_{t}}\sum_{j}^{N_R}\nu_{\alpha,j}r_j \qquad \forall\alpha = \{H_2, H_2O, CO, CO_2\}, \tag{6.1}$$

where $v^{(g)}$ is the superficial gas phase velocity, ε the fixed bed void fraction, $\rho^{(s)}$ the density of the solid OSM and $c_t^{(g)}$ the total gas concentration. Chemical reactions are considered by the last term on the right hand side of equation (6.1), where $[r_j] =$ mol/(kg$^{(s)}$s). The mole fraction of a solid component β in the solid phase is described by

$$\frac{\partial x_\beta^{(s)}}{\partial t} = M^{(s)} \sum_j^{N_R} \nu_{\beta,j} r_j \qquad \forall \beta = \{\mathrm{Fe}, \mathrm{FeO}, \mathrm{FeO}_{4/3}\}, \tag{6.2}$$

where $M^{(s)}$ is the molar mass of the solid oxygen storage material, which is approximated as a mean value (see Section 6.1.4). For a detailed derivation of the model equations, the reader is referred to appendix A.3.

6.1.2 Fluidized bed

The two-region model for bubbling beds with intermediate sized particles from Kunii and Levenspiel is used to model the fluidized bed reactor for RWGSCL [110] as illustrated in Fig. 6.3. One spatial dimension, z, is considered while gradients in the radial direction are neglected. Gas with the composition $x_{\alpha,\mathrm{in}}^{(g)}$ is entering the reactor with a velocity of $v^{(g)}$ (superficial velocity). Two regions are established in the reactor: the emulsion region (e) and the bubble region (b). The size of the regions is characterized by the bubble fraction δ. In the emulsion region, the solid particles are dispersed in a gas phase that rises with a velocity of $v^{(e)}$, while the bubble region is assumed to only consist of gas which is rises along the reactor at a velocity $v^{(b)}$. Therefore, the bubble region effectively acts as a gas bypass in the reactor. However, gas is exchanged between the emulsion and the bubble region with a rate that depends on the bubble-emulsion gas interchange coefficient $K^{(be)}$. Chemical reactions (r_j^M) are assumed to occur only in the emulsion region. The solid composition is denoted by $x_\beta^{(s)}(t,z)$, while the gas composition in the emulsion and bubble region is denoted by $x_\alpha^{(e)}(t,z)$ and $x_\alpha^{(b)}(t,z)$, respectively. Gas leaves the reactor with the composition $x_{\alpha,\mathrm{out}}^{(g)}$.

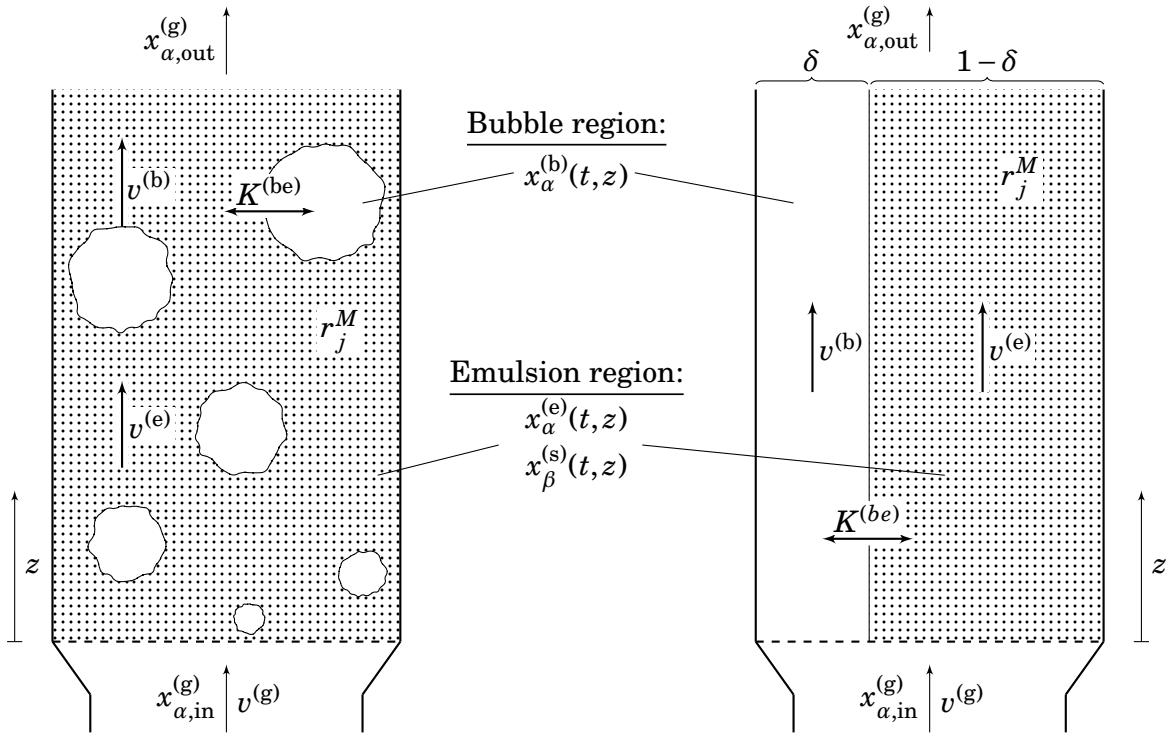

Fig. 6.3 Left: illustration of a 1D two-region, heterogeneous fluidized bed reactor with solid oxygen storage material (OSM). Right: schematic representation for modeling.

The model equations for the two-region fluidized bed model are given in the following:

$$\frac{\partial x_\alpha^{(\mathrm{b})}}{\partial t} = -v^{(\mathrm{b})}\frac{\partial x_\alpha^{(\mathrm{b})}}{\partial z} - K^{(be)}(x_\alpha^{(\mathrm{b})} - x_\alpha^{(\mathrm{e})}) \qquad \forall \alpha = \{\mathrm{H_2}, \mathrm{H_2O}, \mathrm{CO}, \mathrm{CO_2}\} \tag{6.3}$$

$$\begin{aligned}\frac{\partial x_\alpha^{(\mathrm{e})}}{\partial t} = &-v^{(\mathrm{e})}\frac{\partial x_\alpha^{(\mathrm{e})}}{\partial z} + \frac{\delta}{(1-\delta)\varepsilon_{\mathrm{mf}}}K^{(be)}(x_\alpha^{(\mathrm{b})} - x_\alpha^{(\mathrm{e})})\ldots \\ &+ \frac{1-\varepsilon_{\mathrm{mf}}}{\varepsilon_{\mathrm{mf}}}\frac{\rho^{(\mathrm{s})}}{c_{\mathrm{t}}^{(\mathrm{g})}}\sum_j^{N_R}\nu_{\alpha,j}r_j^M \qquad \forall \alpha = \{\mathrm{H_2}, \mathrm{H_2O}, \mathrm{CO}, \mathrm{CO_2}\}\end{aligned} \tag{6.4}$$

$$\frac{\partial x_\beta^{(\mathrm{s})}}{\partial t} = D_v^{(\mathrm{s})}\frac{\partial^2 x_\beta^{(\mathrm{s})}}{\partial z^2} + M^{(\mathrm{s})}\sum_j^{N_R}\nu_{\beta,j}r_j^M \qquad \forall \beta = \{\mathrm{Fe}, \mathrm{FeO}, \mathrm{FeO_{4/3}}\} \tag{6.5}$$

Here, $\varepsilon_{\mathrm{mf}}$ denotes the minimum fluidization voidage and $D_v^{(\mathrm{s})}$ the average vertical dispersion coefficient for the solid. For a detailed derivation of the model equations, the reader is referred to appendix A.4.

6.1.3 Reaction kinetics

It was verified experimentally in Chapter 5 that Fe_3O_4 is reduced to Fe via the intermediate FeO. The reverse was observed for the oxidation with CO_2 making the cycle complete. Thus, the true reaction scheme (assuming that the support metal oxide, $Ce_{0.5}Zr_{0.5}O_2$, does not participate in the reactions) is given by equations (6.6) to (6.9).

$$\mathrm{Fe} + \mathrm{CO_2} \rightleftharpoons \mathrm{FeO} + \mathrm{CO} \qquad \Delta_R h(1073\,\mathrm{K}) = 15.12\,\mathrm{kJ/mol} \tag{6.6}$$

$$\mathrm{FeO} + 1/3\,\mathrm{CO_2} \rightleftharpoons \mathrm{FeO_{4/3}} + 1/3\,\mathrm{CO} \qquad \Delta_R h(1073\,\mathrm{K}) = -3.15\,\mathrm{kJ/mol} \tag{6.7}$$

$$\mathrm{FeO_{4/3}} + 1/3\,\mathrm{H_2} \rightleftharpoons \mathrm{FeO} + 1/3\,\mathrm{H_2O} \qquad \Delta_R h(1073\,\mathrm{K}) = 15.43\,\mathrm{kJ/mol} \tag{6.8}$$

$$\mathrm{FeO} + \mathrm{H_2} \rightleftharpoons \mathrm{Fe} + \mathrm{H_2O} \qquad \Delta_R h(1073\,\mathrm{K}) = 21.72\,\mathrm{kJ/mol} \tag{6.9}$$

Due to a lack of data discriminating the intermediate reaction step through FeO from the total reaction between Fe and Fe_3O_4 the reduction and oxidation reaction was previously modeled as a single reaction from Fe_3O_4 to Fe vice versa (see Chapter 5). Using this simplification a good agreement between the TG data and the kinetic model was obtained. However, detailed process modeling requires the intermediate step to be explicitly considered because the reaction equilibrium between Fe and FeO is different from the one between FeO and Fe_3O_4. The Baur-Glaessner diagram [23] in Fig. 6.4 shows the phase equilibria for iron in its different oxidation states with

gas mixtures of H_2/H_2O and CO/CO_2. The solid and dashed lines delineate the phase

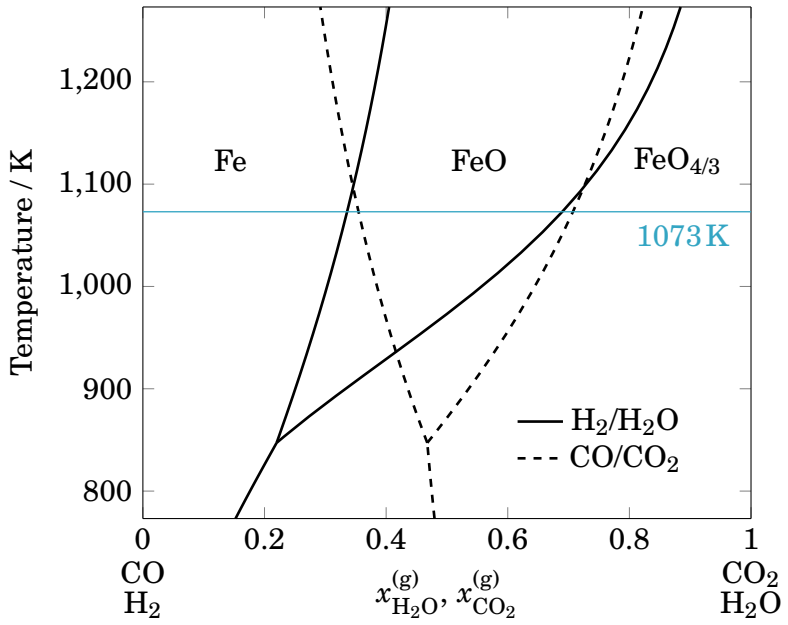

Fig. 6.4 Baur-Glaessner diagram showing the equilibrium between the oxidation states of iron with regard to the gas composition of H_2/H_2O (solid lines) and CO/CO_2 (dashed lines) mixtures. At temperatures below 847 K FeO is not stable. Data taken from [38, 29].

equilibria between the three solid phases Fe, FeO and $FeO_{4/3}$ (FeO is only stable at $T > 847\,\mathrm{K}$) with regard to the gas composition. To completely reduce $FeO_{4/3}$ to Fe at 1073 K, the hydrogen mole fraction of the surrounding gas must be $x^{(g)}_{H_2} > 0.66$. Similarly, for complete oxidation of Fe to $FeO_{4/3}$ at 1073 K, the CO_2 mole fraction must be $x^{(g)}_{CO_2} > 0.70$. Furthermore, it can be seen that the oxidation and reduction each proceed in two consecutive steps with a distinct equilibrium gas composition according to equations (6.6) to (6.9). The equilibrium conversion of CO_2 and H_2 during the oxidation and reduction stage is high for the first reaction step and low for the second reaction step, respectively. Thus, the oxidation step from Fe to FeO (see eq. (6.6)) yields a higher CO_2 conversion than the oxidation step from FeO to Fe_3O_4. Conversely, the reduction step from $FeO_{4/3}$ to FeO (see eq. (6.8)) yields a higher H_2 conversion than the reduction step from FeO to Fe.

The reaction rate expressions for the RWGSCL looping process must account for the equilibrium limitation of the reactions (equations (6.6) to (6.9)), i.e. the reaction rates must vanish at the corresponding gas-solid equilibrium lines shown in Fig. 6.4. The derivation of suitable reaction rate expressions is not as straightforward as for ho-

mogeneous gas phase reactions because the solid composition must also be accounted for in the reaction rates. In many simulation studies of CLC systems reaction rates are used that not explicitly account for the equilibrium limitation of the considered gas-solid reactions [11, 185, 78]. However, this is possible only because the reaction equilibria in CLC are generally far on the product side. This is due to the fact that generally OSMs are used that are easily reduced by CH_4, H_2 and/or CO like NiO or Cu_2O (see also Fig. 3.5). Furthermore, due to the high oxidizing potential of O_2, oxidation by air or O_2 ensures almost complete conversion for all OSMs. For RWGSCL by iron oxide the simplifying assumption of nearly complete conversion can not be applied because of the marked equilibrium limitations. Thus, it is appropriate to elaborate in more detail how thermodynamically consistent reaction rate expressions can be derived for the RWGSCL system. In the following the reaction rate derivation is presented exemplary for the oxidation reaction from Fe to FeO (see eq. (6.6)).

The total reaction rate for the equilibrium limited gas-solid reaction of Fe with CO_2 (see eq. (6.6)) can be expressed as the difference between the forward and reverse reaction rate:

$$r = r_+ - r_- = k_{p+} f(\Psi_{\mathrm{Fe}}) p_{\mathrm{CO_2}} - k_{p-} f(\Psi_{\mathrm{FeO}}) p_{\mathrm{CO}} \tag{6.10}$$

Here, r denotes the reaction rate in mol/m^3/s, k_p are the reaction rate coefficients, p_i is the partial pressure of the gas phase component i and $f(\Psi_j)$ is a function of an arbitrary parameter Ψ_j that describes the influence of the solid reactant j on the reaction rate. In heterogeneously catalyzed reactions, Ψ_j is often represented by the available surface area. However, generally this values is not easily accessible. Furthermore, the reactions considered here are not heterogeneously catalyzed reactions but true heterogeneous (mostly non-catalytic) gas-solid reactions [11]. In this work it is assumed that Ψ_j can be described using the solid mole fraction $x_j^{(\mathrm{s})}$. Noting that $p_i = p x_i^{(\mathrm{g})}$ and $k = p k_p$, equation (6.10) can be reformulated to

$$r = k_+ x_{\mathrm{Fe}}^{(\mathrm{s})} x_{\mathrm{CO_2}}^{(\mathrm{g})} - k_- x_{\mathrm{FeO}}^{(\mathrm{s})} x_{\mathrm{CO}}^{(\mathrm{g})} \tag{6.11}$$

At chemical equilibrium $r \stackrel{!}{=} 0$ must hold and the following relationship can be derived:

$$\frac{k_+}{k_-} \frac{x_{\mathrm{Fe}}^{(\mathrm{s})}}{x_{\mathrm{FeO}}^{(\mathrm{s})}} = \frac{x_{\mathrm{CO}}^{(\mathrm{g})}}{x_{\mathrm{CO_2}}^{(\mathrm{g})}} \tag{6.12}$$

Using the mass action law, the chemical equilibrium constant is related to the gas phase partial pressures according to

$$K_{\mathrm{eq}} = \prod_i \left(\frac{p_i}{p^0} \right)^{\nu_i}, \tag{6.13}$$

where p^0 is the standard pressure (0.1 MPa). Combining equations (6.12) and (6.13) yields the following relationship between the forward and reverse rate constant:

$$k_- = k_+ \frac{x_{\mathrm{Fe}}^{(\mathrm{s})}}{x_{\mathrm{FeO}}^{(\mathrm{s})}} \frac{1}{K_{\mathrm{eq}}} \tag{6.14}$$

Inserting equation (6.14) into (6.11) gives the following reaction rate expression:

$$r = k_+ x_{\mathrm{Fe}}^{(\mathrm{s})} \left(x_{\mathrm{CO_2}}^{(\mathrm{g})} - \frac{x_{\mathrm{CO}}^{(\mathrm{g})}}{K_{\mathrm{eq}}} \right) \tag{6.15}$$

Note that this expression is very similar to traditional expressions for equilibrium limited homogeneous gas phase reactions with the exception of the influence of the solid mole fraction $x_{\mathrm{Fe}}^{(\mathrm{s})}$. This distinction is crucial, however, as the driving force of the reaction is dependent not only on the composition of the gas phase but also on the composition of the solid phase. Thus, even if there is a driving force in the gas phase between CO_2 and CO the reaction rate remains zero if there is no Fe in the system as well. Equation (6.15) can be rearranged to

$$r = k_+ x_{\mathrm{Fe}}^{(\mathrm{s})} Y_{\mathrm{C}} \left(y_{\mathrm{CO_2}}^{(\mathrm{g})} - \frac{y_{\mathrm{CO}}^{(\mathrm{g})}}{K_{\mathrm{eq}}} \right), \tag{6.16}$$

where $y_{\mathrm{CO}}^{(\mathrm{g})}$ and $y_{\mathrm{CO_2}}^{(\mathrm{g})}$ denote the ratios of mole fractions according to

$$y_{\mathrm{CO}}^{(\mathrm{g})} = \frac{x_{\mathrm{CO}}^{(\mathrm{g})}}{x_{\mathrm{CO}}^{(\mathrm{g})} + x_{\mathrm{CO_2}}^{(\mathrm{g})}} \tag{6.17}$$

$$y_{\mathrm{CO_2}}^{(\mathrm{g})} = \frac{x_{\mathrm{CO_2}}^{(\mathrm{g})}}{x_{\mathrm{CO}}^{(\mathrm{g})} + x_{\mathrm{CO_2}}^{(\mathrm{g})}} \tag{6.18}$$

and Y_C is the gas phase carbon content defined by

$$Y_C = x_{CO}^{(g)} + x_{CO_2}^{(g)}. \tag{6.19}$$

To allow for different reaction mechanisms in the gas and solid phase, exponents can be introduced into equation 6.16 to yield

$$r = k_+ \left(x_{Fe}^{(s)}\right)^{n_+} Y_C \left(y_{CO_2}^{(g)} - \frac{y_{CO}^{(g)}}{K_{eq}}\right)^{m_+}. \tag{6.20}$$

The reaction order n_+ is used to describe different reaction mechanisms in the solid phase according to Table 5.1. An additional degree of freedom is obtained by adjusting the gas phase reaction order m_+. It can easily be seen that the reaction rate expression given by equation (6.20) is only valid for the forward direction of reaction 6.6 since it depends on the solid concentration of Fe. However, the reaction rate in the reverse direction must be dependent on the solid concentration of FeO instead. Therefore, (6.20) describes the reaction kinetic of reaction (6.6) only if the gas phase composition is on the left side (i.e. on the reactant side) of chemical equilibrium. An additional equation must be derived to describe the reaction kinetic on the right side (i.e. on the product side) of chemical equilibrium. The importance of using different reaction rate expressions for the forward and backward direction of equilibrium limited gas-solid reactions has been highlighted recently by Sohn [156]. This distinct behavior originates from the fact that the reaction rates of gas solid reactions are equally dependent on the composition of the gas and the solid phase. In the case of homogeneous gas phase reactions, one reaction rate is enough to describe the kinetics on both sides of chemical equilibrium. To derive a reaction rate that is valid for for the reverse direction, the reverse of reaction equation (6.6) is used:

$$FeO + CO \rightleftharpoons Fe + CO_2 \tag{6.21}$$

The same work flow is used on reaction equation (6.21) yielding the following reaction rate expression for the reverse direction (r_{rev}):

$$r_{rev} = k_- \left(x_{FeO}^{(s)}\right)^{n_-} Y_C \left(y_{CO}^{(g)} - \frac{y_{CO_2}^{(g)}}{K'_{eq}}\right)^{m_-}. \tag{6.22}$$

Note that K'_{eq} in eq. (6.22) is different from K_{eq} in eq. (6.16). However, the relationship between both variables is easily established as $K'_{\mathrm{eq}} = 1/K_{\mathrm{eq}}$, yielding

$$r_{\mathrm{rev}} = k_{-}\left(x_{\mathrm{FeO}}^{(\mathrm{s})}\right)^{n_{-}} Y_{\mathrm{C}}\left(y_{\mathrm{CO}}^{(\mathrm{g})} - K_{\mathrm{eq}} y_{\mathrm{CO_2}}^{(\mathrm{g})}\right)^{m_{-}}. \tag{6.23}$$

In general, the exponents n_{-} and m_{-} are different from the forward direction. Bringing together the equations for the forward and reverse direction (equations (6.16) and (6.22), respectively) requires a conditional statement to distinguish the direction based on the current gas composition. Using the work flow outlined above the reaction rate expressions for the remaining reactions (6.7) to (6.9) can be derived similarly. The reaction rate expressions for reaction (6.6) to (6.9) are summarized in the following:

$$r_1^M = \begin{cases} k_{1+}\left(x_{\mathrm{Fe}}^{(\mathrm{s})}\right)^{n_{1+}} Y_{\mathrm{C}}\left(y_{\mathrm{CO_2}}^{(\mathrm{g})} - \frac{y_{\mathrm{CO}}^{(\mathrm{g})}}{K_{\mathrm{eq},1}}\right)^{m_{1+}}, & \text{if } \frac{y_{\mathrm{CO}}^{(\mathrm{g})}}{y_{\mathrm{CO_2}}^{(\mathrm{g})}} < K_{\mathrm{eq},1} \\ -k_{1-}\left(x_{\mathrm{FeO}}^{(\mathrm{s})}\right)^{n_{1-}} Y_{\mathrm{C}}\left(y_{\mathrm{CO}}^{(\mathrm{g})} - K_{\mathrm{eq},1} y_{\mathrm{CO_2}}^{(\mathrm{g})}\right)^{m_{1-}}, & \text{if } \frac{y_{\mathrm{CO}}^{(\mathrm{g})}}{y_{\mathrm{CO_2}}^{(\mathrm{g})}} > K_{\mathrm{eq},1} \end{cases} \tag{6.24}$$

$$r_2^M = \begin{cases} k_{2+}\left(x_{\mathrm{FeO}}^{(\mathrm{s})}\right)^{n_{2+}} Y_{\mathrm{C}}\left(y_{\mathrm{CO_2}}^{(\mathrm{g})} - \frac{y_{\mathrm{CO}}^{(\mathrm{g})}}{K_{\mathrm{eq},2}}\right)^{m_{2+}}, & \text{if } \frac{y_{\mathrm{CO}}^{(\mathrm{g})}}{y_{\mathrm{CO_2}}^{(\mathrm{g})}} < K_{\mathrm{eq},2} \\ -k_{2-}\left(x_{\mathrm{FeO_{4/3}}}^{(\mathrm{s})}\right)^{n_{2-}} Y_{\mathrm{C}}\left(y_{\mathrm{CO}}^{(\mathrm{g})} - K_{\mathrm{eq},2} y_{\mathrm{CO_2}}^{(\mathrm{g})}\right)^{m_{2-}}, & \text{if } \frac{y_{\mathrm{CO}}^{(\mathrm{g})}}{y_{\mathrm{CO_2}}^{(\mathrm{g})}} > K_{\mathrm{eq},2} \end{cases} \tag{6.25}$$

$$r_3^M = \begin{cases} k_{3+}\left(x_{\mathrm{FeO_{4/3}}}^{(\mathrm{s})}\right)^{n_{3+}} Y_{\mathrm{H}}\left(y_{\mathrm{H_2}}^{(\mathrm{g})} - \frac{y_{\mathrm{H_2O}}^{(\mathrm{g})}}{K_{\mathrm{eq},3}}\right)^{m_{3+}}, & \text{if } \frac{y_{\mathrm{H_2O}}^{(\mathrm{g})}}{y_{\mathrm{H_2}}^{(\mathrm{g})}} < K_{\mathrm{eq},3} \\ -k_{3-}\left(x_{\mathrm{FeO}}^{(\mathrm{s})}\right)^{n_{3-}} Y_{\mathrm{H}}\left(y_{\mathrm{H_2O}}^{(\mathrm{g})} - K_{\mathrm{eq},3} y_{\mathrm{H_2}}^{(\mathrm{g})}\right)^{m_{3-}}, & \text{if } \frac{y_{\mathrm{H_2O}}^{(\mathrm{g})}}{y_{\mathrm{H_2}}^{(\mathrm{g})}} > K_{\mathrm{eq},3} \end{cases} \tag{6.26}$$

$$r_4^M = \begin{cases} k_{4+}\left(x_{\mathrm{FeO}}^{(\mathrm{s})}\right)^{n_{4+}} Y_{\mathrm{H}}\left(y_{\mathrm{H_2}}^{(\mathrm{g})} - \frac{y_{\mathrm{H_2O}}^{(\mathrm{g})}}{K_{\mathrm{eq},4}}\right)^{m_{4+}}, & \text{if } \frac{y_{\mathrm{H_2O}}^{(\mathrm{g})}}{y_{\mathrm{H_2}}^{(\mathrm{g})}} < K_{\mathrm{eq},4} \\ -k_{4-}\left(x_{\mathrm{Fe}}^{(\mathrm{s})}\right)^{n_{4-}} Y_{\mathrm{H}}\left(y_{\mathrm{H_2O}}^{(\mathrm{g})} - K_{\mathrm{eq},4} y_{\mathrm{H_2}}^{(\mathrm{g})}\right)^{m_{4-}}, & \text{if } \frac{y_{\mathrm{H_2O}}^{(\mathrm{g})}}{y_{\mathrm{H_2}}^{(\mathrm{g})}} > K_{\mathrm{eq},4} \end{cases} \tag{6.27}$$

The direction of the reaction depends on the current gas phase composition and the chemical equilibrium constant $K_{\mathrm{eq},i}$ of reaction i. The ratio of the mole fractions

of CO/CO_2 and H_2/H_2O are denoted as y_i, which are defined as follows:

$$y_{CO}^{(g)} = \frac{x_{CO}^{(g)}}{x_{CO}^{(g)} + x_{CO_2}^{(g)}} \tag{6.28}$$

$$y_{CO_2}^{(g)} = \frac{x_{CO_2}^{(g)}}{x_{CO}^{(g)} + x_{CO_2}^{(g)}} \tag{6.29}$$

$$y_{H_2}^{(g)} = \frac{x_{H_2}^{(g)}}{x_{H_2}^{(g)} + x_{H_2O}^{(g)}} \tag{6.30}$$

$$y_{H_2O}^{(g)} = \frac{x_{H_2O}^{(g)}}{x_{H_2}^{(g)} + x_{H_2O}^{(g)}} \tag{6.31}$$

The gas phase carbon and hydrogen content is defined by Y_C and Y_H, respectively:

$$Y_C = x_{CO}^{(g)} + x_{CO_2}^{(g)} \tag{6.32}$$

$$Y_H = x_{H_2}^{(g)} + x_{H_2O}^{(g)} \tag{6.33}$$

The values of n and m were experimentally determined in Chapter 5. However, kinetic parameters for the intermediate step could not determined (see Chapter 5). Therefore, it is assumed that the two reaction steps for the oxidation (equations (6.24) and (6.25)) and reduction (equations (6.26) and (6.27)) can be described by the same reaction mechanism and therefore the same reaction parameters can be used. Furthermore, the same reaction parameters are used for the forward and backward reaction rate for each reaction. This is an approximation which is used due to the lack of more detailed information about the reaction mechanism of each reaction step. Including the Arrhenius law for the kinetic parameters k, the reaction rate equations

(6.24) to (6.27) can be simplified to

$$r_1^M = \begin{cases} k_O^0 \exp\left(\frac{-E_{A,O}}{RT}\right)\left(x_{\mathrm{Fe}}^{(\mathrm{s})}\right)^{n_O} Y_{\mathrm{C}}\left(y_{\mathrm{CO_2}}^{(\mathrm{g})} - \frac{y_{\mathrm{CO}}^{(\mathrm{g})}}{K_{\mathrm{eq},1}}\right)^{m_O}, & \text{if } \frac{y_{\mathrm{CO}}^{(\mathrm{g})}}{y_{\mathrm{CO_2}}^{(\mathrm{g})}} < K_{\mathrm{eq},1} \\ -k_O^0 \exp\left(\frac{-E_{A,O}}{RT}\right)\left(x_{\mathrm{FeO}}^{(\mathrm{s})}\right)^{n_O} Y_{\mathrm{C}}\left(y_{\mathrm{CO}}^{(\mathrm{g})} - K_{\mathrm{eq},1} y_{\mathrm{CO_2}}^{(\mathrm{g})}\right)^{m_O}, & \text{if } \frac{y_{\mathrm{CO}}^{(\mathrm{g})}}{y_{\mathrm{CO_2}}^{(\mathrm{g})}} > K_{\mathrm{eq},1} \end{cases} \tag{6.34}$$

$$r_2^M = \begin{cases} k_O^0 \exp\left(\frac{-E_{A,O}}{RT}\right)\left(x_{\mathrm{FeO}}^{(\mathrm{s})}\right)^{n_O} Y_{\mathrm{C}}\left(y_{\mathrm{CO_2}}^{(\mathrm{g})} - \frac{y_{\mathrm{CO}}^{(\mathrm{g})}}{K_{\mathrm{eq},2}}\right)^{m_O}, & \text{if } \frac{y_{\mathrm{CO}}^{(\mathrm{g})}}{y_{\mathrm{CO_2}}^{(\mathrm{g})}} < K_{\mathrm{eq},2} \\ -k_O^0 \exp\left(\frac{-E_{A,O}}{RT}\right)\left(x_{\mathrm{FeO_{4/3}}}^{(\mathrm{s})}\right)^{n_O} Y_{\mathrm{C}}\left(y_{\mathrm{CO}}^{(\mathrm{g})} - K_{\mathrm{eq},2} y_{\mathrm{CO_2}}^{(\mathrm{g})}\right)^{m_O}, & \text{if } \frac{y_{\mathrm{CO}}^{(\mathrm{g})}}{y_{\mathrm{CO_2}}^{(\mathrm{g})}} > K_{\mathrm{eq},2} \end{cases} \tag{6.35}$$

$$r_3^M = \begin{cases} k_R^0 \exp\left(\frac{-E_{A,R}}{RT}\right)\left(x_{\mathrm{FeO_{4/3}}}^{(\mathrm{s})}\right)^{n_R} Y_{\mathrm{H}}\left(y_{\mathrm{H_2}}^{(\mathrm{g})} - \frac{y_{\mathrm{H_2O}}^{(\mathrm{g})}}{K_{\mathrm{eq},3}}\right)^{m_R}, & \text{if } \frac{y_{\mathrm{H_2O}}^{(\mathrm{g})}}{y_{\mathrm{H_2}}^{(\mathrm{g})}} < K_{\mathrm{eq},3} \\ -k_R^0 \exp\left(\frac{-E_{A,R}}{RT}\right)\left(x_{\mathrm{FeO}}^{(\mathrm{s})}\right)^{n_R} Y_{\mathrm{H}}\left(y_{\mathrm{H_2O}}^{(\mathrm{g})} - K_{\mathrm{eq},3} y_{\mathrm{H_2}}^{(\mathrm{g})}\right)^{m_R}, & \text{if } \frac{y_{\mathrm{H_2O}}^{(\mathrm{g})}}{y_{\mathrm{H_2}}^{(\mathrm{g})}} > K_{\mathrm{eq},3} \end{cases} \tag{6.36}$$

$$r_4^M = \begin{cases} k_R^0 \exp\left(\frac{-E_{A,R}}{RT}\right)\left(x_{\mathrm{FeO}}^{(\mathrm{s})}\right)^{n_R} Y_{\mathrm{H}}\left(y_{\mathrm{H_2}}^{(\mathrm{g})} - \frac{y_{\mathrm{H_2O}}^{(\mathrm{g})}}{K_{\mathrm{eq},4}}\right)^{m_R}, & \text{if } \frac{y_{\mathrm{H_2O}}^{(\mathrm{g})}}{y_{\mathrm{H_2}}^{(\mathrm{g})}} < K_{\mathrm{eq},4} \\ -k_R^0 \exp\left(\frac{-E_{A,R}}{RT}\right)\left(x_{\mathrm{Fe}}^{(\mathrm{s})}\right)^{n_R} Y_{\mathrm{H}}\left(y_{\mathrm{H_2O}}^{(\mathrm{g})} - K_{\mathrm{eq},4} y_{\mathrm{H_2}}^{(\mathrm{g})}\right)^{m_R}, & \text{if } \frac{y_{\mathrm{H_2O}}^{(\mathrm{g})}}{y_{\mathrm{H_2}}^{(\mathrm{g})}} > K_{\mathrm{eq},4} \end{cases} \tag{6.37}$$

where k^0, E_A, n and m are kinetic parameters for the oxidation (index O) and reduction (index R) reactions. For the reaction rate equations (6.34) to (6.37) the kinetic parameters estimated in Chapter 5 (see Table Table 5.2) are used.

6.1.4 Model parameters and fluid dynamics

A reactor length of $L = 2\,\mathrm{m}$ is chosen which corresponds to a small scale industrial fixed bed reactor. The effectiveness factor of the RWGS reaction on Ni-catalyst particles with a mean diameter of 3 mm was estimated by Wolf *et al.* to be $\eta_{\mathrm{eff}} = 0.1$ [180]. Hertel *et al.* found a value of $\eta_{\mathrm{eff}} = 0.3$ for iron oxide particles with a mean diameter of 3 mm [84]. Therefore, a mean value for the effectiveness factor of $\eta_{\mathrm{eff}} = 0.2$ was chosen. For the solid, a mean density of $\rho^{(\mathrm{s})} = 6000\,\mathrm{kg/m^3}$ [182] and a mean molar mass of $M^{(\mathrm{s})} = 67\,\mathrm{g/mol}$ are assumed. The fixed bed void fraction is set to $\varepsilon = 0.5$, according to Hertel *et al.* [84]. Both reactor configurations are operated isothermally at $T = 1073\,\mathrm{K}$ and $p = 1\,\mathrm{atm}$. From a theoretical perspective the temperature should be as high as possible to shift the reaction equilibrium to the product side (since all reactions except for one are endothermic) and to accelerate the reaction kinetics. However, from a practical point of view high temperature leads to material stability problems and

it has been shown in our previous work that 1073 K is the highest permissible temperature for 80 wt% Fe_2O_3 to allow for repeated cycling without too severe material degradation [175]. Different temperatures during oxidation and reduction were not permitted in this work because it has been mentioned numerous times in the literature that the necessary heat recuperation between the two steps in non-isothermal operation is severely decreasing the energy efficiency [130]. Therefore, isothermal operation is preferred for chemical looping processes. Standard pressure is chosen since the used kinetic parameters (see Table 5.2) were determined at that pressure. Since all reactions are equimolar there is no pressure dependence of the equilibrium composition. The total gas concentration $c_t^{(g)}$ is calculated using the ideal gas law. For the calculation of the chemical equilibrium constants, K_{eq}, thermodynamic data from CRC Handbook and Yaws were used [80, 182]. For the reaction rate equations (6.34) to (6.37) the kinetic parameters estimated in Chapter 5 (see Table 5.2) are used.

The flow field in the fluidized bed is not solved explicitly *via* the momentum balance but semi-empirical relationships are used to characterize the fluid dynamic behavior of the reactor. This is a typical approach for fluidized bed reactor modeling and yields a reasonable compromise between model simplicity and level of detail. The relationships used in this work are based on the model by Kunii and Levenspiel for intermediate sized particles [110]. The mean particle size for the oxygen storage material is $d_p = 250\,\mu m$ (Geldart Type B [70]). A fluidized bed reactor is assumed with an inner diameter of $d_t = 0.8\,m$ and a bed height of $L = 2\,m$ at fluidization conditions to be comparable in size to the fixed bed reactor. The minimum fluidization voidage is approximated to be $\varepsilon_{mf} = 0.55$, according to Kunii and Levenspiel [111]. Thus, the total amount of OSM inside the reactor is $2059.1\,kg_{OSM}$ (for the fixed bed reactor to hold the same amount of OSM the reactor diameter must be $d_t = 0.661\,m$). All values refer to one reactor since only one reactor needed to be simulated to model the system. The minimum fluidization velocity v_{mf} can be calculated according to eq. (6.38) [111]:

$$v_{mf} = \frac{\mu}{d_p \rho^{(g)}} \left(\sqrt{28.7^2 + 0.0494 \left(\frac{d_p^3 \rho^{(g)} (\rho^{(s)} - \rho^{(g)}) g}{\mu^2} \right)} - 28.7 \right) \tag{6.38}$$

Here, the gas phase density and the dynamic viscosity are denoted by $\rho^{(g)}$ and μ, respectively. Mean values of all gas components are used as an approximation since the actual gas composition changes along the reactor. Thus, at a temperature of 1073 K the gas phase density and the dynamic viscosity are $\rho^{(g)} = 0.261\,\mathrm{kg/m^3}$ and $\mu = 3.66 \times 10^{-5}\,\mathrm{Pas}$, respectively. The ideal gas law is used for calculating the gas density. The dynamic viscosity is calculated by a correlation from VDI Wärmeatlas [71]. The correlation is only valid for $T < 773\,\mathrm{K}$ but since there are no values available for the gas viscosity at the process temperature, this correlation is extrapolated. We assume that the values give a reasonable approximation of the true viscosity. The emulsion phase velocity $v^{(e)}$ is calculated by eq. (6.39).

$$v^{(e)} = \frac{2}{3} v_{mf} + \frac{1}{3} v^{(g)} \tag{6.39}$$

Here, $v^{(g)}$ is the superficial inlet velocity into the reactor, which is assumed to be 0.6 m/s in both reaction stages (this corresponds to a bubbling fluidized bed regime according to Kunii and Levenspiel [111]). For the calculation of the bubble phase velocity $v^{(b)}$, the bubble diameter has to be known first. From eq. (6.40), the bubble diameter at height z can be estimated.

$$d_b = d_{bm} - (d_{bm} - d_{b0}) \exp(-0.3 z / d_t) \tag{6.40}$$

The initial bubble size d_{b0} and the limiting bubble size d_{bm} can be estimated by the following equations:

$$d_{b0} = \frac{2.78}{g} (v^{(g)} - v_{mf})^2 \tag{6.41}$$

$$d_{bm} = 0.65 \left[\frac{\pi}{4} d_t^2 (v^{(g)} - v_{mf}) \right]^{0.4}, \qquad [\mathrm{m}] \tag{6.42}$$

Thus, at height $z = 1\,\mathrm{m}$ the bubble size is estimated to be $d_b = 0.1\,\mathrm{m}$. The bubble rise velocity v_{br} for single bubbles is given by eq. (6.43).

$$v_{br} = 0.711 (g d_b)^{1/2} \tag{6.43}$$

With v_{br}, the bubble gas velocity can be estimated by eq. (6.44).

$$v^{(b')} = v^{(g)} - v_{mf} + v_{br} \tag{6.44}$$

For the model, the rise velocity of bubble gas

$$v^{(\mathrm{b})} = v^{(\mathrm{b'})} + 3v_{\mathrm{mf}} \tag{6.45}$$

is used instead of the bubble gas velocity $v^{(\mathrm{b'})}$. The gas interchange coefficient between bubble and emulsion phase $K^{(be)}$ can be estimated from the minimum fluidization velocity and the particle diameter by eq. (6.46).

$$K^{(be)} = 4.5\left(\frac{v_{\mathrm{mf}}}{d_b}\right) \tag{6.46}$$

The average vertical dispersion coefficient of the solids $D_v^{(\mathrm{s})}$ is estimated by eq. (6.47).

$$D_v^{(\mathrm{s})} = 0.3 d_{\mathrm{t}}^{0.65}, \qquad [\mathrm{m}^2/\mathrm{s}] \tag{6.47}$$

The bubble fraction δ is calculated according to the following equation.

$$\delta = \frac{v_0 - v_{\mathrm{mf}}}{v_b} \tag{6.48}$$

6.1.5 Optimization

An important value for process characterization is the degree of reduction of the oxygen storage material, denoted by α. By definition, $\alpha = 1$ for $x_{\mathrm{Fe}}^{(\mathrm{s})} = 1$ and $\alpha = 0$ for $x_{\mathrm{FeO_{4/3}}}^{(\mathrm{s})} = 1$. For $x_{\mathrm{FeO}}^{(\mathrm{s})} = 1$, 25 % of the available oxygen is released, i.e. $\alpha = 0.25$. Thus, the degree of reduction can be calculated from the solid mole fractions according to

$$\alpha(t,z) = x_{\mathrm{Fe}}^{(\mathrm{s})}(t,z) + 0.25 x_{\mathrm{FeO}}^{(\mathrm{s})}(t,z). \tag{6.49}$$

Due to the cyclic nature of the RWGSCL process at least two reactors are needed for continuous production of syngas. Fernández and Abanades designed a continuous chemical looping combustion (CLC) system consisting of eight reactors [59]. In a similar work by Spallina *et al.* 16 reactors were reported [159]. However, in CLC more process steps are involved (heat removal, purging) which are not necessary for RWGSCL. Thus, intelligent design and optimized process parameters may lead to a

minimum number of reactors. For the following optimization problem, a fixed number of two reactors is assumed to simplify the process design and operation.

The duration of the oxidation and the reduction phase are denoted as t_{Ox} and t_{Red}, respectively, and are optimized for the fixed and fluidized bed reactor design. The most important criterion for continuous production of syngas is that the duration of the reduction phase (regeneration of the reactor) is shorter than the oxidation phase (production of CO), i.e. $t_{\mathrm{Red}} < t_{\mathrm{Ox}}$ assuming that switching of the gas streams occurs instantly. To change the duration of the two phases, the gas flow velocities $v^{(\mathrm{g})}_{\mathrm{in,Ox}}$ and $v^{(\mathrm{g})}_{\mathrm{in,Red}}$ were adjusted as well. However, higher gas flows and shorter reaction times lead to incomplete OSM utilization in the reactor and/or decreased gas conversion. Furthermore, the gas flow velocities can only be adjusted in the fixed bed reactor design. For fluidized bed operation, the gas inlet velocities must be fixed to yield defined flow characteristics.

To analyze process operation, two performance indicators were defined in this work. The first indicator is the OSM utilization which is quantified by the difference of the spatial mean value of the reduction extent ($\bar{\alpha}$) at the end of each reaction phase. In the reduction stage, the reduction extent should approach one to ensure the highest OSM utilization. Equivalently, in the oxidation stage, the reduction extent preferably approaches zero. The OSM utilization, denoted by X_{OSM}, is defined by the following term:

$$X_{\mathrm{OSM}} = \bar{\alpha}_{\mathrm{Red}}(t = t_{\mathrm{Red}}) - \bar{\alpha}_{\mathrm{Ox}}(t = t_{\mathrm{Ox}}) \tag{6.50}$$

Thus, complete reduction of the OSM after the reduction stage and complete oxidation of the OSM after the oxidation stage yields an OSM utilization of $X_{\mathrm{OSM}} = 1$. High values for X_{OSM} lead to reduced reactor size and costs as the OSM is used more effectively.
The second performance indicator is the average CO concentration in the outlet gas of during the oxidation stage which is defined by the following term,

$$\bar{x}_{\mathrm{CO}} = \int_0^{t_{\mathrm{Ox}}} x^{(\mathrm{g})}_{\mathrm{CO,out}}(t)\mathrm{d}t \tag{6.51}$$

where $x^{(\mathrm{g})}_{\mathrm{CO,out}}(t)$ is the mole fraction of CO at the reactor outlet during the oxidation phase. High average CO concentrations are preferable for downstream product purification.

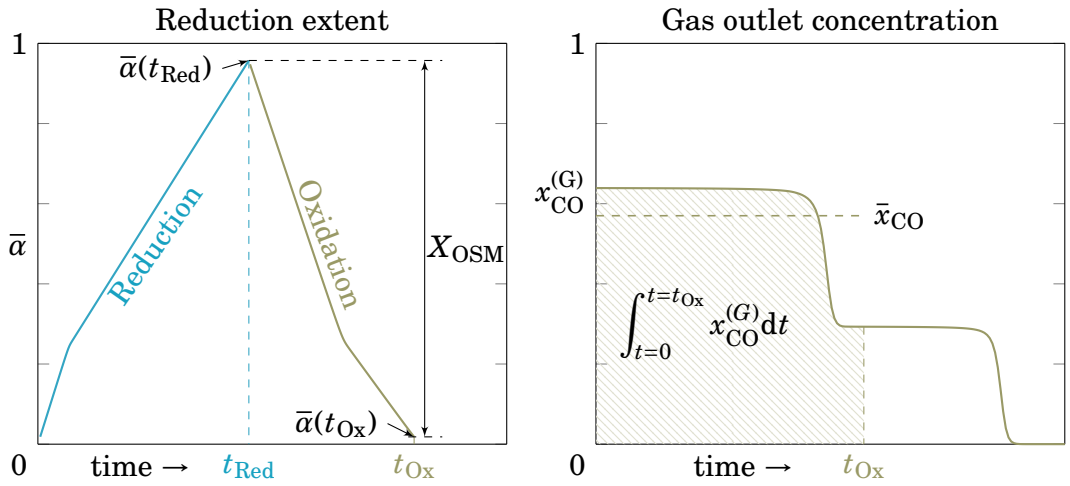

Fig. 6.5 Illustration of the OSM utilization (X_{OSM}, left) and the average CO concentration ($\bar{x}_{\mathrm{CO}}$, right) as an optimization target. For both performance indicators high values are desirable.

The performance indicators are illustrated in Fig. 6.5. Both performance indicators are important for efficient process operation. However, the two indicators are competing and a trade-off solution must be found between these two values for both reactor designs. To further ensure feasible and efficient operation, additional constraints are introduced in the following. The use of hydrogen in the reduction stage should be minimized, since its sustainable production is the most energy consuming step in the production of syngas *via* RWGSCL [176]. Thus, we define that the mole fraction of H_2 in the outlet stream during the reduction stage should not exceed a value of $x_{\mathrm{H_2,out}}^{(\mathrm{g})} = 0.99$. This ensures a reasonable H_2 conversion in the reduction stage and excessive H_2 slip is minimized. Furthermore, a minimum outlet CO concentration should be ensured during the oxidation phase to allow for efficient downstream purification. Downstream gas purification typically prefers a steady gas composition. In this work, the value for the minimum outlet CO concentration was set to $x_{\mathrm{CO,out}}^{(\mathrm{g})} = 0.1$.

Optimization problems are formulated as the maximization of the previously defined performance indicators under the mentioned operation constraints.

Fixed bed reactor

Maximizing the OSM utilization X_{OSM}:

$$\begin{aligned} \max_{t_{\mathrm{Red}}, t_{\mathrm{Ox}}, v^{(\mathrm{g})}_{\mathrm{Red}}, v^{(\mathrm{g})}_{\mathrm{Ox}}} \quad & X_{\mathrm{OSM}} \\ \text{s.t.} \quad & \text{Fixed bed model equations} \\ & t_{\mathrm{Red}} \leq t_{\mathrm{Ox}} \\ & x^{(\mathrm{g})}_{\mathrm{H_2,out}}(t) \leq 0.99 \\ & x^{(\mathrm{g})}_{\mathrm{CO,out}}(t) \geq 0.1 \end{aligned} \tag{6.52}$$

The decision variables for optimization of the fixed bed reactor are the period times t_{Red} and t_{Ox} as well as the gas inlet velocities $v^{(\mathrm{g})}_{\mathrm{Red}}$ and $v^{(\mathrm{g})}_{\mathrm{Ox}}$ for the reduction and the oxidation stage, respectively.

Maximizing the average CO concentration $\bar{x}_{\mathrm{CO}}$ at the reactor outlet during the oxidation stage:

$$\begin{aligned} \max_{t_{\mathrm{Red}}, t_{\mathrm{Ox}}, v^{(\mathrm{g})}_{\mathrm{Red}}, v^{(\mathrm{g})}_{\mathrm{Ox}}} \quad & \bar{x}_{\mathrm{CO}} \\ \text{s.t.} \quad & \text{Fixed bed model equations} \\ & t_{\mathrm{Red}} \leq t_{\mathrm{Ox}} \\ & x^{(\mathrm{g})}_{\mathrm{H_2,out}}(t) \leq 0.99 \\ & x^{(\mathrm{g})}_{\mathrm{CO,out}}(t) \geq 0.1 \end{aligned} \tag{6.53}$$

Fluidized bed reactor

Maximizing the OSM utilization X_{OSM}:

$$\begin{aligned} \max_{t_{\mathrm{Red}}, t_{\mathrm{Ox}}} \quad & X_{\mathrm{OSM}} \\ \text{s.t.} \quad & \text{Fluidized bed model equations} \\ & t_{\mathrm{Red}} \leq t_{\mathrm{Ox}} \\ & x^{(\mathrm{g})}_{\mathrm{H_2,out}}(t) \leq 0.99 \\ & x^{(\mathrm{g})}_{\mathrm{CO,out}}(t) \geq 0.1 \end{aligned} \tag{6.54}$$

For the fluidized bed reactor, the decision variables are only the period times t_{Red} and t_{Ox} for the reduction and the oxidation stage, respectively.

Maximizing the average CO concentration $\bar{x}_{CO}$ at the reactor outlet during the oxidation stage:

$$\begin{aligned} \max_{t_{Red},t_{Ox}} \quad & \bar{x}_{CO} \\ \text{s.t.} \quad & \text{Fluidized bed model equations} \\ & t_{Red} \leq t_{Ox} \\ & x^{(g)}_{H_2,out}(t) \leq 0.99 \\ & x^{(g)}_{CO,out}(t) \geq 0.1 \end{aligned} \tag{6.55}$$

6.1.6 Solution strategy

The model equations of the fixed and fluidized bed reactor designs are discretized with the finite volume method (FVM). The resulting system of ordinary differential equations (ODEs) is solved with the *ode15s* solver in MATLAB. Discretization and subsequent solution of the ODE system was found to be faster than a full discretization approach by Munera Parra *et al.* for a similar problem [138]. The piecewise defined reaction rate equations yields a sudden (non-smooth) change in the reaction rate when the gas composition changes from one side of chemical equilibrium to the other. This can lead to a crash in standard numerical solvers like *ode15s* in MATLAB since the rate expressions are not continuously differentiable. Thus, relaxation techniques were used to approximate the piecewise defined functions by differentiable functions (for further explanation see appendix A.5). To assess the real process performance, the process has to be simulated several times until the cyclic steady-state (CSS) is reached. The CSS solution is obtained by successive substitution, i.e. the end state of one simulation is used for the initial values for the next simulation until the CSS is reached. The criterion for CSS is defined as

$$\sum_{z=0}^{L} \left(x^{(s)}_{new}(t_{Red},z) - x^{(s)}_{old}(t_{Red},z) \right)^2 + \sum_{z=0}^{L} \left(x^{(s)}_{new}(t_{Ox},z) - x^{(s)}_{old}(t_{Ox},z) \right)^2 < 1 \times 10^{-3}$$

Here, $x^{(s)}_{new}$ and $x^{(s)}_{old}$ denote the solid composition at the respective period time of the reduction and oxidation phase, t_{Red} and t_{Ox}. Thus, CSS is reached when the sum of squared errors between the solids composition of the new and the old simulation run is be below 1×10^{-3}. Depending on the operating parameters, up to 50 simulation runs have to be computed to reach CSS. The optimization problem is superimposed on top of the simulation and was solved with MATLAB's *fminsearch* function, where the optimization constraints were formulated as penalty terms in the objective function.

In each iteration step of the optimization, the process has to be simulated until CSS is reached.

6.2 Results and discussion

The piecewise defined kinetic expressions coupled with the inherently dynamic behavior of the RWGSCL process give rise to complex phenomena which are analyzed and discussed in the following. All the results given correspond to the cyclic steady state condition.

6.2.1 Simulation

Process simulation is used prior to optimization to analyze and understand the general process characteristics and behaviour. Therefore, the optimization constraints discussed in Section 6.1.5 are not applied yet. Two different reaction regimes can be established in the process: an equilibrium limited reaction regime and a rate limited reaction regime. The first case is characterized by low gas velocity (long residence time). Therefore, the gas entering the reactor reacts with the solid and reaches chemical equilibrium almost instantly. Conversely, the rate limited reaction regime is characterized by high gas velocity (short residence time). The reaction kinetics dominate the process dynamics and the gas only reacts to a certain extent, i.e. chemical equilibrium is not reached inside of the reactor. In Fig. 6.6, the simulation results for the equilibrium limited reaction regime are depicted for the fixed bed reactor. In Fig. 6.6 the change of the reaction extent of the OSM throughout the reactor is depicted over time. During reduction, two distinct reaction fronts can be identified, one from Fe to FeO and another from FeO to $FeO_{4/3}$. This leads to two composition changes in the gas outlet as can be seen in Fig. 6.6. However, during oxidation the two reaction fronts are overlapping and merge into one reaction front. Consequently, the gas outlet only shows one composition change. Heidebrecht *et al.* conducted a wave analysis for a cyclic water-gas shift reactor to investigate the behavior of reaction fronts [81]. It was shown that the reaction front velocities depend mainly on the chemical equilibria and the stoichiometry of the reactions. Under the conditions investigated in this work, the two reaction fronts in the reduction stage have different velocities. This is due to two reasons: 1) the equilibrium composition of second reaction step from FeO to Fe is on the reactant side, i.e. $K_{\mathrm{eq}} < 1$ (see Fig. 6.4) and 1 mol oxygen must be exchanged

between the gas and the solid phase (compared to 1/3 mol oxygen in the first reaction step). The combination of these two factors leads to a low reaction front velocity. The second reaction step is limiting and the two reaction fronts separate during reduction. Conversely, during oxidation the first reaction step from Fe to FeO is limiting and therefore the two reaction fronts are moving with the same velocity. Notice that complete reduction is achieved after about 128.5 h while the material is completely oxidized after 93 h already. Thus, continuous process operation with an OSM utilization of 100% is not possible in this reaction regime when only two reactors are considered because the regeneration stage (reduction) must be faster than the production stage (oxidation).

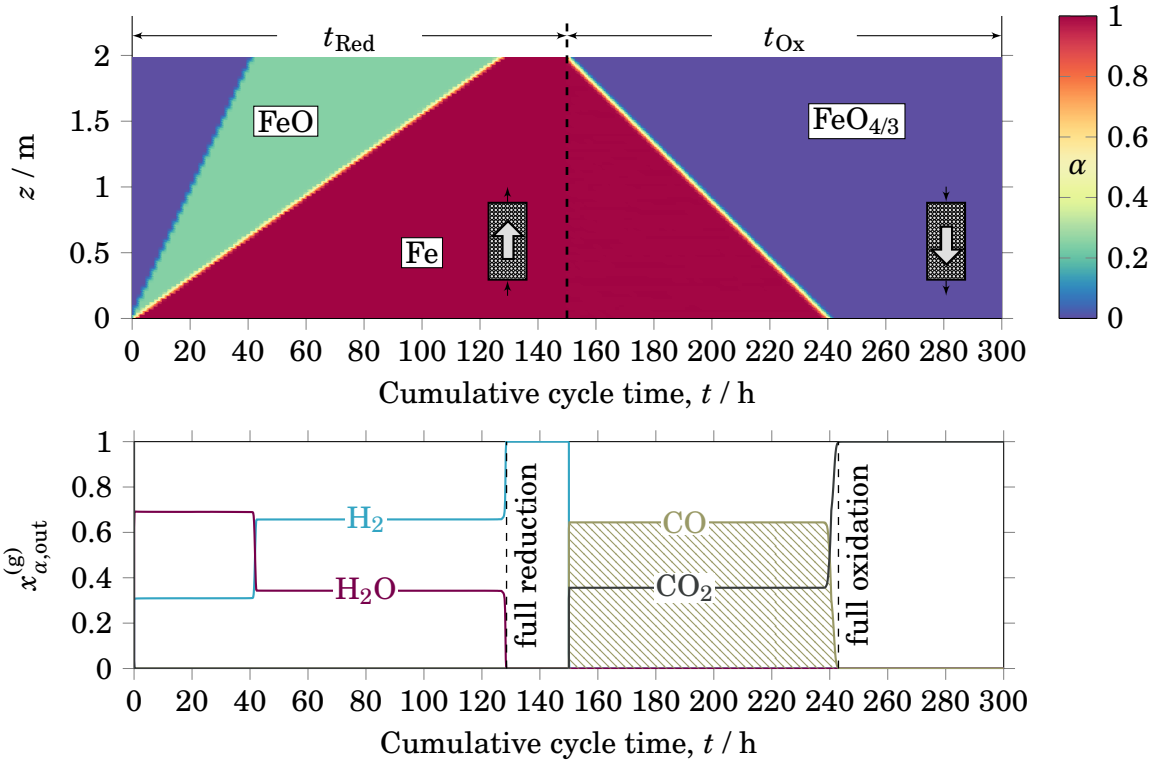

Fig. 6.6 Simulation results for the fixed bed reactor design with $v^{(g)}_{Red} = v^{(g)}_{Ox} = 0.05$ m/s and $t_{Red} = t_{Ox} = 150$ h (equilibrium limited reaction regime). Reduction extent α as a function of time and axial coordinate z (top) and gas outlet concentration $x^{(g)}_{\alpha,out}$ as a function of time (bottom). Complete reduction and oxidation achieved after 128.5 h and 93 h, respectively ($X_{OSM} = 100\%$). Inset indicates the gas flow direction in each stage (reverse-flow).

Fig. 6.7 shows the simulation results for the rate limited reaction regime, i.e. high gas velocities and short residence time. Neither for the reduction nor the oxidation stage clear reaction fronts can be identified compared to the equilibrium limited re-

action regime. Instead, both reaction steps occur simultaneously and the material is gradually reduced and oxidized. The high gas velocities in both stages lead to period times much shorter than under equilibrium limited reaction conditions. However, due to the short residence time chemical equilibrium is not reached inside of the reactor and the gas conversion decreases. This leads to a gradually decreasing CO concentration in the gas outlet and a low average CO concentration during the oxidation stage. Furthermore, the low conversion of H_2 during the reduction stage leads to a higher overall energy demand as H_2 production is the most energy consuming part of the overall process [176]. However, the unreacted H_2 can be separated and recycled easily by condensing the water in the outlet stream during reduction. An important difference compared to the equilibrium limited case is that complete reduction is achieved in less time ($\approx 2.2\,\mathrm{h}$) than complete oxidation ($\approx 3\,\mathrm{h}$). Consequently, in the rate limited reaction regime a continuous process operation with an OSM utilization of 100% is possible with only two reactors. It can be concluded that the overall process behavior is strongly dependent on the selected gas inlet velocities.

For the fluidized bed reactor design, the gas flow velocities are fixed to $v_{\mathrm{Red}}^{(\mathrm{g})} = v_{\mathrm{Ox}}^{(\mathrm{g})} = 0.6\,\mathrm{m/s}$ to yield a bubbling fluidized bed behavior. Therefore, only one case was studied here in contrast to the fixed bed reactor design. Fig. 6.8 shows the solid composition as a function of time (under the investigated conditions the solids are perfectly mixed, i.e. there is no spatial gradient along z). In both stages, the reaction steps proceed consecutively, i.e. the second reaction step starts only after completion of the first reaction step. This is due to the perfect mixing of the OSM inside the reactor. Furthermore, the gas entering the reactor is in chemical equilibrium almost instantly (see equilibrium limited reaction regime in the fixed bed case). In the beginning of the reduction stage, the H_2 outlet concentration is $x_{\mathrm{H_2}}^{(\mathrm{g})} = 0.31$ (corresponding to the equilibrium concentration of the first reaction step from $FeO_{4/3}$ to FeO). However, as mentioned in Section 6.1.3, for reduction of FeO to Fe the H_2 concentration must be at least $x_{\mathrm{H_2}}^{(\mathrm{g})} = 0.66$. Thus, the reaction from FeO to Fe will not proceed since the reduction potential of the gas is too low. The two reactions from Fe to FeO and from FeO to $FeO_{4/3}$ in the oxidation stage proceed in consecutively for the same reason. This leads to two distinct concentration fronts in the gas outlet during oxidation and reduction. Similarly to the fixed bed reactor design with low gas velocities, the reduction is shorter than the oxidation, i.e. complete reduction is achieved after 11.7 h while complete oxidation is achieved already after 7.4 h. Therefore, with the fluidized bed reactor configuration a continuous process operation with an OSM utilization of 100% is not achievable when only two reactors are considered.

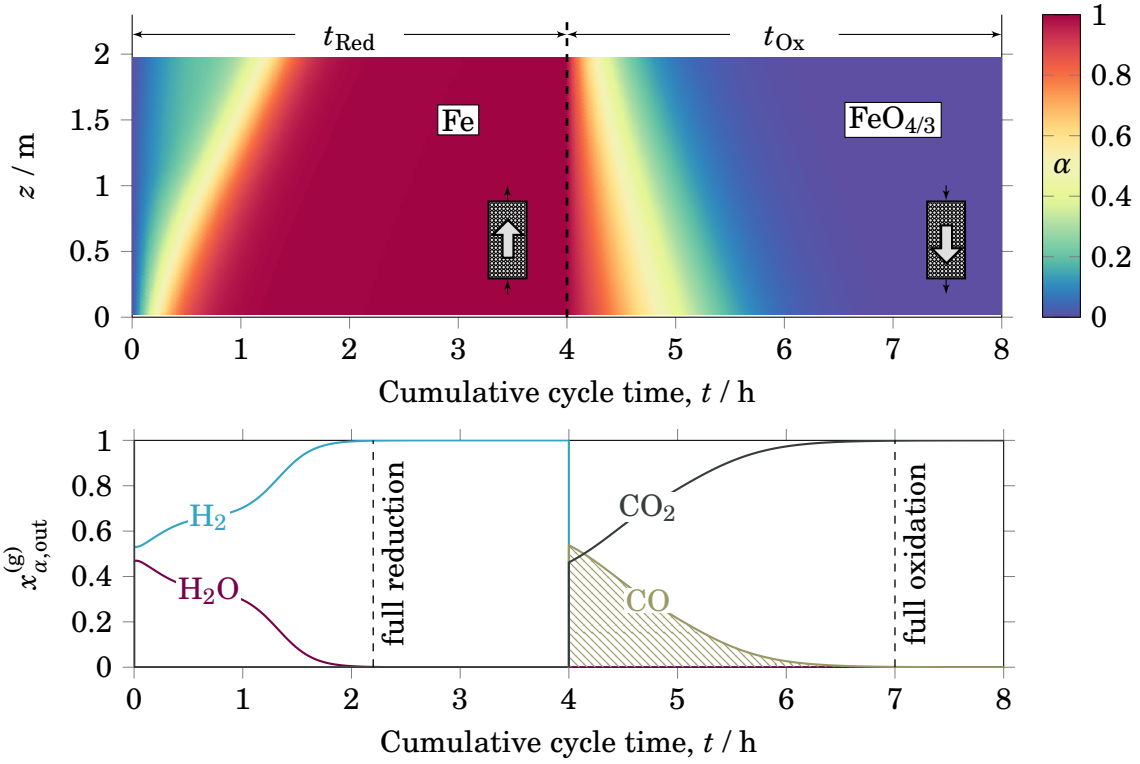

Fig. 6.7 Simulation results for the fixed bed reactor design with $v^{(g)}_{Red} = v^{(g)}_{Ox} = 6\,m/s$ and $t_{Red} = t_{Ox} = 4\,h$ (rate limited reaction regime). Reduction extent α as a function of time and axial coordinate z (top) and gas outlet concentration $x^{(g)}_{\alpha,out}$ as a function of time (bottom). Complete reduction and oxidation achieved after $\approx 2.2\,h$ and $\approx 3\,h$, respectively ($X_{OSM} = 100\%$). Inset indicates the gas flow direction in each stage (reverse-flow).

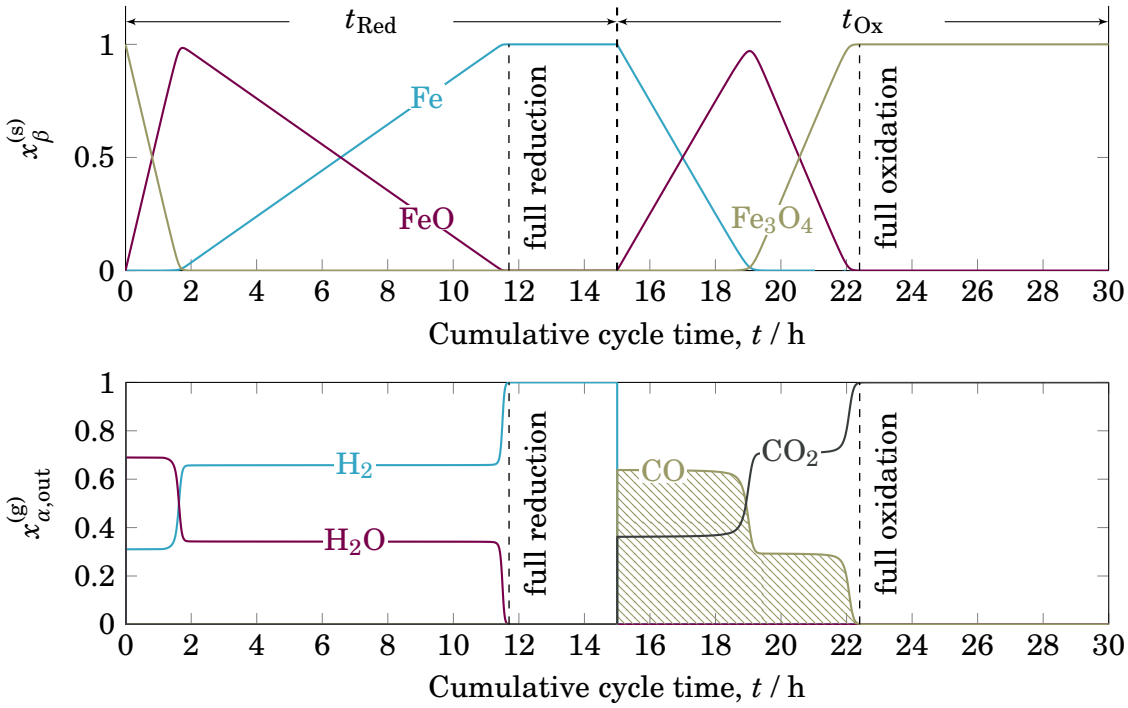

Fig. 6.8 Simulation results for the fluidized bed reactor design with $v_{\mathrm{Red}}^{(g)} = v_{\mathrm{Ox}}^{(g)} = 0.6\,\mathrm{m/s}$ and $t_{\mathrm{Red}} = t_{\mathrm{Ox}} = 15\,\mathrm{h}$. Reduction extent α as a function of time and axial coordinate z (top) and gas outlet concentration $x_{\alpha,\mathrm{out}}^{(g)}$ as a function of time (bottom). Complete reduction and oxidation achieved after 11.6 h and 7.3 h, respectively ($X_{\mathrm{OSM}} = 100\%$).

6.2.2 Optimization

Both reactor designs were optimized with regard to the average CO concentration and the OSM utilization as defined in Section 6.1.5. The results for maximizing the OSM utilization for the fixed bed reactor design (see equation (6.52)) are shown in Fig. 6.9. A period time ($t_{\mathrm{Red}} = 3.53\,\mathrm{h}$) and a gas velocity ($v_{\mathrm{Red}}^{(\mathrm{g})} = 2.04\,\mathrm{m/s}$) are optimal for reduction. Thus, the reduction stage is shorter than the oxidation stage as specified by the constraints to enable quasi-continuous operation with only two reactors. The period time of the oxidation stage is longer ($t_{\mathrm{Ox}} = 4.90\,\mathrm{h}$) and a low gas velocity ($v_{\mathrm{Ox}}^{(\mathrm{g})} = 1.07\,\mathrm{m/s}$) is optimal. Thus, the reactor conditions during oxidation are such that the gas composition is close to equilibrium. The optimal solution for the maximum OSM utilization is $X_{\mathrm{OSM}} = 98.6\%$ with an average CO concentration of $\bar{x}_{\mathrm{CO}} = 0.55$. The outlet CO mole fraction stays relatively constant at $x_{\mathrm{CO,out}} = 0.64$ for the first three hours of the oxidation stage and then gradually decreases.

The maximum achievable value for $\bar{x}_{\mathrm{CO}}$ in the fixed bed case is obtained by solving equation (6.53). The results are shown in Fig. 6.10. Compared to Fig. 6.9 the reduction stage is even shorter and the gas velocity higher while the reverse is true for the oxidation stage. This leads to sharper reaction fronts during the oxidation stage, which is beneficial for obtaining high average CO concentrations. The average CO concentration under the chosen process constraints is $\bar{x}_{\mathrm{CO}} = 0.64$ since the outlet mole fraction $x_{\mathrm{CO,out}}$ is constant during oxidation. This value is limited by the equilibrium composition of the reaction from Fe to FeO (eq. (6.6)). However, the higher value for $\bar{x}_{\mathrm{CO}}$ is achieved at the expense of the OSM utilization, which is decreased to $X_{\mathrm{OSM}} = 83.9\%$. Even though low flow velocities during oxidation are beneficial for achieving the highest possible value for $\bar{x}_{\mathrm{CO}}$, they would result in large reactors to achieve high throughput in industrial applications.

For the fluidized bed reactor, the optimal solutions of the problems defined by equations (6.54) and (6.55) are very similar and therefore only the solution for maximum OSM utilization is depicted in Fig. 6.11. Maximizing the average CO concentration (equation (6.55)) yields slightly smaller values for t_{Red} and t_{Ox}. Thus, the final drop in the CO concentration at $t > 10\,\mathrm{h}$ seen in Fig. 6.11 disappears. The optimal values for the two performance indicators are severely limited to $X_{\mathrm{OSM}} = 62.4\%$ and $\bar{x}_{\mathrm{CO}} = 0.429$ for the fluidized bed reactor design, respectively. This is due to two reasons: 1) the slower kinetics of reduction compared to oxidation 2) fixed gas flow velocity due to fluidization constraints limiting the degrees of freedom for process control compared to the fixed bed reactor design. Solutions where $t_{\mathrm{Red}} = t_{\mathrm{Ox}}$ are generally

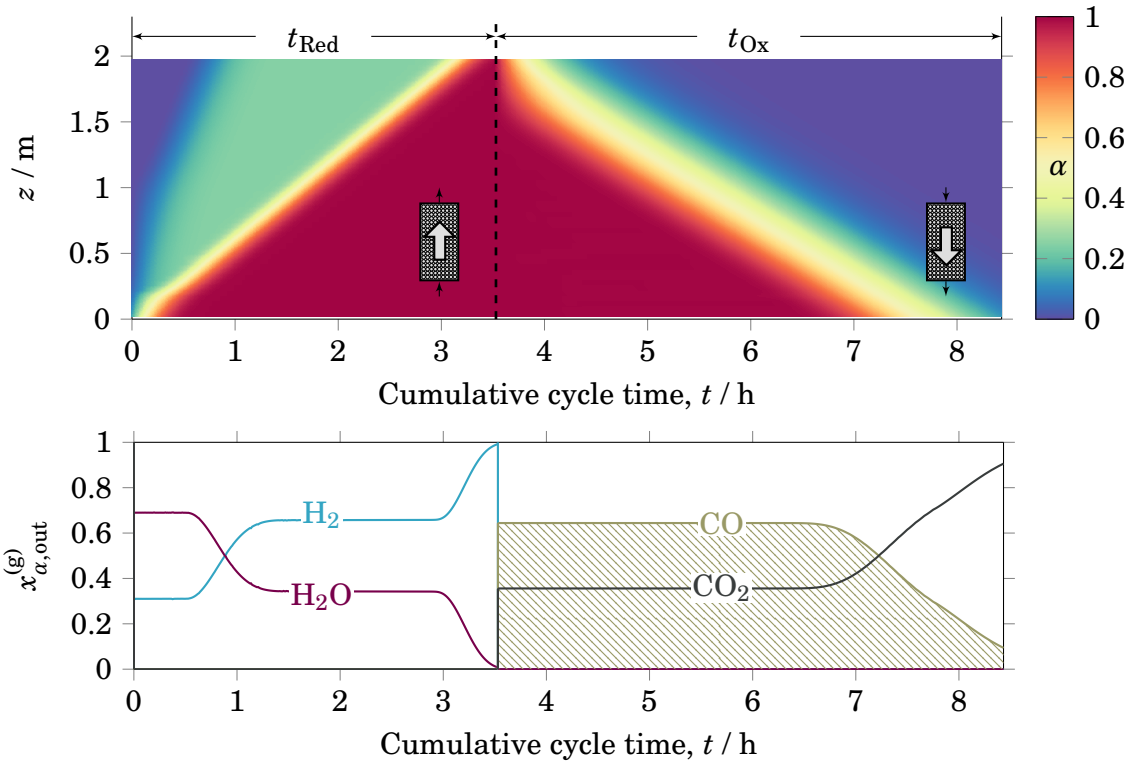

Fig. 6.9 Reduction extent α for the fixed bed reactor design for $v^{(g)}_{Red} = 2.04\,m/s$, $v^{(g)}_{Ox} = 1.07\,m/s$, $t_{Red} = 3.53\,h$ and $t_{Ox} = 4.90\,h$ (optimization results for eq. (6.52)) as a function of time and axial coordinate z (top) and gas outlet concentration $x^{(g)}_{\alpha,out}$ as a function of time (bottom). Maximum OSM utilization is $X_{OSM} = 98.6\%$ with an average CO concentration of $\bar{x}_{CO} = 0.55$.

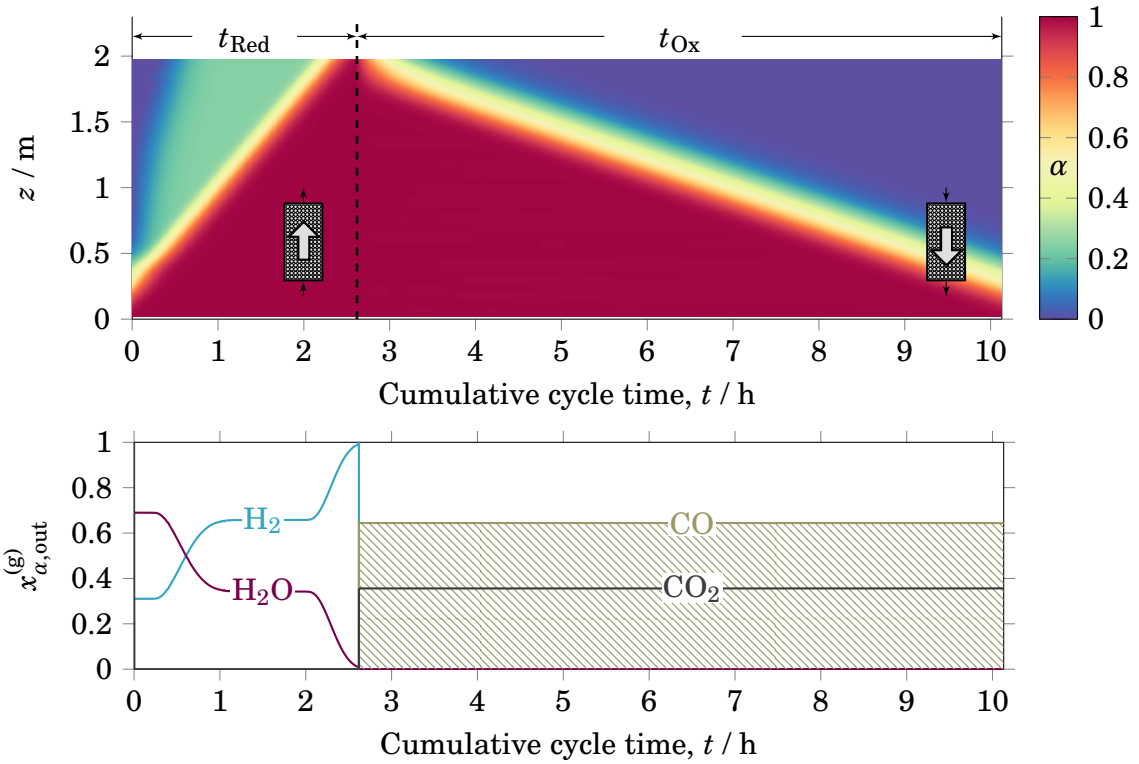

Fig. 6.10 Reduction extent α for the fixed bed reactor design for $v^{(g)}_{Red} = 2.44\,m/s$, $v^{(g)}_{Ox} = 0.51\,m/s$, $t_{Red} = 2.62\,h$ and $t_{Ox} = 7.51\,h$ (optimization results for eq. (6.53)) as a function of time and axial coordinate z (top) and gas outlet concentration $x^{(g)}_{\alpha,out}$ as a function of time (bottom). The maximum achievable average CO concentration is $\bar{x}_{CO} = 0.64$ with an OSM utilization of $X_{OSM} = 83.9\%$.

superior to solutions where $t_{\mathrm{Red}} < t_{\mathrm{Ox}}$, since a shorter reduction period time compared to the oxidation period time decreases the OSM utilization leading to a lower average CO concentration. Solutions with $t_{\mathrm{Red}} > t_{\mathrm{Ox}}$ would theoretically yield better results but are prohibited because in this work only two reactors are allowed. The results in Fig. 6.11 show that during reduction, the maximum mole fraction of Fe is only $x_{\mathrm{Fe}}^{(\mathrm{s})} \approx 0.5$. However, during oxidation the reaction step from Fe to FeO (see eq. (6.6)) yields the highest possible CO concentration in the gas outlet. This favorable reaction step from Fe to FeO can not be completely used under the constraints of the fluidized bed. Therefore, the average CO concentration and the OSM utilization are strongly decreased in the fluidized bed reactor case compared to the fixed bed reactor case. For higher values for $\bar{x}_{\mathrm{CO}}$ and X_{OSM}, a different OSM with more favorable kinetics or more than two reactors would be required.

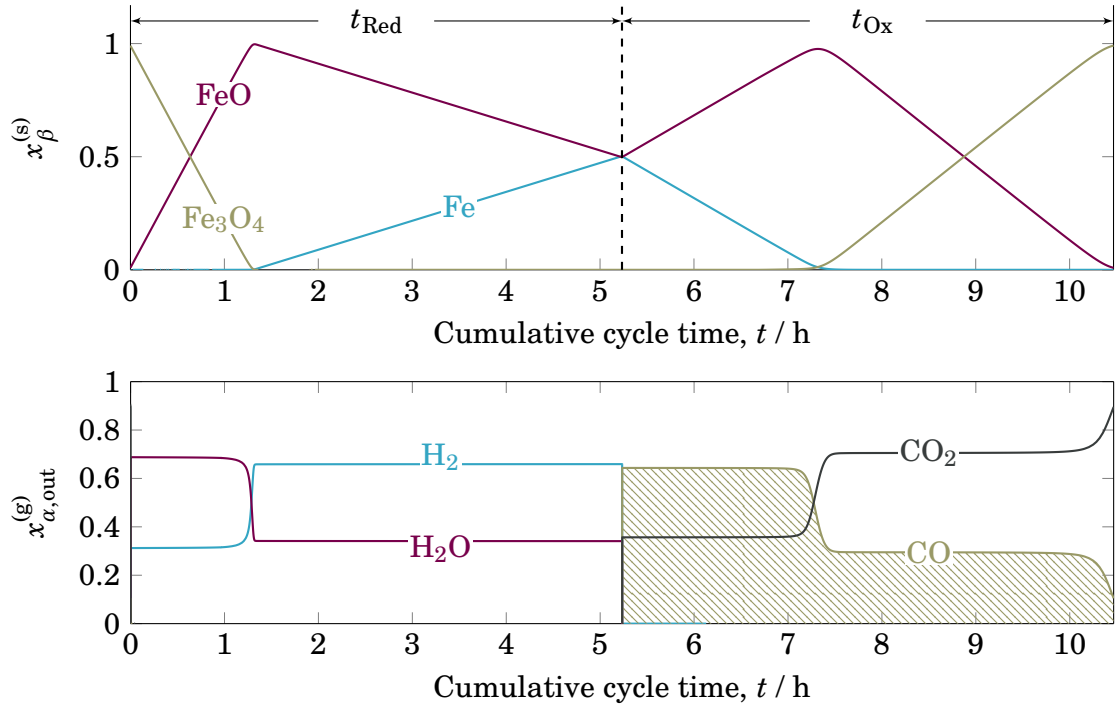

Fig. 6.11 Solid composition $x_\beta^{(\mathrm{s})}$ for the fluidized bed reactor design for $v_{\mathrm{Red}}^{(\mathrm{g})} = v_{\mathrm{Ox}}^{(\mathrm{g})} = 0.6\,\mathrm{m/s}$ and $t_{\mathrm{Red}} = t_{\mathrm{Ox}} = 5.23\,\mathrm{h}$ (optimization results for eq. (6.54)) as a function of time (top) and gas outlet concentration $x_{\alpha,\mathrm{out}}^{(\mathrm{g})}$ as a function of time (bottom). OSM utilization is $X_{\mathrm{OSM}} = 43.6\%$ with an average CO concentration of $\bar{x}_{\mathrm{CO}} = 0.36$.

The optimal results of problems (6.52) to (6.55) are summarized in Table 6.1. The gas conversions of H_2 during reduction (X_{H_2}) and of CO_2 during oxidation (X_{CO_2}) are given in addition to the performance criteria. Theoretically, a total amount of 25.6 kmol of CO_2 could be converted stoichiometrically with the given amount of OSM.

The gas conversion of CO_2 is higher but the H_2 conversion is lower in the fixed bed reactor compared to the fluidized bed reactor. The total molar flow of CO for each case is calculated using the following equation

$$\dot{N}_{CO} = \frac{4}{3} \frac{m_{OSM} X_{OSM}}{M^{(s)} t_{Ox}}, \tag{6.56}$$

where m_{OSM} is the total amount of material in the reactor (2059.1 kg). It can be seen that the fixed bed reactor with maximum OSM utilization produces 8.25 $\mathrm{kmol_{CO}}$/h which is almost twice as much as the alternatives.

Table 6.1 Summary of process parameters and performance criteria for the fixed and fluidized bed reactor design optimization cases defined by equations (6.52) to (6.55). In both cases, $v^{(g)}$ denotes the respective superficial gas velocity. The total amount of material in the reactor is 2059.1 kg in both cases. The conversion of H_2 during the reduction stage and of CO_2 during the oxidation stage are denoted by X_{H_2} and X_{CO_2}, respectively.

		Fixed Bed max X_{OSM}	Fixed Bed max $\bar{x}_{CO}$	Fluidized Bed max X_{OSM}	Fluidized Bed max $\bar{x}_{CO}$
t_{Red}	[h]	3.53	2.62	5.23	4.42
t_{Ox}	[h]	4.90	7.51	5.23	4.42
$v^{(g)}_{Red}$	[m/s]	2.04	2.44	0.60	0.60
$v^{(g)}_{Ox}$	[m/s]	1.07	0.51	0.60	0.60
X_{OSM}	[−]	0.986	0.839	0.624	0.531
$\bar{x}_{CO}$	[−]	0.547	0.644	0.426	0.429
X_{H_2}	[−]	0.400	0.384	0.423	0.426
X_{CO_2}	[−]	0.547	0.644	0.423	0.426
$\dot{N}_{CO}$	[kmol/h]	8.25	4.58	4.89	4.92

Fig. 6.12 shows the Pareto plot for the fixed and fluidized bed reactor designs with regard to the average CO concentration and the OSM utilization. The circles indicate the solution which maximizes one of the two objectives (discussed previously). As illustrated in Fig. 6.12 the fixed bed reactor design is strictly superior to the fluidized bed reactor design with regard to both performance indicators. The maximum average CO concentration is limited by thermodynamics to 0.644 and the OSM utilization cannot be increased above 0.986 without violating the optimization constraints. The Pareto optimal front for the fluidized bed reactor design is small and nearly insensitive to changes in the OSM utilization, i.e. for all solutions, the average CO concentration is nearly the same. The solution of the optimization problems defined by

equations (6.54) and (6.55) lie close to each other on the Pareto front. The Pareto plot illustrates that the performance of the fluidized bed reactor design is severely limited if only two reactors are available with the investigated OSM. The fixed bed reactor allows for greater operational freedom with the control of the gas flows and therefore yields higher values for both performance indicators. However, in this work practical challenges of operation like excessive material deactivation by sintering as well as elutration and attrition are not discussed.

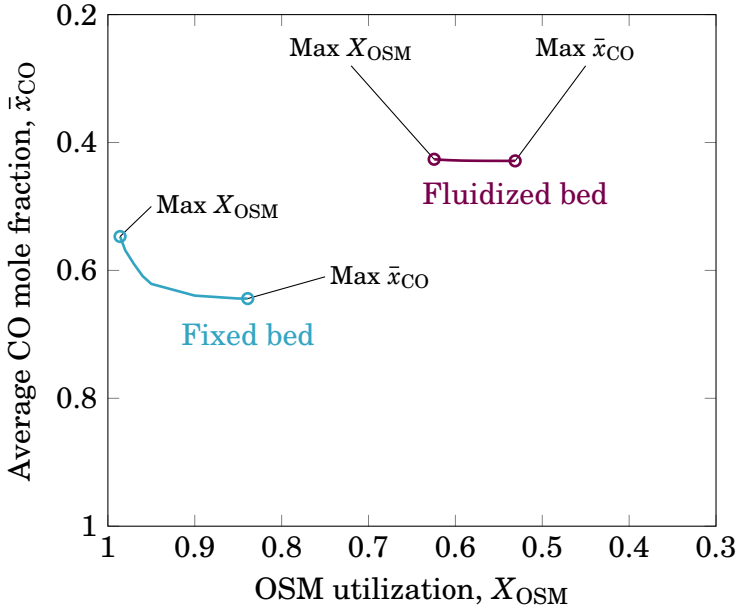

Fig. 6.12 Pareto plot of the optimal solutions for the average CO concentration and OSM utilization for the fixed bed (blue) and fluidized bed (red) reactor designs. Circles indicate the solution, which maximizes one of the two objectives.

6.3 Conclusions

The RWGSCL process was mathematically described using dynamic, one dimensional models for fixed bed and fluidized bed reactor configurations assuming only two reactors each for quasi-continuous production of CO. It was shown for the fixed bed reactor that under equivalent inlet gas concentrations the reduction is slower in an equilibrium limited reaction regime and faster in a rate limited reaction regime compared to the oxidation. The equilibrium limited reaction regime was shown to be advantageous during oxidation in the fixed bed reactor case, since high CO concentrations can be reached when distinct reaction fronts are present. This result was analyzed

in detail in a subsequent optimization of the process. Therefore, two performance indicators were defined, the OSM utilization and the average CO concentration. The optimization results were compared in a Pareto plot. The fixed bed reactor configuration yielded better results for both performance indicators compared to the fluidized bed reactor configuration. The performance of the fluidized bed reactor design was severely limited because the gas flow velocities were fixed by the hydrodynamics and, therefore, less control variables were available for optimization. The maximum performance potential of chemical looping systems in general strongly depends on the dynamics of the system. If the regeneration stage is limiting, higher degrees of operational freedom are needed to achieve high performance. Thus, material design and selection for chemical looping processes should consider that it is important that the regeneration stage of the cycle should ideally be faster than the production stage. The insights gained from this detailed analysis are applicable to comparable chemical looping systems.

7 | Conclusions and outlook

Perfection is achieved not when there is nothing left to add, but when there is nothing left to take away.

Antoine de Saint-Exupéry

While there are many aspects of the process that were investigated and analyzed in this thesis, just as many open questions remain to be answered. This last chapter concludes the work and puts the findings of this thesis into the larger scope of sustainability.

7.1 Concluding remarks

RWGSCL for CO_2 utilization is a novel process in which the concept of chemical looping is applied to the RWGS reaction resulting in a two-step, quasi-continuous process with inherent product separation. In that way, RWGSCL is an intensified version of the conventional RWGS reaction that avoids side reactions and potentially simplifies product separation. The RWGS reaction itself is interesting within the scope of sustainability because it enables the production of syngas from CO_2. Substituting fossil feedstocks for CO_2 to produce syngas is a critical step towards closing the carbon loop and for achieving a stable level of CO_2 in the atmosphere.

In Chapter 3 it is shown how thermodynamic principles can be used to evaluate potential candidate materials for RWGSCL. More specifically, it is argued why there is no material that allows for complete conversion in both process steps (oxidation and reduction) under isothermal conditions. The underlying RWGS reaction brings with it thermodynamic limitations that can not be overcome by applying the chemical looping

concept alone. However, thermodynamic methods still provide valuable information about which material is most suitable from a thermodynamic perspective.

A sustainable syngas production scenario based on CO_2, H_2 and renewable energy is illustrated in Chapter 4. Realistic process efficiencies were applied to all process units to estimate the overall energy efficiency of converting solar energy into syngas. The solar-to-syngas efficiency was estimated to be up to 13.7% for RWGSCL which is comparable to the estimated efficiency of the main competing process, STL. Furthermore, it was shown that the energy consumption of RWGSCL is up to 54% lower compared to the RWGS reaction (in the reactor/separator sequence). The best results were obtained for the production of pure CO. The advantage of RWGSCL over the conventional RWGS reaction decreases when the desired H_2/CO ratio is increased. It was the first quantitative study regarding the energy efficiency of the RWGSCL process.

Once it was concluded that RWGSCL is competitive with regard to energy efficiency the process concept was verified experimentally with the chosen OSM from Chapter 3. The main focus of Chapter 5 was to obtain kinetic information for the oxidation and reduction reactions. Furthermore, the long time stability of the modified iron oxide was assessed. Complete oxidation and reduction from Fe to Fe_3O_4 vice versa was observed for a 500 times cycled material sample.

The obtained kinetic information obtained in Chapter 5 allowed the logical continuation of the work towards process design. In Chapter 6 fixed bed and fluidized bed reactor designs for the RWGSCL process are compared by rigorous process modeling and optimization. The main finding of Chapter 6 was that the fixed bed reactor yields superior performance compared to the fluidized bed reactor because the fixed bed reactor offers more flexible control opportunities. The results show the importance of the interplay between process kinetics and thermodynamic limitations for optimal reactor operation, which has not been investigated before for the RWGSCL process. Another major topic of Chapter 6 was the formulation of thermodynamically consistent reaction rate expressions for the RWGSCL process. Equilibrium-limited gas-solid reactions are a very special case of reactions that require non-standard reaction rate expressions. It was shown how these expressions can be derived. The proposed work flow can be applied to other equilibrium-limited gas-solid reactions as well.

The main achievements of this thesis may be summarized as follows:

- A framework for the rational selection OSMs for RWGSCL based on thermodynamic principles is proposed
- Proof of concept for the RWGSCL process by thermodynamic analysis of the entire production chain from renewables to syngas
- Characterization of iron oxide as OSM by advanced experimental methods
- Kinetic modeling and parameter estimation based on thermogravimetric data
- A new derivation for thermodynamically consistent reaction rate expressions for equilibrium limited gas-solid reactions is proposed
- Dynamic modeling and simulation of fixed and fluidized bed reactor designs for RWGSCL including a comparison with STL

7.2 Outlook and future research areas

The need of technologies that disrupt the prevailing take-make-dispose paradigm to pave the way for a sustainable, circular economy has never been higher and it is growing steadily. However, environmental reasons as discussed in the Chapter 1 are only one side of the coin. Economic drivers are increasingly seen as equally important. In a 2015 report by the consultant firm McKinsey & Company, the economic opportunities of transitioning from a linear to a sustainable, circular economy are highlighted (for Europe) [3]. Whether humankind will shift towards sustainability and how long it will take to get there will arguably depend more on economic incentives than on environmental ones in the foreseeable future.

One of the most important economic driving forces for adoption of CCU processes in the chemical industry is their energy efficiency. In this thesis, the energy efficiency of the RWGSCL process is estimated for a possible future scenario where syngas is produced solely from CO_2, H_2 and solar energy. While the energy efficiency gives some implications about the approximate operating costs of RWGSCL, there is as of yet no detailed cost analysis available that compares the RWGSCL process to the traditional RWGS reaction or STL. This will be another important topic to be investigated in the future not only for RWGSCL but for many other CCU processes as well. Apart from that, there are many other aspects that were not investigated in this thesis due to the restriction of time and space. A selection of aspects that seem worth further investigation is briefly discussed in the following.

First, further research is required to improve the RWGSCL process. The theoretical findings of this thesis must be verified in a pilot plant. Possible deviations from the expected behavior must be thoroughly analyzed and included in the model. Repeated cycling and quasi steady-state operation must be realized on a small scale before larger plants can be designed. The influence of pressure is of particular interest as it was not investigated in this thesis. The main reason is because the reactions are all equimolar and, therefore, the pressure has no influence on the chemical equilbrium. However, the pressure might have a beneficial effect on the reaction rates. In fact, it is known that a pressure increase leads to higher reaction rates in the traditional RWGS reaction [19]. Furthermore, the total throughput must be increased to allow an industrial scale operation. Increasing the material stability to sustain prolonged cycling in an industrial scale reactor is one of the most urgent topics for chemical looping applications in general. Regarding OSM research it would also be interesting to screen more materials to check if there are other suitable OSMs apart from iron oxide. In particular, the influence of dopants on the thermodynamic properties of pure metal oxides must be known to be able to shift the OSM properties in favorable directions (e.g. taylor-made materials based on findings from computational chemistry). In this way, a whole new range of materials could be investigated for the RWGSCL process.

On a broader scale it would be interesting to research alternative ways to overcome the equilibrium limitation in the reduction and oxidation reactions to obtain full conversion. Temperature swings between the reduction and oxidation stage are one possible option but as was argued in Chapter 6 heat recovery is a big problem and a source of large exergy losses. Integrated reactor-separator concepts based on membranes or additional materials that influence the gas composition in a favorable way (e.g. by adsorption and desorption of products) could potentially help to overcome the equilibrium limitations and make the RGWSCL more energy efficient. Unless full conversion is achieved in RWGSCL the maximum potential of the process can not be used because the product gases must still be separated (see Chapter 4) as in the traditional RWGS reaction (even though only two products must be separated in RWGSCL instead of four).

The adoption of RWGSCL (and CCU process in general) in real industrial processes is dependent on several other factors (apart from energy efficiency, material stability, etc.) that go beyond the scope of pure engineering (e.g. economics, politics, etc.) and which can hardly be assessed. Most notably, the dynamic nature of RWGSCL poses a strong barrier for adoption in industry as steady-state operation is preferred

in almost all industrial sectors. After all, the simplicity of the traditional RWGS reaction for CO_2 utilization (heterogeneously catalyzed gas phase reaction that allows for steady-state operation) may outweigh the potential benefits of the RWGSCL concept in an industrial setting.

The upcoming decades will be critical for the transition from a linear to a circular economy. It will be interesting to see whether RWGSCL or (any other chemical looping process) will stand the test of time or if other technologies for CO_2 utilization processes will emerge and prove to be more efficient. However, as long as our whole economy is based on carbon, closing the carbon loop is of paramount importance for a sustainable future. Within this grand challenge, RWGSCL may be one of many processes that help to achieve this goal.

A | Appendix

A.1 Minimum conversion for OSM selection

The chemical equations in Figures Fig. 3.5 and Fig. 3.4 can be generalized as follows:

$$\text{Reduction:} \qquad \mathrm{Me_yO_x} + \mathrm{H_2} \rightleftharpoons \mathrm{Me_yO_{x-1}} + \mathrm{H_2O} \tag{A.1}$$

$$\text{Oxidation:} \qquad \mathrm{Me_yO_{x-1}} + \mathrm{CO_2} \rightleftharpoons \mathrm{Me_yO_x} + \mathrm{CO} \tag{A.2}$$

In that way, the stoichiometric numbers of the gas phase components are always one. Therefore, the equilibrium constant for the reduction reaction (eq. (A.1)) can be written as

$$K_{\mathrm{eq}} = \frac{x_{\mathrm{H_2O}}}{x_{\mathrm{H_2}}}. \tag{A.3}$$

Since only H_2 and H_2O are present during OSM reduction it follows that $x_{\mathrm{H_2}} = 1 - x_{\mathrm{H_2O}}$. Thus, equation A.3 can be reformulated to

$$K_{\mathrm{eq}} = \frac{x_{\mathrm{H_2O}}}{1 - x_{\mathrm{H_2O}}}. \tag{A.4}$$

Assuming that pure H_2 is present at the start of the reaction ($n_{\mathrm{H_2}}(t=0) = 1$), the H_2 equilibrium conversion ($X_{\mathrm{H_2}}$) can be calculated by

$$X_{\mathrm{H_2}} = 1 - \frac{n_{\mathrm{H_2}}(t=\infty)}{n_{\mathrm{H_2}}(t=0)} = 1 - \frac{x_{\mathrm{H_2}}(t=\infty)}{x_{\mathrm{H_2}}(t=0)} = 1 - x_{\mathrm{H_2}}(t=\infty) = x_{\mathrm{H_2O}} \tag{A.5}$$

Therefore, the equilibrium constant is related to X_{H_2} by

$$K_{eq} = \frac{X_{H_2}}{1 - X_{H_2}}. \tag{A.6}$$

Inserting the general definition of the equilibrium constant yields

$$\exp\left(\frac{-\Delta_R g}{RT}\right) = \frac{X_{H_2}}{1 - X_{H_2}}. \tag{A.7}$$

To achieve a minimum value for $X_{H_2,min}$ at any temperature T the Gibbs free energy of reaction must be smaller than a maximum value ($\Delta_R g_{max}$) which is found by rearranging equation (A.7):

$$\Delta_R g_{max} = -\ln\left(\frac{X_{H_2,min}}{1 - X_{H_2,min}}\right) RT. \tag{A.8}$$

Thus, for all values below $\Delta_R g_{max}$ a minimum H_2 equilibrium conversion is ensured (shaded area in Fig. 3.5). Similarly $\Delta_R g_{max}$ can be calculated for the oxidation reaction (eq. (A.2)) to yield the shaded area in Fig. 3.4.

A.2 TGA model for parameter estimation

A.2.1 Balance equations

For the ease of modeling, equations (5.2) and (5.1) were normalized so that the oxidized state of iron oxide has one iron atom. Thus, the considered reactions for oxidation and reduction are given by equations (A.9) and (A.10), respectively.

Oxidation: $$Fe + 4/3\,CO_2 \rightleftharpoons FeO_{4/3} + 4/3\,CO \tag{A.9}$$

Reduction: $$FeO_{4/3} + 4/3\,H_2 \rightleftharpoons Fe + 4/3\,H_2O \tag{A.10}$$

The mole balances used to describe the TG unit are given in terms of mole fractions for the gas ($x_\alpha^{(g)}$) and solid phase ($x_\beta^{(s)}$) according to equations (A.11) and (A.12).

$$\frac{\mathrm{d}x_\alpha^{(g)}}{\mathrm{d}t} = \frac{\dot{F}}{V_{TG}}\left(x_{\alpha,in}^{(g)} - x_\alpha^{(g)}\right) + \frac{m_{OSM}}{c_t^{(g)} V_{TG}} \nu_{\alpha,k} r_k \qquad \forall \alpha = \{CO, CO_2, H_2, H_2O\} \tag{A.11}$$

$$\frac{\mathrm{d}x_\beta^{(s)}}{\mathrm{d}t} = M_{OSM} \nu_{\beta,k} r_k \qquad \forall \beta = \{Fe, FeO_{4/3}\} \tag{A.12}$$

Here, index k = {Ox,Red} for oxidation (eq. (A.9)) and reduction (eq. (A.10)), respectively. $\dot{F}$ is the total gas flow rate, which was 120 ml/min for all experiments and V_{TG} is the volume of the thermogravimetry unit (38 ml). The mole fractions of the inlet gas stream are denoted by $x_{\alpha,in}^{(g)}$. The total gas concentration, $c_t^{(g)}$, is calculated from the ideal gas law according to

$$c_t^{(g)} = \frac{p}{RT}, \tag{A.13}$$

where R is the universal gas constant and p and T are the system pressure and temperature, respectively. Since the process is operated at high temperature and ambient pressure, the use of the ideal gas law is justified. The mass m_{OSM} and the molar mass M_{OSM} of the OSM at each point in time can be calculated by equations (A.14) and (A.15).

$$m_{OSM} = w_{Fe}^{(s)} m_{Fe} + w_{FeO_{4/3}}^{(s)} m_{FeO_{4/3}} \tag{A.14}$$

$$M_{OSM} = x_{Fe}^{(s)} M_{Fe} + x_{FeO_{4/3}}^{(s)} M_{FeO_{4/3}} \tag{A.15}$$

Here, w denotes the mass fraction, which can be calculated from the mole according to

$$w_\beta^{(s)} = \frac{x_\beta^{(s)} M_\beta^{(s)}}{\sum_\beta x_\beta^{(s)} M_\beta^{(s)}} \qquad \forall \beta = \{Fe, FeO_{4/3}\}. \tag{A.16}$$

A.2.2 Kinetics

The reaction rates for oxidation and reduction are described by the following equations, respectively

$$r_{\mathrm{Ox}} = k_{\mathrm{Ox}} f(\xi_{\mathrm{Ox}}) x_{\mathrm{CO_2}}^{m_{\mathrm{Ox}}} \tag{A.17}$$

$$r_{\mathrm{Red}} = k_{\mathrm{Red}} f(\xi_{\mathrm{Red}}) x_{\mathrm{H_2}}^{m_{\mathrm{Red}}}, \tag{A.18}$$

where k_{Ox} and k_{Red} are the kinetic constants for the oxidation and reduction reaction, respectively. Their temperature dependency is described by the Arrhenius equation:

$$k = k^0 \exp\left(-\frac{E_A}{RT}\right) \tag{A.19}$$

The function $f(\xi)$ for the reaction extent of oxidation and reduction is depending on the reaction model used (see Table 5.1). The reaction extents for oxidation (ξ_{Ox}) and reduction (ξ_{Red}) are equal to $1 - x_{\mathrm{FeO_{4/3}}}$ and $1 - x_{\mathrm{Fe}}$, respectively. The influence of the reactive gas mole fraction is described by $x_{\mathrm{CO_2}}^{m_{\mathrm{Ox}}}$ and $x_{\mathrm{H_2}}^{m_{\mathrm{Red}}}$. The reaction rates are, therefore, functions of the temperature T, the reaction extent ξ, and the reactive gas mole fractions $x_{\mathrm{H_2}}$ and $x_{\mathrm{CO_2}}$.

A.3 Fixed bed model derivation

Gas Phase

Starting point for the model derivation is the local partial mass balance in one spatial dimension for the gas phase (G)

$$\frac{\partial \rho_\alpha^{(\mathrm{g})}}{\partial t} = -\frac{\partial}{\partial z}\left(\rho_\alpha^{(\mathrm{g})} v^{(\mathrm{g})} + j_\alpha^{(\mathrm{g})}\right) + \sigma_\alpha^M \qquad \forall \alpha = \{\mathrm{H_2}, \mathrm{H_2O}, \mathrm{CO}, \mathrm{CO_2}\}, \tag{A.20}$$

where $\rho_\alpha^{(g)}$ is the local mass density of component α ($\left[\rho_\alpha^{(g)}\right] = \mathrm{kg/m^3_{Reactor}}$), $v^{(g)}$ the gas phase superficial velocity, $j_\alpha^{(g)}$ the diffusive flux and σ_α^M the specific source term ($\left[\sigma_\alpha^M\right] = \mathrm{kg/m^3/s}$). Assuming that diffusion can be neglected because of high gas velocity, eq. (A.20) reduces to

$$\frac{\partial \rho_\alpha^{(g)}}{\partial t} = -\frac{\partial}{\partial z}\left(\rho_\alpha^{(g)} v^{(g)}\right) + \sigma_\alpha^M. \tag{A.21}$$

The gas phase velocity $v^{(g)}$ can be calculated starting from the local total mass balance of the gas phase

$$\frac{\partial \rho^{(g)}}{\partial t} = -\frac{\partial}{\partial z}\left(\rho^{(g)} v^{(g)}\right) \tag{A.22}$$

by introducing the ideal gas law and assuming isothermal and isobaric operation of the reactor. In this case, the local total mass density of the gas, $\rho^{(g)}$, is constant and eq. (A.22) reduces to

$$0 = \frac{\partial v^{(g)}}{\partial z}, \tag{A.23}$$

i.e. $v^{(g)}$ is constant throughout the reactor. The superficial gas phase velocity $v^{(g)}$ and the void fraction ε can be used to calculate the interstitial gas phase velocity $v_{\mathrm{int}}^{(g)}$ (velocity in the gas void volume) by

$$v_{\mathrm{int}}^{(g)} = \frac{v^{(g)}}{\varepsilon}. \tag{A.24}$$

With $\rho_\alpha^{(g)} = c_{\mathrm{t}}^{(g)} M_\alpha x_\alpha^{(g)} \varepsilon$, eq. (A.21) can be rewritten as

$$\frac{\partial}{\partial t}\left(c_{\mathrm{t}}^{(g)} M_\alpha x_\alpha^{(g)} \varepsilon\right) = -\frac{\partial}{\partial z}\left(c_{\mathrm{t}}^{(g)} M_\alpha x_\alpha^{(g)} \varepsilon v_{\mathrm{int}}^{(g)}\right) + \sigma_\alpha^M = -\frac{\partial}{\partial z}\left(c_{\mathrm{t}}^{(g)} M_\alpha x_\alpha^{(g)} v^{(g)}\right) + \sigma_\alpha^M, \tag{A.25}$$

where $c_{\mathrm{t}}^{(\mathrm{g})}$ is the molar concentration of the gas phase, M_α the molar mass of component α, $x_\alpha^{(\mathrm{g})}$ the gas phase mole fraction of component α and ε the fixed bed void fraction ($[\varepsilon] = \mathrm{m}^3_{\mathrm{Gas}}/\mathrm{m}^3_{\mathrm{Reactor}}$). Here, $c_{\mathrm{t}}^{(\mathrm{g})}$, M_α and ϵ are constant. Furthermore, the specific source term σ_α^M for the gas phase is defined as

$$\sigma_\alpha^M = M_\alpha \sum_j^{N_R} \nu_{\alpha,j} r_{j,\mathrm{eff}}. \tag{A.26}$$

Eq. (A.25) and (A.26) can be rearranged to yield

$$\frac{\partial x_\alpha^{(\mathrm{g})}}{\partial t} = -\frac{v^{(\mathrm{g})}}{\varepsilon}\frac{\partial x_\alpha^{(\mathrm{g})}}{\partial z} + \frac{1}{\varepsilon c_{\mathrm{t}}^{(\mathrm{g})}} \sum_j^{N_R} \nu_{\alpha,j} r_{j,\mathrm{eff}}. \tag{A.27}$$

Here, $\nu_{\alpha,j}$ is the stoichiometric coefficient of component α in reaction j and $r_{j,\mathrm{eff}}$ is the corresponding effective reaction rate. N_R denotes the total number of reactions considered. For gas-solid reactions, the reaction rate is often expressed in terms of mol/kg/s. However, in eq. (A.27) the reaction rate is given as $\left[r_{j,\mathrm{eff}}\right] = \mathrm{mol/m^3/s}$. To convert between the rate expressions, the solid phase density $\rho^{(\mathrm{s})}$ and the fixed bed void fraction can be used according to

$$r_{j,\mathrm{eff}} = (1-\varepsilon)\rho^{(\mathrm{s})} r_{j,\mathrm{eff}}^M. \tag{A.28}$$

Here $r_{j,\mathrm{eff}}^M$ denotes the reaction rate in terms of mol/kg/s. The effective reaction rate $r_{j,\mathrm{eff}}^M$ is related to the intrinsic reaction rate r_j^M by the effectiveness factor η_{eff}:

$$r_{j,\mathrm{eff}}^M = \eta_{\mathrm{eff}} r_j^M \tag{A.29}$$

The effectiveness factor is introduced to account for mass transfer resistances in the pores of the oxygen storage material and the resulting decrease in reactivity. Combining equations (A.28) and (A.29) with eq. (A.27) yields the final balance in form of the gas mole fractions:

$$\frac{\partial x_\alpha^{(\mathrm{g})}}{\partial t} = -\frac{v^{(\mathrm{g})}}{\varepsilon}\frac{\partial x_\alpha^{(\mathrm{g})}}{\partial z} + \frac{(1-\varepsilon)}{\varepsilon}\frac{\rho^{(\mathrm{s})}}{c_{\mathrm{t}}^{(\mathrm{g})}}\eta_{\mathrm{eff}} \sum_j^{N_R} \nu_{\alpha,j} r_j^M \qquad \forall \alpha = \{\mathrm{H_2}, \mathrm{H_2O}, \mathrm{CO}, \mathrm{CO_2}\} \tag{A.30}$$

Solid phase

The derivation of the model equation for the solid phase (S) is analogous to the gas phase. The local partial mass balance in one spatial dimension for the solid phase (S) reads

$$\frac{\partial \rho_\beta^{(\mathrm{s})}}{\partial t} = -\frac{\partial}{\partial z}\left(\rho_\beta^{(\mathrm{s})} v^{(\mathrm{s})} + j_\beta^{(\mathrm{s})}\right) + \sigma_\beta^M \qquad \forall \beta = \{\mathrm{Fe}, \mathrm{FeO}, \mathrm{FeO_{4/3}}\}. \tag{A.31}$$

Since the solid phase is a fixed bed it follows that $v^{(\mathrm{s})} = 0$. Assuming that diffusion can be neglected in the solid phase, eq. (A.31) reduces to

$$\frac{\partial \rho_\beta^{(\mathrm{s})}}{\partial t} = \sigma_\beta^M. \tag{A.32}$$

With $\rho_\beta^{(\mathrm{s})} = c_\mathrm{t}^{(\mathrm{s})} M_\beta x_\beta^{(\mathrm{s})}(1-\varepsilon)$, eq. (A.32) can be rewritten as

$$\frac{\partial}{\partial t}\left(c_\mathrm{t}^{(\mathrm{s})} M_\beta x_\beta^{(\mathrm{s})}(1-\varepsilon)\right) = \sigma_\beta^M, \tag{A.33}$$

where $c_\mathrm{t}^{(\mathrm{s})}$, M_β and ε are constant. The specific source term σ_β^M for the solid phase is defined as

$$\sigma_\beta^M = M_\beta \sum_j^{N_R} \nu_{\beta,j} r_{j,\mathrm{eff}}. \tag{A.34}$$

Introducing eqs. (A.28) and (A.29) and rearranging leads to the final balance in form of the solid mole fractions:

$$\begin{aligned} \frac{\partial x_\beta^{(\mathrm{s})}}{\partial t} &= \frac{(1-\varepsilon)\rho^{(\mathrm{s})}}{(1-\varepsilon)c_\mathrm{t}^{(\mathrm{s})}} \eta_\mathrm{eff} \sum_j^{N_R} \nu_{\beta,j} r_j^M = M^{(\mathrm{s})} \eta_\mathrm{eff} \sum_j^{N_R} \nu_{\beta,j} r_j^M \\ &\forall \beta = \{\mathrm{Fe}, \mathrm{FeO}, \mathrm{FeO_{4/3}}\} \end{aligned} \tag{A.35}$$

Model discretization

The finite volume method (FVM) was used to discretize the derived model equations spatially to yield a coupled ODE system, which was solved in MATLAB (*ode15s*). Piecewise constant functions were assumed for the system variables $x_\alpha^{(\mathrm{g})}$ and $x_\beta^{(\mathrm{s})}$ and

an upwind scheme was used because of the defined flow direction. The inlet condition for $x_\alpha^{(g)}$ is used as a boundary condition:

$$x_\alpha^{(g)}\Big|_{z=0} = x_{\alpha,\text{in}}^{(g)} \tag{A.36}$$

The discretization scheme with equidistant spacing of the finite volumes is illustrated in Fig. A.1. The following ODE system is derived:

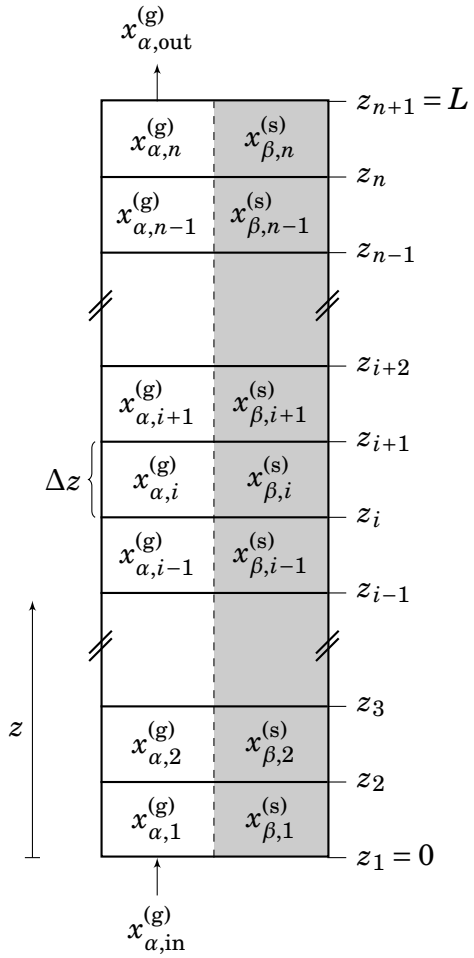

Fig. A.1 Discretization scheme for the fixed bed reactor model with equidistant spacing. Gas phase depicted in white and solid phase in gray.

$$\frac{\mathrm{d}x_{\alpha,1}^{(\mathrm{g})}}{\mathrm{d}t} = -\frac{v^{(\mathrm{g})}}{\varepsilon \Delta z}\left(x_{\alpha,1}^{(\mathrm{g})} - x_{\alpha,\mathrm{in}}^{(\mathrm{g})}\right) + \frac{(1-\varepsilon)}{\varepsilon}\frac{\rho^{(\mathrm{s})}}{c_{\mathrm{t}}^{(\mathrm{g})}}\eta_{\mathrm{eff}}\sum_{j}^{N_R}\nu_{\alpha,j}r_j^M(x_{\alpha,1}^{(\mathrm{g})}, x_{\beta,1}^{(\mathrm{s})}) \tag{A.37}$$

$$\frac{\mathrm{d}x_{\alpha,i}^{(\mathrm{g})}}{\mathrm{d}t} = -\frac{v^{(\mathrm{g})}}{\varepsilon \Delta z}\left(x_{\alpha,i}^{(\mathrm{g})} - x_{\alpha,i-1}^{(\mathrm{g})}\right) + \frac{(1-\varepsilon)}{\varepsilon}\frac{\rho^{(\mathrm{s})}}{c_{\mathrm{t}}^{(\mathrm{g})}}\eta_{\mathrm{eff}}\sum_{j}^{N_R}\nu_{\alpha,j}r_j^M(x_{\alpha,i}^{(\mathrm{g})}, x_{\beta,i}^{(\mathrm{s})}) \quad \forall i = 2\ldots N_{FV} \tag{A.38}$$

$$\frac{\mathrm{d}x_{\beta,i}^{(\mathrm{s})}}{\mathrm{d}t} = M^{(\mathrm{s})}\eta_{\mathrm{eff}}\sum_{j}^{N_R}\nu_{\beta,j}r_j^M(x_{\alpha,i}^{(\mathrm{g})}, x_{\beta,i}^{(\mathrm{s})}) \quad \forall i = 1\ldots N_{FV} \tag{A.39}$$

Here, i indicates the number of finite volumes ranging from 1 to N_{FV}. In this work, 50 finite elements were used for simulation and optimization. This number was found to be most efficient while granting accurate results.

A.4 Two-region fluidized bed model derivation

Bubble Region

The local partial mass balance in one spatial dimension for the gas phase in the bubble region (b) can be stated as follows:

$$\frac{\partial \rho_\alpha^{(\mathrm{b})}}{\partial t} = -\frac{\partial}{\partial z}\left(\rho_\alpha^{(\mathrm{b})} v^{(\mathrm{b})} + j_\alpha^{(\mathrm{b})}\right) + \sigma_\alpha^M \qquad \forall \alpha = \{\mathrm{H_2}, \mathrm{H_2O}, \mathrm{CO}, \mathrm{CO_2}\}, \tag{A.40}$$

where $\rho_\alpha^{(\mathrm{b})}$ is the local mass density of component α ($\left[\rho_\alpha^{(\mathrm{b})}\right] = \mathrm{kg/m^3_{Reactor}}$), $v^{(\mathrm{b})}$ the rise velocity of bubble gas, $j_\alpha^{(\mathrm{b})}$ the diffusive flux and σ_α^M the specific source term ($\left[\sigma_\alpha^M\right] = \mathrm{kg/m^3/s}$). Assuming that diffusion can be neglected because of high gas velocity and that no reaction occurs in the bubble region, eq. (A.40) reduces to

$$\frac{\partial \rho_\alpha^{(\mathrm{b})}}{\partial t} = -\frac{\partial}{\partial z}\left(\rho_\alpha^{(\mathrm{b})} v^{(\mathrm{b})}\right). \tag{A.41}$$

With $\rho_\alpha^{(\mathrm{b})} = c_\alpha^{(\mathrm{b})} M_\alpha \delta$, eq. (A.41) can be rewritten as

$$\frac{\partial}{\partial t}\left(c_\alpha^{(\mathrm{b})} M_\alpha \delta\right) = -\frac{\partial}{\partial z}\left(c_\alpha^{(\mathrm{b})} M_\alpha \delta v^{(\mathrm{b})}\right), \tag{A.42}$$

where $c_{\mathrm{t}}^{(\mathrm{b})}$ is the molar concentration of component α in the gas of the bubble region, M_α the molar mass of component α and δ the bubble fraction ($[\delta] = \mathrm{m}^3_{\mathrm{Bubble}}/\mathrm{m}^3_{\mathrm{Reactor}}$). Here, M_α, δ and $v^{(\mathrm{b})}$ are assumed to be constant. Furthermore, a bubble-emulsion mass interchange term is inserted to describe the mass flow between the two regions:

$$\delta \frac{\partial c_\alpha^{(\mathrm{b})}}{\partial t} = -\delta v^{(\mathrm{b})} \frac{\partial c_\alpha^{(\mathrm{b})}}{\partial z} - \delta K^{(\mathrm{be})} \left(c_\alpha^{(\mathrm{b})} - c_\alpha^{(\mathrm{e})} \right) \tag{A.43}$$

Here, $K^{(\mathrm{be})}$ denotes the bubble-emulsion gas interchange coefficient ($\left[K^{(\mathrm{be})}\right] = 1/\mathrm{s}$) and $c_\alpha^{(\mathrm{e})}$ the molar gas concentration in the emulsion region. It is assumed that the ideal gas law holds, such that the total gas concentration in both regions is equal:

$$c_{\mathrm{t}}^{(\mathrm{b})} = c_{\mathrm{t}}^{(\mathrm{e})} = c_{\mathrm{t}}^{(\mathrm{g})} \tag{A.44}$$

Rearranging yields the final equation in form of the gas phase mole fractions in the bubble region:

$$\frac{\partial x_\alpha^{(\mathrm{b})}}{\partial t} = -v^{(\mathrm{b})} \frac{\partial x_\alpha^{(\mathrm{b})}}{\partial z} - K^{(\mathrm{be})} \left(x_\alpha^{(\mathrm{b})} - x_\alpha^{(\mathrm{e})} \right) \tag{A.45}$$

Emulsion region

Gas phase

For the gas phase in the emulsion region (e), a similar derivation is used starting from the local partial mass balance in one spatial dimension:

$$\frac{\partial \rho_\alpha^{(\mathrm{e})}}{\partial t} = -\frac{\partial}{\partial z} \left(\rho_\alpha^{(\mathrm{e})} v^{(\mathrm{e})} + j_\alpha^{(\mathrm{e})} \right) + \sigma_\alpha^M \qquad \forall \alpha = \{\mathrm{H_2}, \mathrm{H_2O}, \mathrm{CO}, \mathrm{CO_2}\}, \tag{A.46}$$

where $\rho_\alpha^{(\mathrm{e})}$ is the local mass density of component α ($\left[\rho_\alpha^{(\mathrm{e})}\right] = \mathrm{kg/m^3_{Reactor}}$), $v^{(\mathrm{e})}$ the emulsion region gas velocity, $j_\alpha^{(\mathrm{e})}$ the diffusive flux and σ_α^M the specific source term ($\left[\sigma_\alpha^M\right] = \mathrm{kg/m^3/s}$). Assuming that diffusion can be neglected because of high gas velocity, eq. (A.46) reduces to

$$\frac{\partial \rho_\alpha^{(\mathrm{e})}}{\partial t} = -\frac{\partial}{\partial z} \left(\rho_\alpha^{(\mathrm{e})} v^{(\mathrm{e})} \right) + \sigma_\alpha^M. \tag{A.47}$$

With $\rho_\alpha^{(\mathrm{e})} = c_\alpha^{(\mathrm{e})} M_\alpha (1-\delta)\varepsilon_{\mathrm{mf}}$ and eq. (A.26), eq. (A.47) can be rewritten as

$$\frac{\partial}{\partial t}\left(c_\alpha^{(\mathrm{e})} M_\alpha (1-\delta)\varepsilon_{\mathrm{mf}}\right) = -\frac{\partial}{\partial z}\left(c_\alpha^{(\mathrm{e})} M_\alpha (1-\delta)\varepsilon_{\mathrm{mf}} v^{(\mathrm{e})}\right) + M_\alpha \sum_j^{N_R} \nu_{\alpha,j} r_j. \tag{A.48}$$

Here, $\varepsilon_{\mathrm{mf}}$ denotes the minimum fluidization void fraction ($[\varepsilon_{\mathrm{mf}}] = \mathrm{m}^3_{\mathrm{Gas}}/\mathrm{m}^3_{\mathrm{Emulsion}}$). In fluidized bed operation, the effectiveness factor η_{eff} is assumed to be unity, such that $r^M_{j,\mathrm{eff}} = r^M_j$. This assumption is realistic because in fluidized bed reactors the mass and heat transfer resistance is minimized by vigorous mixing and a small particle size [168]. To convert from $\left[r_j\right] = \mathrm{mol/m^3/s}$ to $\left[r^M_j\right] = \mathrm{mol/kg/s}$, the following equation is used:

$$r_j = (1-\delta)(1-\varepsilon_{\mathrm{mf}})\rho^{(\mathrm{s})} r^M_j \tag{A.49}$$

Rearranging eq. (A.48) yields:

$$(1-\delta)\varepsilon_{\mathrm{mf}}\frac{\partial c_\alpha^{(\mathrm{e})}}{\partial t} = -(1-\delta)\varepsilon_{\mathrm{mf}} v^{(\mathrm{e})}\frac{\partial c_\alpha^{(\mathrm{e})}}{\partial z} + (1-\delta)(1-\varepsilon_{\mathrm{mf}})\rho^{(\mathrm{s})}\sum_j^{N_R}\nu_{\alpha,j} r^M_j. \tag{A.50}$$

Again, a bubble-emulsion mass interchange term is inserted to describe the mass flow between the two regions:

$$\begin{aligned}(1-\delta)\varepsilon_{\mathrm{mf}}\frac{\partial c_\alpha^{(\mathrm{e})}}{\partial t} = &-(1-\delta)\varepsilon_{\mathrm{mf}} v^{(\mathrm{e})}\frac{\partial c_\alpha^{(\mathrm{e})}}{\partial z}\ldots \\ &+\delta K^{(\mathrm{be})}\left(c_\alpha^{(\mathrm{b})} - c_\alpha^{(\mathrm{e})}\right) + (1-\delta)(1-\varepsilon_{\mathrm{mf}})\rho^{(\mathrm{s})}\sum_j^{N_R}\nu_{\alpha,j} r^M_j\end{aligned} \tag{A.51}$$

Using eq. (A.44) and rearranging, the final equation in form of the gas phase mole fractions in the emulsion region:

$$\begin{aligned}\frac{\partial x_\alpha^{(\mathrm{e})}}{\partial t} = &- v^{(\mathrm{e})}\frac{\partial x_\alpha^{(\mathrm{e})}}{\partial z} + \frac{\delta}{(1-\delta)\varepsilon_{\mathrm{mf}}} K^{(\mathrm{be})}\left(x_\alpha^{(\mathrm{b})} - x_\alpha^{(\mathrm{e})}\right)\ldots \\ &+ \frac{1-\varepsilon_{\mathrm{mf}}}{\varepsilon_{\mathrm{mf}}}\frac{\rho^{(\mathrm{s})}}{c_{\mathrm{t}}^{(\mathrm{g})}}\sum_j^{N_R}\nu_{\alpha,j} r^M_j\end{aligned} \tag{A.52}$$

Solid phase

For the solid phase in the emulsion region (S), the dispersion model is used according to Kunii and Levenspiel [111] with an additional reaction term:

$$\frac{\partial \rho_\beta^{(\mathrm{s})}}{\partial t} = D_v^{(\mathrm{s})} \frac{\partial^2 \rho_\beta^{(\mathrm{s})}}{\partial z^2} + \sigma_\beta^M \qquad \forall \beta = \{\mathrm{Fe}, \mathrm{FeO}, \mathrm{FeO_{4/3}}\}, \tag{A.53}$$

where $\rho_\beta^{(\mathrm{s})}$ is the local mass density of component β ($\left[\rho_\beta^{(\mathrm{s})}\right] = \mathrm{kg/m^3_{Reactor}}$), $D_v^{(\mathrm{s})}$ the average vertical dispersion coefficient for the solid and σ_β^M the specific source term ($\left[\sigma_\beta^M\right] = \mathrm{kg/m^3/s}$).With $\rho_\beta^{(\mathrm{s})} = c_\mathrm{t}^{(\mathrm{s})} x_\beta^{(\mathrm{s})} M_\beta (1-\varepsilon_\mathrm{mf})(1-\delta)$, eq. (A.53) can be rearranged to

$$\frac{\partial}{\partial t}\left(c_\mathrm{t}^{(\mathrm{s})} x_\beta^{(\mathrm{s})} M_\beta (1-\varepsilon_\mathrm{mf})(1-\delta)\right) = D_v^{(\mathrm{s})} \frac{\partial^2}{\partial z^2}\left(c_\mathrm{t}^{(\mathrm{s})} x_\beta^{(\mathrm{s})} M_\beta (1-\varepsilon_\mathrm{mf})(1-\delta)\right) + \sigma_\beta^M, \tag{A.54}$$

where $c_\mathrm{t}^{(\mathrm{s})}$ is the total concentration of the solid. Eq. (A.34) is introduced to describe the reaction term:

$$\frac{\partial}{\partial t}\left(c_\mathrm{t}^{(\mathrm{s})} x_\beta^{(\mathrm{s})} M_\beta (1-\varepsilon_\mathrm{mf})(1-\delta)\right) = D_v^{(\mathrm{s})} \frac{\partial^2}{\partial z^2}\left(c_\mathrm{t}^{(\mathrm{s})} x_\beta^{(\mathrm{s})} M_\beta (1-\varepsilon_\mathrm{mf})(1-\delta)\right) + M_\beta \sum_j^{N_R} \nu_{\beta,j} r_j. \tag{A.55}$$

To convert from $[r_j] = \mathrm{mol/m^3/s}$ to $\left[r_j^M\right] = \mathrm{mol/kg/s}$, eq. (A.49) is used. Rearranging yields:

$$\frac{\partial x_\beta^{(\mathrm{s})}}{\partial t} = D_v^{(\mathrm{s})} \frac{\partial^2 x_\beta^{(\mathrm{s})}}{\partial z^2} + \frac{\rho^{(\mathrm{s})}}{c_\mathrm{t}^{(\mathrm{s})}} \sum_j^{N_R} \nu_{\beta,j} r_j^M. \tag{A.56}$$

Noting that $\rho^{(\mathrm{s})}/c_\mathrm{t}^{(\mathrm{s})} = M^{(\mathrm{s})}$ yields the final equation in form of the solid phase mole fractions in the emulsion region:

$$\frac{\partial x_\beta^{(\mathrm{s})}}{\partial t} = D_v^{(\mathrm{s})} \frac{\partial^2 x_\beta^{(\mathrm{s})}}{\partial z^2} + M^{(\mathrm{s})} \sum_j^{N_R} \nu_{\beta,j} r_j^M \tag{A.57}$$

Model discretization

The finite volume method (FVM) was used to discretize the derived model equations spatially to yield a coupled ODE system, which was solved in MATLAB (*ode15s*). Piecewise constant functions were assumed for the system variables $x_\alpha^{(\mathrm{b})}$, $x_\alpha^{(\mathrm{e})}$ and $x_\beta^{(\mathrm{s})}$ and an upwind scheme was used because of the defined flow direction. Dispersion was assumed to be limited inside the reactor, such that the following boundary conditions for $x_\beta^{(\mathrm{s})}$ (no axial dispersion at the reactor inlet and outlet) can be formulated:

$$\left.\frac{\partial x_\beta^{(\mathrm{s})}}{\partial z}\right|_{z=0} = 0 \tag{A.58}$$

$$\left.\frac{\partial x_\beta^{(\mathrm{s})}}{\partial z}\right|_{z=L} = 0 \tag{A.59}$$

For $x_\alpha^{(\mathrm{b})}$ and $x_\alpha^{(\mathrm{e})}$ the inlet conditions are used as boundary conditions. The discretization scheme with equidistant spacing of the finite volumes is illustrated in Fig. A.2.

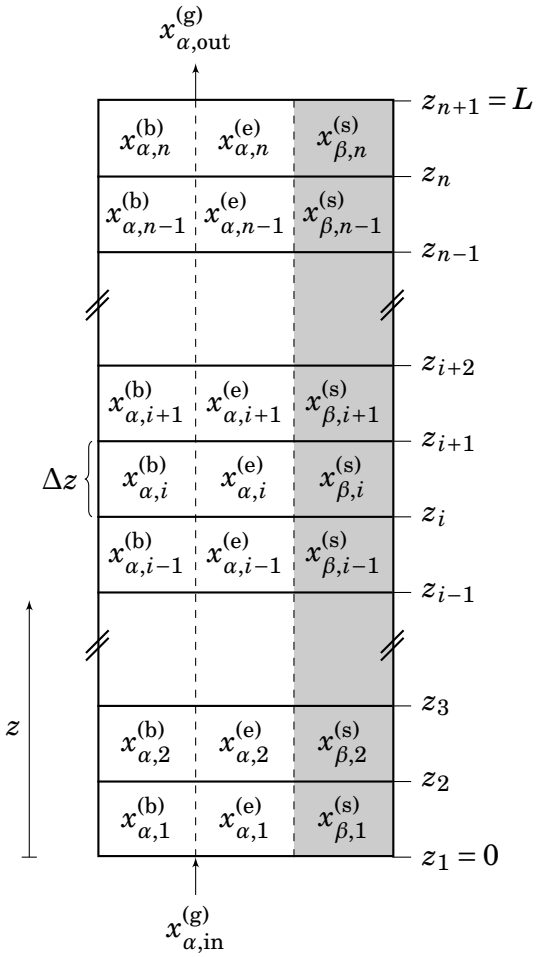

Fig. A.2 Discretization scheme for the two-region fluidized bed reactor model with equidistant spacing. The bubble region is depicted in white and the emulsion region in gray.

The following ODE system is derived:

$$\frac{\mathrm{d}x_{\alpha,1}^{(\mathrm{b})}}{\mathrm{d}t} = -\frac{v^{(\mathrm{b})}}{\Delta z}\left(x_{\alpha,1}^{(\mathrm{b})} - x_{\alpha,\mathrm{in}}^{(\mathrm{g})}\right) - K^{(\mathrm{be})}(x_{\alpha,1}^{(\mathrm{b})} - x_{\alpha,1}^{(\mathrm{e})}) \tag{A.60}$$

$$\frac{\mathrm{d}x_{\alpha,i}^{(\mathrm{b})}}{\mathrm{d}t} = -\frac{v^{(\mathrm{b})}}{\Delta z}\left(x_{\alpha,i}^{(\mathrm{b})} - x_{\alpha,i-1}^{(\mathrm{b})}\right) - K^{(\mathrm{be})}(x_{\alpha,i}^{(\mathrm{b})} - x_{\alpha,i}^{(\mathrm{e})}) \qquad \forall i = 2\ldots N_{FV} \tag{A.61}$$

$$\begin{aligned}\frac{\mathrm{d}x_{\alpha,1}^{(\mathrm{e})}}{\mathrm{d}t} = &-\frac{v^{(\mathrm{e})}}{\Delta z}\left(x_{\alpha,1}^{(\mathrm{e})} - x_{\alpha,\mathrm{in}}^{(\mathrm{g})}\right) + \frac{\delta}{(1-\delta)\varepsilon_{\mathrm{mf}}}K^{(\mathrm{be})}(x_{\alpha,1}^{(\mathrm{b})} - x_{\alpha,1}^{(\mathrm{e})})\ldots \\ &+ \frac{1-\varepsilon_{\mathrm{mf}}}{\varepsilon_{\mathrm{mf}}}\frac{\rho^{(\mathrm{s})}}{c_{\mathrm{t}}^{(\mathrm{g})}}\sum_{j}^{N_R}\nu_{\alpha,j}r_j^M(x_{\alpha,1}^{(\mathrm{e})}, x_{\beta,1}^{(\mathrm{s})})\end{aligned} \tag{A.62}$$

$$\begin{aligned}\frac{\mathrm{d}x_{\alpha,i}^{(\mathrm{e})}}{\mathrm{d}t} = &-\frac{v^{(\mathrm{e})}}{\Delta z}\left(x_{\alpha,i}^{(\mathrm{e})} - x_{\alpha,i-1}^{(\mathrm{e})}\right) + \frac{\delta}{(1-\delta)\varepsilon_{\mathrm{mf}}}K^{(\mathrm{be})}(x_{\alpha,i}^{(\mathrm{b})} - x_{\alpha,i}^{(\mathrm{e})})\ldots \\ &+ \frac{1-\varepsilon_{\mathrm{mf}}}{\varepsilon_{\mathrm{mf}}}\frac{\rho^{(\mathrm{s})}}{c_{\mathrm{t}}^{(\mathrm{g})}}\sum_{j}^{N_R}\nu_{\alpha,j}r_j^M(x_{\alpha,i}^{(\mathrm{e})}, x_{\beta,i}^{(\mathrm{s})}) \qquad \forall i = 2\ldots N_{FV}\end{aligned} \tag{A.63}$$

$$\frac{\mathrm{d}x_{\beta,1}^{(\mathrm{s})}}{\mathrm{d}t} = \frac{D_v^{(\mathrm{s})}}{\Delta z^2}\left(x_{\beta,2}^{(\mathrm{s})} - x_{\beta,1}^{(\mathrm{s})}\right) + M^{(\mathrm{s})}\sum_{j}^{N_R}\nu_{\beta,j}r_j^M(x_{\alpha,1}^{(\mathrm{e})}, x_{\beta,1}^{(\mathrm{s})}) \tag{A.64}$$

$$\begin{aligned}\frac{\mathrm{d}x_{\beta,i}^{(\mathrm{s})}}{\mathrm{d}t} = &\frac{D_v^{(\mathrm{s})}}{\Delta z^2}\left(x_{\beta,i+1}^{(\mathrm{s})} - 2x_{\beta,i}^{(\mathrm{s})} + x_{\beta,i-1}^{(\mathrm{s})}\right)\ldots \\ &+ M^{(\mathrm{s})}\sum_{j}^{N_R}\nu_{\beta,j}r_j^M(x_{\alpha,i}^{(\mathrm{e})}, x_{\beta,i}^{(\mathrm{s})}) \qquad \forall i = 2\ldots N_{FV}-1\end{aligned} \tag{A.65}$$

$$\frac{\mathrm{d}x_{\beta,n}^{(\mathrm{s})}}{\mathrm{d}t} = -\frac{D_v^{(\mathrm{s})}}{\Delta z^2}\left(x_{\beta,n}^{(\mathrm{s})} - x_{\beta,n-1}^{(\mathrm{s})}\right) + M^{(\mathrm{s})}\sum_{j}^{N_R}\nu_{\beta,j}r_j^M(x_{\alpha,n}^{(\mathrm{e})}, x_{\beta,n}^{(\mathrm{s})}) \tag{A.66}$$

Here, i indicates the number of finite volumes ranging from 1 to N_{FV}. In this work, 50 finite elements were used for simulation and optimization. This number was found to be most efficient while granting accurate results.

A.5 Numerical stability

The piecewise definition of the rate expressions in Chapter 6 (equations (6.24) to (6.27)) can lead to excessively large computation times or convergence problems for implicit ODE solvers because the function is not differentiable (even though it is continuous) at chemical equilibrium. Therefore, the piecewise definition of equations (6.34) to (6.37) is substituted by a differentiable function, that approximates the orig-

inal equations. A sigmoid function is introduced as follows:

$$r_1^M = r_{1+}^M \cdot \left(0.5 - 0.5 \frac{y_{\mathrm{CO}} - \frac{K_{\mathrm{eq},1}}{1+K_{\mathrm{eq},1}}}{\sqrt{\left(y_{\mathrm{CO}} - \frac{K_{\mathrm{eq},1}}{1+K_{\mathrm{eq},1}} \right)^2 + \eta}} \right) - r_{1-}^M \cdot \left(0.5 + 0.5 \frac{y_{\mathrm{CO}} - \frac{K_{\mathrm{eq},1}}{1+K_{\mathrm{eq},1}}}{\sqrt{\left(y_{\mathrm{CO}} - \frac{K_{\mathrm{eq},1}}{1+K_{\mathrm{eq},1}} \right)^2 + \eta}} \right) \tag{A.67}$$

$$r_2^M = r_{2+}^M \cdot \left(0.5 - 0.5 \frac{y_{\mathrm{CO}} - \frac{K_{\mathrm{eq},2}}{1+K_{\mathrm{eq},2}}}{\sqrt{\left(y_{\mathrm{CO}} - \frac{K_{\mathrm{eq},2}}{1+K_{\mathrm{eq},2}} \right)^2 + \eta}} \right) - r_{2-}^M \cdot \left(0.5 + 0.5 \frac{y_{\mathrm{CO}} - \frac{K_{\mathrm{eq},2}}{1+K_{\mathrm{eq},2}}}{\sqrt{\left(y_{\mathrm{CO}} - \frac{K_{\mathrm{eq},2}}{1+K_{\mathrm{eq},2}} \right)^2 + \eta}} \right) \tag{A.68}$$

$$r_3^M = r_{3+}^M \cdot \left(0.5 - 0.5 \frac{y_{\mathrm{H_2O}} - \frac{K_{\mathrm{eq},3}}{1+K_{\mathrm{eq},3}}}{\sqrt{\left(y_{\mathrm{H_2O}} - \frac{K_{\mathrm{eq},3}}{1+K_{\mathrm{eq},3}} \right)^2 + \eta}} \right) - r_{3-}^M \cdot \left(0.5 + 0.5 \frac{y_{\mathrm{H_2O}} - \frac{K_{\mathrm{eq},3}}{1+K_{\mathrm{eq},3}}}{\sqrt{\left(y_{\mathrm{H_2O}} - \frac{K_{\mathrm{eq},3}}{1+K_{\mathrm{eq},3}} \right)^2 + \eta}} \right) \tag{A.69}$$

$$r_4^M = r_{4+}^M \cdot \left(0.5 - 0.5 \frac{y_{\mathrm{H_2O}} - \frac{K_{\mathrm{eq},4}}{1+K_{\mathrm{eq},4}}}{\sqrt{\left(y_{\mathrm{H_2O}} - \frac{K_{\mathrm{eq},4}}{1+K_{\mathrm{eq},4}} \right)^2 + \eta}} \right) - r_{4-}^M \cdot \left(0.5 + 0.5 \frac{y_{\mathrm{H_2O}} - \frac{K_{\mathrm{eq},4}}{1+K_{\mathrm{eq},4}}}{\sqrt{\left(y_{\mathrm{H_2O}} - \frac{K_{\mathrm{eq},4}}{1+K_{\mathrm{eq},4}} \right)^2 + \eta}} \right) \tag{A.70}$$

Here, r_{j+}^M and r_{j-}^M denote the forward and backward reaction rate of reaction j, respectively, and η is an adjustable parameter for the steepness of the sigmoid function. The value is set to $\eta = 1 \times 10^{-7}$, providing a fair trade-off between accuracy and numerical stability. However, the approximation of the original reaction rates by a differentiable function gives rise to a new problem. In equations (A.67) to (A.70), the forward and backward reaction rates are both computed regardless of the actual composition of the gas. Therefore, terms like $\left(y_{\mathrm{CO_2}}^{(\mathrm{g})} - \frac{y_{\mathrm{CO}}^{(\mathrm{g})}}{K_{\mathrm{eq},1}} \right)$ (see eq. (6.34)) yield negative values if $\frac{y_{\mathrm{CO}}^{(\mathrm{g})}}{y_{\mathrm{CO_2}}^{(\mathrm{g})}} > K_{\mathrm{eq},1}$. For non-integer values of the corresponding exponent m_O this becomes problematic because a solution exists only in complex space. To avoid this, the absolute values are used for calculation. However, since the absolute function is non-differentiable at $x = 0$, a differentiable approximation must be used again. The approximation function is exemplified in the following for the relevant term in equa-

tion 6.34:

$$y_{\mathrm{CO_2}}^{(\mathrm{g})} - \frac{y_{\mathrm{CO}}^{(\mathrm{g})}}{K_{\mathrm{eq},1}} \approx \sqrt{\left(y_{\mathrm{CO_2}}^{(\mathrm{g})} - \frac{y_{\mathrm{CO}}^{(\mathrm{g})}}{K_{\mathrm{eq},1}}\right)^2 + \eta} \tag{A.71}$$

Again, η is an adjustable parameter for the smoothness of the approximation and set to $\eta = 1 \times 10^{-7}$. Using similar approximations for equations 6.34 to 6.37, the original reaction rate equations are converted into differentiable functions, which are better suited for numerical integration. Additional problems may occur in the calculation of the ratios of mole fractions $y_i^{(\mathrm{g})}$. During the oxidation stage, the gas inside the reactor consists of only CO_2 and CO after the leftover gas from the reduction stage is purged. Thus, the denominator in equations (6.30) and (6.31) would become zero. The same is true for the denominators in equations (6.28) and (6.29) for the reduction stage. A machine epsilon is added to the denominator in equations (6.28) to (6.31) to avoid division by zero during simulation.

References

[1] Key world energy statistics. https://www.iea.org/publications/freepublications/publication/KeyWorld2016.pdf. Accessed: 2017-10-31.

[2] World gasification database. https://energy.gov/fe/articles/world-gasification-database-now-available-doe. Accessed: 2017-10-10.

[3] Growth within: A circular economy vision for a competitive europe. https://www.mckinsey.de/files/growth_within_report_circular_economy_in_europe.pdf. Accessed: 2017-12-20.

[4] Building a bridge between energy networks. http://www.sunfire.de/en/applications/fuel. Accessed: 2017-09-19.

[5] *Ecosystems and Human Well-being: Synthesis*. Island Press, Washington, DC, 2005.

[6] A. Abad, T. Mattisson, A. Lyngfelt, and M. Johansson. The use of iron oxide as oxygen carrier in a chemical-looping reactor. *Fuel*, 86(7-8):1021–1035, 2007.

[7] A. Abad, R. Pérez-Vega, L. F. de Diego, F. García-Labiano, P. Gayán, and J. Adánez. Design and operation of a $50\,kW_{th}$ chemical looping combustion (clc) unit for solid fuels. *Applied Energy*, 157:295–303, 2015.

[8] S. Abanades. CO_2 and H_2O reduction by solar thermochemical looping using SnO_2/SnO redox reactions: Thermogravimetric analysis. *International Journal of Hydrogen Energy*, 37(10):8223–8231, 2012.

[9] S. Abanades and G. Flamant. Thermochemical hydrogen production from a two-step solar-driven water-splitting cycle based on cerium oxides. *Solar Energy*, 80 (12):1611–1623, 2006.

[10] J. Adánez, L. F. de Diego, F. García-Labiano, P. Gayán, A. Abad, and J. M. Palacios. Selection of oxygen carriers for chemical-looping combustion. *Energy & Fuels*, 18(2):371–377, 2004.

[11] J. Adánez, A. Abad, F. García-Labiano, P. Gayán, and L. F. de Diego. Progress in chemical-looping combustion and reforming technologies. *Progress in Energy and Combustion Science*, 38(2):215–282, 2012.

[12] C. Agrafiotis, M. Roeb, and C. Sattler. A review on solar thermal syngas production via redox pair-based water/carbon dioxide splitting thermochemical cycles. *Renewable and Sustainable Energy Reviews*, 42:254–285, 2015.

[13] E. Alper and O. Yuksel Orhan. CO_2 utilization: Developments in conversion processes. *Petroleum*, 3(1):109–126, 2017.

[14] I. Alxneit. Assessing the feasibility of separating a stoichiometric mixture of zinc vapor and oxygen by a fast quench – model calculations. *Solar Energy*, 82 (11):959–964, 2008.

[15] M. Anheden and G. Svedberg. Exergy analysis of chemical-looping combustion systems. *Energy Conversion and Management*, 39(16-18):1967–1980, 1998.

[16] N. C. Arens and I. D. West. Press-pulse: A general theory of mass extinction? *Paleobiology*, 34(04):456–471, 2008.

[17] M. Aresta. *Carbon Dioxide Recovery and Utilization*. Kluwer Academic Publishers, Dordrecht and Boston, 2003.

[18] A. E. Ashley, A. L. Thompson, and D. O'Hare. Non-metal-mediated homogeneous hydrogenation of CO_2 to CH_3OH. *Angewandte Chemie (International ed. in English)*, 48(52):9839–9843, 2009.

[19] K. Atwood, M. R. Arnold, and E. G. Appel. Water-gas shift reaction. effect of pressure on rate over an iron-oxide-chromium oxide catalyst. *Industrial & Engineering Chemistry*, 42(8):1600–1602, 1950.

[20] R. Bader, L. J. Venstrom, J. H. Davidson, and W. Lipiński. Thermodynamic analysis of isothermal redox cycling of ceria for solar fuel production. *Energy & Fuels*, 27(9):5533–5544, 2013.

[21] I. Barin. *Thermochemical Data of Pure Substances*. Wiley-VCH Verlag GmbH, Weinheim, Germany, 1995.

[22] C. H. Bartholomew. Mechanisms of catalyst deactivation. *Applied Catalysis A: General*, 212(1-2):17–60, 2001.

[23] L. E. Baur and A. Z. Glaessner. *Phys. Chem.*, 43:354–368, 1903.

[24] S. Bebelis, H. Karasali, and C. G. Vayenas. Electrochemical promotion of the CO_2 hydrogenation on Pd/YSZ and Pd/$\beta'' - Al_2O_3$ catalyst-electrodes. *Solid State Ionics*, 179(27-32):1391–1395, 2008.

[25] B. M. Bhanage and M. Arai, editors. *Transformation and Utilization of Carbon Dioxide*. Springer, Heidelberg and New York, 2014.

[26] S. Bhavsar, M. Najera, and G. Veser. Chemical looping dry reforming as novel, intensified process for CO_2 activation. *Chemical Engineering & Technology*, 35 (7):1281–1290, 2012.

[27] E. Bilgen, M. Ducarroir, M. Foex, F. Sibieude, and F. Trombe. Use of solar energy for direct and two-step water decomposition cycles. *International Journal of Hydrogen Energy*, 2(3):251–257, 1977.

[28] A. Bischi, Ø. Langørgen, I. Saanum, J. Bakken, M. Seljeskog, M. Bysveen, J.-X. Morin, and O. Bolland. Design study of a $150\,kW_{th}$ double loop circulating fluidized bed reactor system for chemical looping combustion with focus on industrial applicability and pressurization. *International Journal of Greenhouse Gas Control*, 5(3):467–474, 2011.

[29] L. v. Bogdandy and H.-J. Engell. *Die Reduktion der Eisenerze: Wissenschaftliche Grundlagen und technische Durchführung*. Springer Berlin Heidelberg, Berlin, 2013.

[30] A. Borgschulte, N. Gallandat, B. Probst, R. Suter, E. Callini, D. Ferri, Y. Arroyo, R. Erni, H. Geerlings, and A. Züttel. Sorption enhanced CO_2 methanation. *Physical chemistry chemical physics : PCCP*, 15(24):9620–9625, 2013.

[31] K. P. Brooks, J. Hu, H. Zhu, and R. J. Kee. Methanation of carbon dioxide by hydrogen reduction using the sabatier process in microchannel reactors. *Chemical Engineering Science*, 62(4):1161–1170, 2007.

[32] L. C. Buelens, V. V. Galvita, H. Poelman, C. Detavernier, and G. B. Marin. Super-dry reforming of methane intensifies CO_2 utilization via Le Chatelier's principle. *Science (New York, N.Y.)*, 354(6311):449–452, 2016.

[33] B. Bulfin, F. Call, M. Lange, O. Lübben, C. Sattler, R. Pitz-Paal, and I. V. Shvets. Thermodynamics of CeO_2 thermochemical fuel production. *Energy & Fuels*, 29 (2):1001–1009, 2015.

[34] B. Bulfin, J. Vieten, C. Agrafiotis, M. Roeb, and C. Sattler. Applications and limitations of two step metal oxide thermochemical redox cycles; a review. *J. Mater. Chem. A*, 5(36):18951–18966, 2017.

[35] M. Carmo, D. L. Fritz, J. Mergel, and D. Stolten. A comprehensive review on PEM water electrolysis. *International Journal of Hydrogen Energy*, 38(12): 4901–4934, 2013.

[36] B. T. Carvill, J. R. Hufton, M. Anand, and S. Sircar. Sorption-enhanced reaction process. *AIChE Journal*, 42(10):2765–2772, 1996.

[37] P. Charvin, S. Abanades, G. Flamant, and F. Lemort. Two-step water splitting thermochemical cycle based on iron oxide redox pair for solar hydrogen production. *Energy*, 32(7):1124–1133, 2007.

[38] M. W. Chase. *NIST-JANAF thermochemical tables*, volume 9 of *Journal of physical and chemical reference data. Monograph*. Published by the American Chemical Society and the American Institute of Physics for the National Institute of Standards and Technology, Washington, DC, 4th edition, 1998.

[39] C.-S. Chen, W.-H. Cheng, and S.-S. Lin. Mechanism of CO formation in reverse water–gas shift reaction over Cu/Al_2O_3 catalyst. *Catalysis Letters*, 68(1):45–48, 2000.

[40] Z. Chen, J. J. Concepcion, M. K. Brennaman, P. Kang, M. R. Norris, P. G. Hoertz, and T. J. Meyer. Splitting CO_2 into CO and O_2 by a single catalyst. *Proceedings of the National Academy of Sciences of the United States of America*, 109(39): 15606–15611, 2012.

[41] D. Cheng, F. R. Negreiros, E. Aprà, and A. Fortunelli. Computational approaches to the chemical conversion of carbon dioxide. *ChemSusChem*, 6(6): 944–965, 2013.

[42] W. C. Cho, D. Y. Lee, M. W. Seo, S. D. Kim, K. Kang, K. K. Bae, C. H. Kim, S. Jeong, and C. S. Park. Continuous operation characteristics of chemical looping hydrogen production system. *Applied Energy*, 113:1667–1674, 2014.

[43] W. C. Chueh, C. Falter, M. Abbott, D. Scipio, P. Furler, S. M. Haile, and A. Steinfeld. High-flux solar-driven thermochemical dissociation of CO_2 and H_2O using nonstoichiometric ceria. *Science (New York, N.Y.)*, 330(6012):1797–1801, 2010.

[44] E. N. Coker, A. Ambrosini, M. A. Rodriguez, and J. E. Miller. Ferrite-ysz composites for solar thermochemical production of synthetic fuels: In operando characterization of CO_2 reduction. *Journal of Materials Chemistry*, 21(29):10767, 2011.

[45] J. Cook, D. Nuccitelli, S. A. Green, M. Richardson, B. Winkler, R. Painting, R. Way, P. Jacobs, and A. Skuce. Quantifying the consensus on anthropogenic global warming in the scientific literature. *Environmental Research Letters*, 8 (2):024024, 2013.

[46] J. Cook, N. Oreskes, P. T. Doran, W. R. L. Anderegg, B. Verheggen, E. W. Maibach, J. S. Carlton, S. Lewandowsky, A. G. Skuce, S. A. Green, D. Nuccitelli, P. Jacobs, M. Richardson, B. Winkler, R. Painting, and K. Rice. Consensus on consensus: A synthesis of consensus estimates on human-caused global warming. *Environmental Research Letters*, 11(4):048002, 2016.

[47] Y. A. Daza and J. N. Kuhn. CO_2 conversion by reverse water gas shift catalysis: Comparison of catalysts, mechanisms and their consequences for CO_2 conversion to liquid fuels. *RSC Adv*, 6(55):49675–49691, 2016.

[48] Y. A. Daza, R. A. Kent, M. M. Yung, and J. N. Kuhn. Carbon dioxide conversion by reverse water-gas shift chemical looping on perovskite-type oxides. *Industrial & Engineering Chemistry Research*, 53(14):5828–5837, 2014.

[49] Y. A. Daza, D. Maiti, R. A. Kent, V. R. Bhethanabotla, and J. N. Kuhn. Isothermal reverse water gas shift chemical looping on $La_{0.75}Sr_{0.25}Co_{(1-Y)}Fe_YO_3$ perovskite-type oxides. *Catalysis Today*, 258, Part 2:691–698, 2015.

[50] L. F. de Diego, M. Ortiz, F. García-Labiano, J. Adánez, A. Abad, and P. Gayán. Hydrogen production by chemical-looping reforming in a circulating fluidized bed reactor using ni-based oxygen carriers. *Journal of Power Sources*, 192(1): 27–34, 2009.

[51] Y. Demirel. *Nonequilibrium Thermodynamics*. Elsevier Science, Amsterdam, 2nd edition, 2007.

[52] S. Dey, B. S. Naidu, and C. N. R. Rao. $Ln_{0.5}A_{0.5}MnO_3$ (Ln = Lanthanide, A = Ca, Sr) perovskites exhibiting remarkable performance in the thermochemical generation of CO and H_2 from CO_2 and H_2O. *Chemistry – A European Journal*, 21(19):7077–7081, 2015.

[53] I. Dimitriou, P. García-Gutiérrez, R. H. Elder, R. M. Cuéllar-Franca, A. Azapagic, and R. W. K. Allen. Carbon dioxide utilisation for production of transport fuels: Process and economic analysis. *Energy Environ. Sci.*, 8(6):1775–1789, 2015.

[54] I. Ermanoski, N. P. Siegel, and E. B. Stechel. A new reactor concept for efficient solar-thermochemical fuel production. *Journal of Solar Energy Engineering Transactions of the ASME*, 135(3), 2013.

[55] I. Ermanoski, J. E. Miller, and M. D. Allendorf. Efficiency maximization in solar-thermochemical fuel production: Challenging the concept of isothermal water splitting. *Physical Chemistry Chemical Physics*, 16(18):8418, 2014.

[56] C. P. Falter, A. Sizmann, and R. Pitz-Paal. Modular reactor model for the solar thermochemical production of syngas incorporating counter-flow solid heat exchange. *Solar Energy*, 122:1296–1308, 2015.

[57] L.-S. Fan, L. Zeng, and S. Luo. Chemical-looping technology platform. *AIChE Journal*, 61(1):2–22, 2015.

[58] H. Fang, L. Haibin, and Z. Zengli. Advancements in development of chemical-looping combustion: A review. *International Journal of Chemical Engineering*, 2009(5):1–16, 2009.

[59] J. R. Fernández and J. C. Abanades. Conceptual design of a ni-based chemical looping combustion process using fixed-beds. *Applied Energy*, 135:309–319, 2014.

[60] D. Ferrero, A. Lanzini, M. Santarelli, and P. Leone. A comparative assessment on hydrogen production from low- and high-temperature electrolysis. *International Journal of Hydrogen Energy*, 38(9):3523–3536, 2013.

[61] B. Fidalgo, A. Dominguez, J. Pis, and J. Menedez. Microwave-assisted dry reforming of methane. *International Journal of Hydrogen Energy*, 33(16): 4337–4344, 2008.

[62] J. E. Funk and R. M. Reinstrom. Energy requirements in production of hydrogen from water. *Industrial & Engineering Chemistry Process Design and Development*, 5(3):336–342, 1966.

[63] P. Furler, J. R. Scheffe, and A. Steinfeld. Syngas production by simultaneous splitting of H_2O and CO_2 via ceria redox reactions in a high-temperature solar reactor. *Energy and Environmental Science*, 5:6098–6103, 2012.

[64] P. Furler, J. Scheffe, D. Marxer, M. Gorbar, A. Bonk, U. Vogt, and A. Steinfeld. Thermochemical CO_2 splitting via redox cycling of ceria reticulated foam structures with dual-scale porosities. *Physical Chemistry Chemical Physics : PCCP*, 16(22):10503–10511, 2014.

[65] M. E. Gálvez, P. G. Loutzenhiser, I. Hischier, and A. Steinfeld. CO_2 splitting via two-step solar thermochemical cycles with Zn/ZnO and FeO/Fe_3O_4 redox reactions: Thermodynamic analysis. *Energy & Fuels*, 22(5):3544–3550, 2008.

[66] V. V. Galvita, T. Hempel, H. Lorenz, L. K. Rihko-Struckmann, and K. Sundmacher. Deactivation of modified iron oxide materials in the cyclic water gas shift process for CO-free hydrogen production. *Industrial & Engineering Chemistry Research*, 47(2):303–310, 2008.

[67] V. V. Galvita, H. Poelman, V. Bliznuk, C. Detavernier, and G. B. Marin. CeO_2-modified Fe_2O_3 for CO_2 utilization via chemical looping. *Industrial & Engineering Chemistry Research*, 52(25):8416–8426, 2013.

[68] X. Gao, A. Vidal, A. Bayon, R. Bader, J. Hinkley, W. Lipinski, and A. Tricoli. Efficient ceria nanostructures for enhanced solar fuel production via high-temperature thermochemical redox cycles. *Journal of Material Chemistry A*, 4 (24):9614–9624, 2016.

[69] E. García-Díez, F. García-Labiano, L. F. de Diego, A. Abad, P. Gayán, J. Adánez, and J. Ruíz. Steam, dry, and steam-dry chemical looping reforming of diesel fuel in a $1\,kW_{th}$ unit. *Chemical Engineering Journal*, 325:369–377, 2017.

[70] D. Geldart. Types of gas fluidization. *Powder Technology*, 7(5):285–292, 1973.

[71] V. Gesellschaft. *VDI-Wärmeatlas*. Springer Berlin Heidelberg, Wiesbaden, 10th edition, 2005.

[72] F. J. Gotor, J. M. Criado, J. Malek, and N. Koga. Kinetic analysis of solid-state reactions: The universality of master plots for analyzing isothermal and nonisothermal experiments. *The Journal of Physical Chemistry A*, 104(46): 10777–10782, 2000.

[73] C. A. Gueymard. The sun's total and spectral irradiance for solar energy applications and solar radiation models. *Solar Energy*, 76(4):423–453, 2004.

[74] V. Hacker, R. Fankhauser, G. Faleschini, H. Fuchs, K. Friedrich, M. Muhr, and K. Kordesch. Hydrogen production by steam-iron process. *Journal of Power Sources*, 86(1-2):531–535, 2000.

[75] W. Haije and H. Geerlings. Efficient production of solar fuel using existing large scale production technologies. *Environmental Science & Technology*, 45 (20):8609–8610, 2011.

[76] S. F. Hakonsen and R. Blom. Chemical looping combustion in a rotating bed reactor – finding optimal process conditions for prototype reactor. *Environmental Science & Technology*, 45(22):9619–9626, 2011.

[77] M. M. Halmann. *Chemical Fixation of Carbon Dioxide: Methods of Recycling* CO_2 *into Useful Products*. CRC Press, 1st edition, 1993.

[78] L. Han and G. M. Bollas. Dynamic optimization of fixed bed chemical-looping combustion processes. *Energy*, 112:1107–1119, 2016.

[79] R. S. Haszeldine. Carbon capture and storage: how green can black be? *Science (New York, N.Y.)*, 325(5948):1647–1652, 2009.

[80] W. M. Haynes. *CRC Handbook of Chemistry and Physics*. CRC Press, Hoboken, 95th edition, 2014.

[81] P. Heidebrecht and K. Sundmacher. Thermodynamic analysis of a cyclic water gas-shift reactor (cwgsr) for hydrogen production. *Chemical Engineering Science*, 64(23):5057–5065, 2009.

[82] P. Heidebrecht, V. Galvita, and K. Sundmacher. An alternative method for parameter identification from temperature programmed reduction (TPR) data. *Chemical Engineering Science*, 63(19):4776–4788, 2008.

[83] P. Heidebrecht, C. Hertel, and K. Sundmacher. Conceptual analysis of a cyclic water gas shift reactor. *International Journal of Chemical Reactor Engineering*, 6(1), 2008.

[84] C. Hertel, P. Heidebrecht, and K. Sundmacher. Experimental quantification and modelling of reaction zones in a cyclic watergas shift reactor. *International Journal of Hydrogen Energy*, 37(3):2195–2203, 2012.

[85] H. Hiller, R. Reimert, and H.-M. Stönner. Gas production, 1. introduction. In *Ullmann's Encyclopedia of Industrial Chemistry*, pages 403–421. Wiley-VCH Verlag GmbH & Co. KGaA, 2000.

[86] M. M. Hossain and H. I. de Lasa. Chemical-looping combustion (CLC) for inherent CO_2 separations – a review. *Chemical Engineering Science*, 63(18): 4433–4451, 2008.

[87] K. Z. House, A. C. Baclig, M. Ranjan, E. A. van Nierop, J. Wilcox, and H. J. Herzog. Economic and energetic analysis of capturing CO_2 from ambient air. *Proceedings of the National Academy of Sciences*, 108(51):20428–20433, 2011.

[88] Z. Huang, H. Jiang, F. He, D. Chen, G. Wei, K. Zhao, A. Zheng, Y. Feng, Z. Zhao, and H. Li. Evaluation of multi-cycle performance of chemical looping dry reforming using CO_2 as an oxidant with $Fe-Ni$ bimetallic oxides. *Journal of Energy Chemistry*, 25(1):62–70, 2016.

[89] C. A. Huff and M. S. Sanford. Cascade catalysis for the homogeneous hydrogenation of CO_2 to methanol. *Journal of the American Chemical Society*, 133 (45):18122–18125, 2011.

[90] Q. Imtiaz, D. Hosseini, and C. R. Müller. Review of oxygen carriers for chemical looping with oxygen uncoupling (CLOU): Thermodynamics, material development, and synthesis. *Energy Technology*, 1(11):633–647, 2013.

[91] Intergovernmental Panel on Climate Change. *Climate Change 2013 - The Physical Science Basis*. Cambridge University Press, Cambridge, 2014.

[92] M. Ishida and H. Jin. A novel combustor based on chemical-looping reactions and its reaction kinetics. *Journal of Chemical Engineering of Japan*, 27(3): 296–301, 1994.

[93] M. Ishida and H. Jin. A new advanced power-generation system using chemical-looping combustion. *Energy*, 19(4):415–422, 1994.

[94] M. Ishida and H. Jin. A novel chemical-looping combustor without NO_x formation. *Industrial & Engineering Chemistry Research*, 35(7):2469–2472, 1996.

[95] M. Ishida, D. Zheng, and T. Akehata. Evaluation of a chemical-looping-combustion power-generation system by graphic exergy analysis. *Energy*, 12 (2):147–154, 1987.

[96] C. Jarrett, W. Chueh, C. Yuan, Y. Kawajiri, K. H. Sandhage, and A. Henry. Critical limitations on the efficiency of two-step thermochemical cycles. *Solar Energy*, 123:57–73, 2016.

[97] Q. Jiang, Z. Chen, J. Tong, M. Yang, Z. Jiang, and C. Li. Direct thermolysis of CO_2 into CO and O_2. *Chemical Communications (Cambridge, England)*, 53(6): 1188–1191, 2017.

[98] P. Kaiser, R. B. Unde, C. Kern, and A. Jess. Production of liquid hydrocarbons with CO_2 as carbon source based on reverse water-gas shift and fischer-tropsch synthesis. *Chemie Ingenieur Technik*, 85(4):489–499, 2013.

[99] G. Karagiannakis. Hydrogenation of carbon dioxide on copper in a H^+ conducting membrane-reactor. *Solid State Ionics*, 162-163:313–318, 2003.

[100] I. Kemp. *Pinch Analysis and Process Integration: A User Guide on Process Integration for the Efficient Use of Energy*. Butterworth-Heinemann, Oxford, 2007.

[101] A. Khawam and D. R. Flanagan. Solid-state kinetic models: Basics and mathematical fundamentals. *The Journal of Physical Chemistry B*, 110(35): 17315–17328, 2006.

[102] J. Kim, C. A. Henao, T. A. Johnson, D. E. Dedrick, J. E. Miller, E. B. Stechel, and C. T. Maravelias. Methanol production from CO_2 using solar-thermal energy: Process development and techno-economic analysis. *Energy Environ. Sci.*, 4: 3122–3132, 2011.

[103] J. Kim, T. A. Johnson, J. E. Miller, E. B. Stechel, and C. T. Maravelias. Fuel production from CO_2 using solar-thermal energy: System level analysis. *Energy Environ. Sci.*, 5:8417–8429, 2012.

[104] T. Kodama and N. Gokon. Thermochemical cycles for high-temperature solar hydrogen production. *Chemical reviews*, 107(10):4048–4077, 2007.

[105] T. Kodama, Y. Nakamuro, and T. Mizuno. A two-step thermochemical water splitting by iron-oxide on stabilized zirconia. *Journal of Solar Energy Engineering*, 128(1):3–7, 2006. International Solar Energy Conference, Portland, OR, JUL 01-14, 2004.

[106] T. Kodama, N. Gokon, and R. Yamamoto. Thermochemical two-step water splitting by ZrO_2-supported $Ni_xFe_{3-x}O_4$ for solar hydrogen production. *Solar Energy*, 82(1):73–79, 2008.

[107] E. Koepf, I. Alxneit, C. Wieckert, and A. Meier. A review of high temperature solar driven reactor technology: 25 years of experience in research and development at the Paul Scherrer Institute. *Applied Energy*, 188:620–651, 2017.

[108] P. T. Krenzke and J. H. Davidson. Thermodynamic analysis of syngas production via the solar thermochemical cerium oxide redox cycle with methane-driven reduction. *Energy & Fuels*, 28(6):4088–4095, 2014.

[109] P. T. Krenzke, J. R. Fosheim, and J. H. Davidson. Solar fuels via chemical-looping reforming. *Solar Energy*, 156:48–72, 2017.

[110] D. Kunii and O. Levenspiel. Fluidized reactor models. 1. for bubbling beds of fine, intermediate, and large particles. 2. for the lean phase: Freeboard and fast fluidization. *Industrial & Engineering Chemistry Research*, 29(7):1226–1234, 1990.

[111] D. Kunii and O. Levenspiel. *Fluidization Engineering*. Wiley, New York, 2nd edition, 1991.

[112] M. Lange, M. Roeb, C. Sattler, and R. Pitz-Paal. T–s diagram efficiency analysis of two-step thermochemical cycles for solar water splitting under various process conditions. *Energy*, 67:298–308, 2014.

[113] J. Lapp, J. H. Davidson, and W. Lipiński. Efficiency of two-step solar thermochemical non-stoichiometric redox cycles with heat recovery. *Energy*, 37(1): 591–600, 2012.

[114] T. L. LeValley, A. R. Richard, and M. Fan. The progress in water gas shift and steam reforming hydrogen production technologies – a review. *International Journal of Hydrogen Energy*, 39(30):16983–17000, 2014.

[115] C. Linderholm, M. Schmitz, P. Knutsson, and A. Lyngfelt. Chemical-looping combustion in a 100 kW unit using a mixture of ilmenite and manganese ore as oxygen carrier. *Fuel*, 166:533–542, 2016.

[116] A. Löfberg, T. Kane, J. Guerrero-Caballero, and L. Jalowiecki-Duhamel. Chemical looping dry reforming of methane: Toward shale-gas and biogas valorization. *Chemical Engineering and Processing: Process Intensification*, 122 (Supplement C):523–529, 2017.

[117] F. Logist, J. Lauwers, B. Trigaux, and J. F. van Impe. Model based optimisation of a cyclic reactor for the production of hydrogen. In *21st European Symposium on Computer Aided Process Engineering*, volume 29 of *Computer Aided Chemical Engineering*, pages 457–461. Elsevier, Amsterdam and Oxford, 2011.

[118] P. G. Loutzenhiser and A. Steinfeld. Solar syngas production from CO_2 and H_2O in a two-step thermochemical cycle via Zn/ZnO redox reactions: Thermodynamic cycle analysis. *International Journal of Hydrogen Energy*, 36(19): 12141–12147, 2011.

[119] P. G. Loutzenhiser, M. E. Galvez, I. Hischier, A. Stamatiou, A. Frei, and A. Steinfeld. CO_2 splitting via two-step solar thermochemical cycles with Zn/ZnO and FeO/Fe_3O_4 redox reactions ii: Kinetic analysis. *Energy & Fuels*, 23(5): 2832–2839, 2009.

[120] A. Lyngfelt and C. Linderholm. Chemical-looping combustion of solid fuels – status and recent progress. *Energy Procedia*, 114:371–386, 2017.

[121] A. Lyngfelt, B. Leckner, and T. Mattisson. A fluidized-bed combustion process with inherent CO_2 separation; application of chemical-looping combustion. *Chemical Engineering Science*, 56(10):3101–3113, 2001.

[122] D. S. Mallapragada, N. R. Singh, V. Curteanu, and R. Agrawal. Sun-to-fuel assessment of routes for fixing CO_2 as liquid fuel. *Industrial & Engineering Chemistry Research*, 52(14):5136–5144, 2013.

[123] T. Mancini, P. Heller, B. Butler, B. Osborn, W. Schiel, V. Goldberg, R. Buck, R. Diver, C. Andraka, and J. Moreno. Dish-stirling systems: An overview of development and status. *Journal of Solar Energy Engineering Transactions of the ASME*, 125(2):135–151, 2003.

[124] D. Marxer, P. Furler, J. R. Scheffe, H. Geerlings, C. Falter, V. Batteiger, A. Sizmann, and A. Steinfeld. Demonstration of the entire production chain to renewable kerosene via solar thermochemical splitting of H_2O and CO_2. *Energy & Fuels*, 29(5):3241–3250, 2015.

[125] T. Mattisson and A. Lyngfelt. Applications of chemical-looping combustion with capture of CO_2. In *Proceedings of the second nordic minisymposium on carbon dioxide capture and storage, Göteborg, Sweden*, 2001.

[126] T. Mattisson, A. Lyngfelt, and H. Leion. Chemical-looping with oxygen uncoupling for combustion of solid fuels. *International Journal of Greenhouse Gas Control*, 3(1):11–19, 2009.

[127] A. H. McDaniel, E. C. Miller, D. Arifin, A. Ambrosini, E. N. Coker, R. O'Hayre, W. C. Chueh, and J. Tong. Sr- and Mn-doped $LaAlO_{3-\delta}$ for solar thermochemical H_2 and CO production. *Energy Environ. Sci.*, 6:2424 – 2428, 2013.

[128] A. Messerschmitt. Process of producing hydrogen, 1910. US Patent 971,206.

[129] B. Metz. *IPCC special report on carbon dioxide capture and storage*. Cambridge University Press for the Intergovernmental Panel on Climate Change, Cambridge, 2005.

[130] B. Moghtaderi. Review of the recent chemical looping process developments for novel energy and fuel applications. *Energy & Fuels*, 26(1):15–40, 2012.

[131] C. L. Muhich, K. C. Weston, D. Arifin, A. H. McDaniel, C. B. Musgrave, and A. W. Weimer. Extracting kinetic information from complex gas-solid reaction data. *Industrial & Engineering Chemistry Research*, 54(16):4113–4122, 2015.

[132] M. Najera, R. Solunke, T. Gardner, and G. Veser. Carbon capture and utilization via chemical looping dry reforming. *Chemical Engineering Research and Design*, 89(9):1533–1543, 2011.

[133] T. Nakamura. Hydrogen production from water utilizing solar heat at high temperatures. *Solar Energy*, 19(5):467–475, 1977.

[134] P. Ohlemüller, F. Alobaid, A. Gunnarsson, J. Ströhle, and B. Epple. Development of a process model for coal chemical looping combustion and validation against 100 kW_{th} tests. *Applied Energy*, 157:433–448, 2015.

[135] K. Otsuka, T. Kaburagi, C. Yamada, and S. Takenaka. Chemical storage of hydrogen by modified iron oxides. *Journal of Power Sources*, 122(2):111–121, 2003.

[136] D. Pakhare and J. Spivey. A review of dry (CO_2) reforming of methane over noble metal catalysts. *Chemical Society reviews*, 43(22):7813–7837, 2014.

[137] R. J. Panlener, R. N. Blumenthal, and J. E. Garnier. A thermodynamic study of nonstoichiometric cerium dioxide. *Journal of Physics and Chemistry of Solids*, 36(11):1213–1222, 1975.

[138] A. A. M. Parra, C. Asmanoglo, and D. W. Agar. Cyclic steady-state behavior and optimization of a fixed-bed adsorptive reactor for the reverse water-gas shift reaction. *Chemical Engineering & Technology*, 2016.

[139] G. Pekridis, K. Kalimeri, N. Kaklidis, E. Vakouftsi, E. F. Iliopoulou, C. Athanasiou, and G. E. Marnellos. Study of the reverse water gas shift (RWGS) reaction over Pt in a solid oxide fuel cell (SOFC) operating under open and closed-circuit conditions. *Catalysis Today*, 127(1-4):337–346, 2007.

[140] S. Penthor, F. Zerobin, K. Mayer, T. Pröll, and H. Hofbauer. Investigation of the performance of a copper based oxygen carrier for chemical looping combustion in a 120 kW pilot plant for gaseous fuels. *Applied Energy*, 145:52–59, 2015.

[141] T. Pröll, P. Kolbitsch, J. Bolhàr-Nordenkampf, and H. Hofbauer. A novel dual circulating fluidized bed system for chemical looping processes. *AIChE Journal*, 55(12):3255–3266, 2009.

[142] D. A. Reay, C. Ramshaw, and A. Harvey. *Process Intensification: Engineering for Efficiency, Sustainability and Flexibility*. Butterworth-Heinemann, Oxford, 2nd edition, 2013.

[143] H. J. Richter and K. F. Knoche. Reversibility of combustion processes. In R. A. Gaggioli, editor, *Efficiency and Costing*, chapter 3, pages 71–85. Washington, D.C., 1983.

[144] F. N. Ridha, D. Lu, A. Macchi, and R. W. Hughes. Combined calcium looping and chemical looping combustion cycles with CaO – CuO pellets in a fixed bed reactor. *Fuel*, 153:202–209, 2015.

[145] E. Rochon and J. Kuper. *False hope: Why carbon capture and storage won't save the climate*. Greenpeace International, Amsterdam, 2008.

[146] J. Rockstrom, W. Steffen, K. Noone, A. Persson, Chapin, F. Stuart, III, E. Lambin, T. M. Lenton, M. Scheffer, C. Folke, H. J. Schellnhuber, B. Nykvist, C. A. de Wit, T. Hughes, S. van der Leeuw, H. Rodhe, S. Sorlin, P. K. Snyder, R. Costanza, U. Svedin, M. Falkenmark, L. Karlberg, R. W. Corell, V. J. Fabry, J. Hansen, B. Walker, D. Liverman, K. Richardson, P. Crutzen, and J. Foley. Planetary boundaries: Exploring the safe operating space for humanity. *Ecology and Society*, 14(2), 2009.

[147] J. A. Rodriguez, J. Evans, L. Feria, A. B. Vidal, P. Liu, K. Nakamura, and F. Illas. CO_2 hydrogenation on Au/TiC, Cu/TiC, and Ni/TiC catalysts: Production of CO, methanol, and methane. *Journal of Catalysis*, 307:162–169, 2013.

[148] J. Rogelj, M. den Elzen, N. Höhne, T. Fransen, H. Fekete, H. Winkler, R. Schaeffer, F. Sha, K. Riahi, and M. Meinshausen. Paris agreement climate proposals need a boost to keep warming well below 2°C. *Nature*, 534(7609):631–639, 2016.

[149] S. Rönsch, J. Schneider, S. Matthischke, M. Schlüter, M. Götz, J. Lefebvre, P. Prabhakaran, and S. Bajohr. Review on methanation – from fundamentals to current projects. *Fuel*, 166:276–296, 2016.

[150] M. Ryden, A. Lyngfelt, and T. Mattisson. Synthesis gas generation by chemical-looping reforming in a continuously operating laboratory reactor. *Fuel*, 85(12-13):1631–1641, 2006.

[151] M. Rydén, P. Moldenhauer, T. Mattisson, A. Lyngfelt, M. Younes, T. Niass, B. Fadhel, and J.-P. Ballaguet. Chemical-looping combustion with liquid fuels. *Energy Procedia*, 37:654–661, 2013.

[152] J. R. Scheffe and A. Steinfeld. Thermodynamic analysis of cerium-based oxides for solar thermochemical fuel production. *Energy & Fuels*, 26(3):1928–1936, 2012.

[153] J. R. Scheffe and A. Steinfeld. Oxygen exchange materials for solar thermochemical splitting of H_2O and CO_2: A review. *Materials Today*, 17(7):341–348, 2014.

[154] R. A. Sheldon. *Chemicals from Synthesis Gas: Catalytic Reactions of* CO *and* H_2, volume 3 of *Catalysis by Metal Complexes*. Springer Netherlands, Dordrecht, 1983.

[155] B. Smith R J, M. Loganathan, and M. S. Shantha. A review of the water gas shift reaction kinetics. *International Journal of Chemical Reactor Engineering*, 8(1), 2010.

[156] H. Y. Sohn. On the rate expressions for "reversible" gas-solid reactions. *Metallurgical and Materials Transactions B*, 45(5):1600–1602, 2014.

[157] C. Song. Global challenges and strategies for control, conversion and utilization of CO_2 for sustainable development involving energy, catalysis, adsorption and chemical processing. *Catalysis Today*, 115(1-4):2–32, 2006.

[158] C. Song, A. F. Gaffney, and K. Fujimoto. CO_2 *Conversion and Utilization*. American Chemical Society and Oxford University Press [distributor], Washington, D.C., 2002.

[159] V. Spallina, P. Chiesa, E. Martelli, F. Gallucci, M. C. Romano, G. Lozza, and M. van Sint Annaland. Reactor design and operation strategies for a large-scale packed-bed CLC power plant with coal syngas. *International Journal of Greenhouse Gas Control*, 36:34–50, 2015.

[160] V. Spallina, B. Marinello, F. Gallucci, M. C. Romano, and M. van Sint Annaland. Chemical looping reforming in packed-bed reactors: Modelling, experimental validation and large-scale reactor design. *Fuel Processing Technology*, 156:156–170, 2017.

[161] A. Stamatiou, P. G. Loutzenhiser, and A. Steinfeld. Solar syngas production from H_2O and CO_2 via two-step thermochemical cycles based on Zn/ZnO and FeO/Fe_3O_4 redox reactions: Kinetic analysis. *Energy & Fuels*, 24(4):2716–2722, 2010.

[162] A. I. Stankiewicz and J. A. Moulijn, editors. *Re-engineering the Chemical Processing Plant: Process Intensification*. Marcel Dekker, New York, N.Y., 2004.

[163] A. Steinfeld. Solar-processed metals as clean energy carriers and water-splitters. *International Journal of Hydrogen Energy*, 23(9):767–774, 1998.

[164] A. Sternberg and A. Bardow. Life cycle assessment of power-to-gas: Syngas vs methane. *ACS Sustainable Chemistry & Engineering*, 4(8):4156–4165, 2016.

[165] Y. Tamaura, A. Steinfeld, P. Kuhn, and K. Ehrensberger. Production of solar hydrogen by a novel, 2-step, water-splitting thermochemical cycle. *Energy*, 20 (4):325–330, 1995.

[166] M. Tang, L. Xu, and M. Fan. Progress in oxygen carrier development of methane-based chemical-looping reforming: A review. *Applied Energy*, 151: 143–156, 2015.

[167] M. Tou, R. Michalsky, and A. Steinfeld. Solar-driven thermochemical splitting of CO_2 and in situ separation of CO and O_2 across a ceria redox membrane reactor. *Joule*, 1(1):146–154, 2017.

[168] P. Trambouze and J.-P. Euzen. *Chemical Reactors: From Design to Operation*. Editions TECHNIP, Paris, revised edition, 2004.

[169] E. R. van Selow, P. D. Cobden, P. A. Verbraeken, J. R. Hufton, and van den Brink, R. W. Carbon capture by sorption-enhanced water-gas shift reaction process using hydrotalcite-based material. *Industrial & Engineering Chemistry Research*, 48(9):4184–4193, 2009.

[170] D. G. Victor, K. Akimoto, Y. Kaya, M. Yamaguchi, D. Cullenward, and C. Hepburn. Prove paris was more than paper promises. *Nature*, 548(7665):25–27, 2017.

[171] G. Voitic, S. Nestl, M. Lammer, J. Wagner, and V. Hacker. Pressurized hydrogen production by fixed-bed chemical looping. *Applied Energy*, 157:399–407, 2015.

[172] W.-H. Wang, Y. Himeda, J. T. Muckerman, G. F. Manbeck, and E. Fujita. CO_2 hydrogenation to formate and methanol as an alternative to photo- and electrochemical CO_2 reduction. *Chemical reviews*, 115(23):12936–12973, 2015.

[173] G. Wei, F. He, Z. Huang, A. Zheng, K. Zhao, and H. Li. Continuous operation of a 10 kW_{th} chemical looping integrated fluidized bed reactor for gasifying biomass using an iron-based oxygen carrier. *Energy & Fuels*, 29(1):233–241, 2015.

[174] M. Welte, R. Barhoumi, A. Zbinden, J. R. Scheffe, and A. Steinfeld. Experimental demonstration of the thermochemical reduction of ceria in a solar aerosol reactor. *Industrial & Engineering Chemistry Research*, 55(40):10618–10625, 2016.

[175] M. Wenzel, N. Aditya Dharanipragada, V. V. Galvita, H. Poelman, G. B. Marin, L. Rihko-Struckmann, and K. Sundmacher. CO production from CO_2 via reverse water-gas shift reaction performed in a chemical looping mode: Kinetics on modified iron oxide. *Journal of CO_2 Utilization*, 17:60–68, 2017.

[176] M. Wenzel, L. Rihko-Struckmann, and K. Sundmacher. Thermodynamic analysis and optimization of RWGS processes for solar syngas production from CO_2. *AIChE Journal*, 63(1):15–22, 2017.

[177] M. Wenzel, L. Rihko-Struckmann, and K. Sundmacher. Continuous production of CO from CO_2 by RWGS chemical looping in fixed and fluidized bed reactors. *Chemical Engineering Journal*, 336:278–296, 2018.

[178] J. E. Whitlow and C. F. Parish. Operation, modeling and analysis of the reverse water gas shift process. In *AIP Conference Proceedings, Alburquerque, New Mexico, (February 4–5, 2003)*, volume 654, pages 1116–1123, Melville, NY, USA, 2003. AIP.

[179] J. Wilcox. *Carbon Capture*. Springer, New York, 2012.

[180] A. Wolf, A. Jess, and C. Kern. Syngas production via reverse water-gas shift reaction over a $Ni-Al_2O_3$ catalyst: Catalyst stability, reaction kinetics, and modeling. *Chemical Engineering & Technology*, 39(6):1040–1048, 2016.

[181] J.-b. Yang, N.-s. Cai, and Z.-s. Li. Hydrogen production from the steam-iron process with direct reduction of iron oxide by chemical looping combustion of coal char. *Energy & Fuels*, 22(4):2570–2579, 2008.

[182] C. L. Yaws. *Thermophysical Properties of Chemicals and Hydrocarbons*. William Andrew, Norwich, N.Y., 2008.

[183] J. Yoshihara and C. T. Campbell. Methanol synthesis and reverse water-gas shift kinetics over Cu(110) model catalysts: Structural sensitivity. *Journal of Catalysis*, 161(2):776–782, 1996.

[184] S. Zhang, R. Xiao, and W. Zheng. Comparative study between fluidized-bed and fixed-bed operation modes in pressurized chemical looping combustion of coal. *Applied Energy*, 130:181–189, 2014.

[185] G. M. B. Zhiquan Zhou, Lu Han. Overview of chemical-looping reduction in fixed bed and fluidized bed reactors focused on oxygen carrier utilization and reactor efficiency. *Aerosol and Air Quality Research*, 14:559–571, 2014.

[186] J. Zielinski, I. Zglinicka, L. Znak, and Z. Kaszkur. Reduction of Fe_2O_3 with hydrogen. *Applied Catalysis A-General*, 381(1-2):191–196, 2010.

[187] E. Zoulias, E. Varkaraki, and N. Lymberopoulos. A review on water electrolysis. *TCJST*, 4(2):41–71, 2004.

List of figures

1.1 Important syngas reaction routes. 4
1.2 Overview of the thesis. 6

2.1 Gibbs free energy of power-to-gas reactions. 9
2.2 RWGS chemical equilibrium. 11

3.1 Chemical looping concept. 16
3.2 Sustainable syngas production by RWGS processes. 19
3.3 Overview of important chemical looping based processes. 21
3.4 Gibbs free energy of OSM oxidation reactions. 28
3.5 Gibbs free energy of OSM reduction reactions. 29

4.1 Idealized process system for syngas production by RWGS. 35
4.2 Idealized process system for syngas production by RWGSCL. 37
4.3 Temperature dependence of the equilibrium constant K_{eq} 39
4.4 Separation efficiency η_{S} 42
4.5 Dimensionless energy factors F for pure CO production. 44
4.6 Optimal reactor feed H_2/CO_2 ratios 45
4.7 StS efficiency η_{StS} 46

5.1 CO yield per cycle for 500 redox cycles. 56
5.2 HR-TEM image of as-prepared Fe_2O_3-$Ce_{0.5}Zr_{0.5}O_2$. 57
5.3 TEM micrograph of a sample with different morphologies. 58
5.4 XRD patterns of as-prepared and 500 times cycled Fe_2O_3-$Ce_{0.5}Zr_{0.5}O_2$. . 60
5.5 In situ XRD for one full redox cycle. 60
5.6 Thermogravimetry and mass spectrometry signal for stabilized OSM. . 61
5.7 Thermogravimetry results for stabilized OSM. 63
5.8 Master plot results for OSM oxidation and reduction. 64

6.1 Illustration of the RWGSCL concept with two reactors. 72
6.2 Illustration of a heterogeneous 1D plug flow reactor. 75

6.3 Illustration of a heterogeneous 1D fluidized bed reactor. 77
6.4 Baur-Glaessner diagram. 79
6.5 Optimization illustration. 90
6.6 Simulation results for the fixed bed reactor design. 94
6.7 Simulation results for the fixed bed reactor design. 96
6.8 Simulation results for the fluidized bed reactor design. 97
6.9 Optimization results for the fixed bed reactor design. 99
6.10 Optimization results for the fixed bed reactor design. 100
6.11 Optimization results for the fluidized bed reactor design. 101
6.12 Pareto plot. 103

A.1 Discretization scheme for the fixed bed reactor model. 118
A.2 Discretization scheme for the fluidized bed reactor model. 124

List of tables

2.1 Enthalpy change of reaction for important power-to-gas reactions. 8

3.1 Classification of important chemical looping based processes. 20
3.2 Oxygen storage capacity of commonly used OSMs. 27

5.1 Used gas-solid kinetic equations for master-plot analysis. 66
5.2 Estimated kinetic parameters. 68

6.1 Summary of process parameters. 102

Publications and statements of authorship

Journal publications

L. Rihko-Struckmann, P. Datta, **M. Wenzel**, K. Sundmacher, N. V. R. Aditya Dharanipragada, H. Poelman, V. V. Galvita, G. B. Marin, Hydrogen and Carbon Monoxide Production by Chemical Looping over Iron-Aluminium Oxides, Energy Technology 4 (2016) 304-313.

M. Wenzel helped evaluating the results and prepared figures for the manuscript.

M. Wenzel, L. Rihko-Struckmann, K. Sundmacher, Thermodynamic Analysis and Optimization of RWGS Processes for Solar Syngas Production from CO_2, AIChE Journal 63 (2017) 15-22.

M. Wenzel formulated the model, analyzed the results and wrote the manuscript.

M. Wenzel, N. V. R. Aditya Dharanipragada, V. V. Galvita, H. Poelman, G. B. Marin, L. Rihko-Struckmann, K. Sundmacher, CO Production From CO_2 via Reverse Water-Gas Shift Reaction Performed in a Chemical Looping Mode: Kinetics on Modified Iron Oxide, Journal of CO_2 Utilization 17 (2017) 60-68.

M. Wenzel carried out the experiments, analyzed the results, estimated the kinetic parameters, created the figures (except for Figures 2, 3 and 5) and wrote the majority of the manuscript (except for Sections 2.3., 2.4., 3.2. and 3.4.). Parts of this publication that were not written originally by the author are included in this thesis but are clearly indicated by quotation marks.

M. Wenzel, L. Rihko-Struckmann, K. Sundmacher, Continuous Production of CO from CO_2 by RWGS Chemical Looping in Fixed and Fluidized Bed Reactors, Chemical Engineering Journal 336 (2018) 278–296.

M. Wenzel derived and implemented the reactor models, analyzed the results and wrote the manuscript.

M. Wenzel, L. Rihko-Struckmann, K. Sundmacher, Derivation of Thermodynamically Consistent Rate Equations for Equilibrium Limited Gas-Solid Reactions, *(internal revision)*.

M. Wenzel derived the new kinetic equations, formulated the models, ran simulations, analyzed the results and wrote the manuscript.

Conference talks and posters

M. Wenzel, L. Rihko-Struckmann, K. Sundmacher, CO_2-Aktivierung mittels Chemical Looping, Jahrestreffen der ProcessNet-Fachgruppe Energieverfahrenstechnik, February 23-24, 2015, Bonn, Germany. (Poster presentation)

M. Wenzel, L. Rihko-Struckmann, K. Sundmacher, CO-Production from CO_2 via RWGS Chemical Looping, Energy Science and Technology (EST2015), May 20-22, 2015, Karlsruhe, Germany. (Oral presentation)

M. Wenzel, L. Rihko-Struckmann, K. Sundmacher, Thermodynamic Analysis and Optimization of RWGS Processes for Solar Syngas Production, International Symposium on Chemical Reaction Engineering (ISCRE24), June 12-15, 2016, Minneapolis, USA. (Poster presentation, **2nd Poster Award**)

M. Wenzel, L. Rihko-Struckmann, K. Sundmacher, Optimization of Reverse Water-Gas Shift Chemical Looping for Continuous Production of Syngas from CO_2, AIChE Annual Meeting, November 13-18, 2016, San Francisco, USA. (Oral presentation)

M. Wenzel, L. Rihko-Struckmann, K. Sundmacher, Continuous Production of Syngas from CO_2 by Reverse Water-Gas Shift Chemical Looping Processes, World

Congress of Chemical Engineering (WCCE10), October 1-5, 2017, Barcelona, Spain. (Poster presentation)

Curriculum vitae

PERSONAL INFORMATION

Name:	Marcus Wenzel
Date of birth:	April 5, 1988
Place of birth:	Köthen (Anhalt), Germany
Marital status:	in relationship, one child
Nationality:	German

EDUCATION

1994 – 1998	Primary school “Wolfgang Ratke”, Köthen, Germany
1998 – 2000	High school “Völkerfreundschaft”, Köthen, Germany
2000 – 2007	High school “Ludwigsgymnasium”, Köthen, Germany
10/2007 – 09/2010	Anhalt University of Applied Sciences, Köthen, Germany Field of study: Chemical engineering Academic degree: Bachelor of Engineering (B.Eng.) Thesis title: “Betriebs- und Abwasserbehandlung durch Adsorption”

10/2010 – 08/2013	Otto von Guericke University Magdeburg, Magdeburg, Germany Field of study: Mechanical and Process Engineering Academic degree: Master of Science (M.Sc.) Thesis title: “Dynamic Optimization of Reactive Separation Processes exemplified by Cyclohexanol Production from Cyclohexene”
08/2012 – 12/2012	Semester abroad (Erasmus programme) Lappeenranta University of Technology, Lappeenranta, Finland

WORK EXPERIENCE

07/2009 – 09/2009	Ningbo Oceanking Chemical Development Corporation, Ningbo, China Internship, Chloralkali process
01/2010 – 03/2010	ContiTech AG, Dannenberg, Germany Internship, Research and Development
11/2011 – 03/2012	Wacker Chemie AG, Burghausen, Germany Internship, Research and Development
11/2011 – 03/2012	Max Planck Institute for Dynamics of Complex Technical Systems, Magdeburg, Germany Research assistant, Process Systems Engineering
since 09/2013	Max Planck Institute for Dynamics of Complex Technical Systems, Magdeburg, Germany PhD student, Process Systems Engineering